Max Planck Institute
of Colloids and Interfaces

Universität Potsdam

MAGNETIC ANISOTROPY ANALYSIS OF MAGNETIC NANOPARTICLES IN MAGNETOTACTIC BACTERIA

Dissertation

zur Erlangung des akademischen Grades
"doctor rerum naturalium"
(Dr. rer. nat.)
in der Wissenschaftsdisziplin "Biological Physics"

eingereicht an der
Mathematisch-Naturwissenschaftlichen Fakultät
der Universität Potsdam

von

Sara Ghaisari

MAX PLANCK INSTITUTE OF COLLOIDS AND INTERFACES
DEPARTMENT BIOMATERIALS

Potsdam, September 2017

Abstract

The magnetic anisotropy is a fundamental indicator of the magnetization stability of magnetic nanoparticles. Magnetotactic bacteria form intracellular assemblies of magnetic nanoparticles called magnetosomes. These magnetosomes are typically arranged in chains, but organizations such as clusters and scattered particles are observed in some species and in various genetically modified mutant strains. As such, the bacteria have developed as a model for the understanding of how organization of nanoparticles influences magnetic properties.

In this study, ferromagnetic resonance (FMR) spectroscopy is first used to measure the magnetic anisotropies in different strains of *Magnetospirillum gryphiswaldense* MSR-1, a bacterial species that is amendable to genetic mutations. I use the wild-type MSR-1 cells, Δ*mamJ* and Δ*F3* mutants. These samples exhibit a variety of magnetosomes assembly, and are used to study the effect of particle configurations on magnetization properties. The experimental results are combined with a theoretical model, which I use to describe the spectra and extract parameters characterizing the different nanoparticle organizations. The model indeed includes chain imperfections and misalignments in addition to the intrinsic magnetic properties of the magnetosomes. Thereby, applying this model to analyze the FMR data, the distribution of orientations in the bulk sample can be retrieved in addition to the average chain length. This shows that the bulk sample of WT has an average anisotropy higher than the Δ*mamJ* and Δ*F3* samples. Also, the magnetosome chains of WT cells align with 25° deviation around the direction of an applied magnetic field. Next, I study the collective magnetic response of nanoparticle assemblies by measuring the remanent magnetization of various magnetosome configurations and mapping their magnetization using X-ray photoemission electron microscopy (XPEEM). The structural properties of each configuration are analyzed using scanning electron microscopy (SEM). For each magnetosome structure a remanent curve is plotted and analyzed based on the assembly shape. The remanence curves show that a linear magnetosome chain has a more stable magnetization, in comparison with a magnetosome cluster.

In summary, I have developed a framework to apply FMR for characterizing the average anisotropy of a bulk sample, and correlating this to both their particle configuration and structure orientation. In addition, I measure the magnetic stability of various formed particle configurations, based on their anisotropies, at the nanoscale. The conclusion is that, as expected, the linear magnetosome chain configurations typical of WT cells display a magnetic single domain property due to its high uniaxial anisotropy, while the clustered magnetosomes act as a multi-domain material, with lower magnetic stability.

Zusammenfassung

Die magnetische Anisotropie ist ein fundamentaler Indikator für die Stabilität der Magnetisierung magnetischer Nanopartikel. Magnetotaktische Bakterien formen intrazelluläre Verbände von magnetischen Nanopartikeln, welche Magnetosomen genannt werden. Diese Magnetosomen sind typischerweise in Ketten angeordnet, wobei auch Cluster und einzeln auftretende Partikel in einigen Spezies und in verschiedenen genetisch mutierten Strängen auftreten. Dadurch sind derartige Bakterien zu einem Modellsystem geworden, um den Einfluss von Organisation von magnetischen Nanopartikeln auf deren magnetischen Eigenschaften zu untersuchen.

In dieser Studie wird ferromagnetische Resonanz (FMR) Spektroskopie genutzt, um die magnetische Anisotropie in verschiedenen Strängen von *Magnetosprillum gryphiswaldense* MSR-1, einer Spezies von Bakterien mit einer Vielzahl von bekannten genetischen Mutationen, zu untersuchen. Für diese Studie wurde der MSR-1 Wildtyp, die Δ*mamJ* und die Δ*F3* Mutante genutzt. Diese Proben weisen eine Vielfalt von Magnetosomenanordnungen auf und werden genutzt, um den Effekt dieser Anordnungen auf deren magnetische Eigenschaften zu studieren. Die experimentellen Resultate werden mit einem theoretischen Modell kombiniert, um die Spektren zu beschreiben und Parameter zu ermitteln, welche die Partikelanordnung beschreiben. Das Modell bezieht dabei Kettenimperfektionen und Fehlausrichtungen zusätzlich zu intrinsischen magnetischen Eigenschaften der Partikel mit ein. Durch das Anwenden des entwickelten Modells kann die Verteilung von Orientierungen aus den FMR Daten einer Volumenprobe mit der mittleren Kettenlänge gewonnen werden. Darüber hinaus wird das kollektive magnetische Verhalten von Nanopartikelverbänden studiert, indem die Remanenz ermittelt und ihre Magnetisierung durch Röntgen-Photoemissionselektronenmikroskopie (X-ray photoemission electron microscopy, XPEEM) visualisiert wird. Die strukturellen Eigenschaften einer jeden Konfiguration werden durch die Rasterelektronenmikroskopie analysiert. Für jede Magnetosomenanordnung wird eine Remanenzkurve bestimmt und anhand der Partikelanordnung analysiert.

Zusammenfasssend wurde ein Vorgehen entwickelt, um FMR für die Charakterisierung der mittleren Anisotropie einer Volumenprobe nutzbar zu machen, während die Partikelkonfiguration und Orientierung der Struktur berücksichtigt werden. Zusätzlich wurde die magnetische Stabilität verschiedener Partikelanordnungen basierend auf ihrer Anisotropie gemessen. Als Schlussfolgerung ergibt sich, dass sich eine Magnetosomenkette eines Wildtypen aufgrund ihrer hohen uniaxialen Anisotropie wie ein Eindomänenpartikel verhält, während Cluster von Magnetosomen ein Mehrdomänenverhalten mit einer geringeren magnetischen Stabilität aufweisen.

Contents

List of Figures

List of Tables

1 Introduction and Objectives

1.1 Introduction

Magnetic nanoparticles are of interest in a wide range of applications. Technological applications such as magnetic data storage media (Terris and Thomson, 2005), ferro-fluidic systems (Kurtoğlu, et al., 2012), waste water treatment (Xu, et al., 2012) are vastly developing. Also, magnetic nanoparticles are broadly used in biomedical applications as in magnetic resonance imaging (MRI) agents (Lee, et al., 2005), hyperthermia therapy (Pankhurst, et al., 2003), and medical nano-robots (Martel, et al., 2009). The magnetic anisotropy is the key parameter to control the magnetic hardness of a material, which is important for the application. The anisotropy defines a preferred magnetization direction in the material by introducing an energy barrier for the natural magnetic moments. This can strongly increase the thermal stability of the material at ambient temperature and therefore the potential application of it.

The desired magnetic stability, which is the stability of magnetic moments without an applied field, depends directly on the area of application. For applications such as data storage, a high magnetic stability (in the order of years) is required. For biomedical applications, depending on function, usually a low stability (in the order of milliseconds) is required (Gao, et al., 2009, Prozorov, et al., 2013). This stability differs with the magnetic particle size, shape and

configuration. The particle shape determines whether there is any preferred magnetization direction, and its stability. Further, the assembly of particles into a specific configuration and the consequent dipole couplings will heavily influence the stability and direction of the magnetization (Blachowicz and Ehrmann, 2016). Particularly, a 1D assembly of magnetic nanoparticles is shown to enhance the collective magnetic properties, in comparison with individual nanoparticles (Toulemon, et al., 2016, Yan, et al., 2012, Zhang, et al., 2009). The dipole interaction between the particles leads to a uniaxial anisotropy, which stabilizes the magnetic moments along the chain axis. This varies with the number, orientation, configuration, and crystalline structure of the particles. The production of high-quality chain assemblies, with narrow particle size distribution, high magnetization, uniform crystallinity, and stable structure is still a synthetic challenge, and a purely passive magnetic interactions of magnetic nanoparticles, will not result in such a robust chain formation (Ceylan, et al., 2008, Klumpp and Faivre, 2012, Liu, et al., 2004, Wang, et al., 2009, Zhou, et al., 2008).

Magnetotactic bacteria are prokaryotic cells that are successfully producing high-quality magnetic nanoparticles in different configurations, but mainly as 1D assemblies (Faivre, 2015). These organelles, called magnetosomes, are located inside the cell and function as a bacterial geo-navigator in aquatic and sedimentary environments. The 1D arrangement is optimal for alignment with the earth's magnetic field and transferring sufficient torque to the cell. Among the broad group of these bacteria, the *Magnetospirillum gryphiswaldense* strain MSR-1 has mainly developed as a model system because of their convenient laboratory growth and genetic tractability. Practically, it is possible to culture them in large scale and achieve a high concentration of biosynthetic nanochains, while even controlling the chain configuration by gene modifications.

1.2 Aim of the work

In this work, we focus on MSR-1 magnetosome chains, both intact and isolated from the cells. We study their magnetic anisotropy properties in various configurations and also in both macro (1mL sample) and nano (single magnetosome) scales. We use two techniques for studying the magnetosomes' magnetic anisotropy. The first is ferromagnetic resonance (FMR) spectroscopy, which is a spin resonance measurement. The FMR spectrum shape strongly depends on the magnetic energy of the sample, which in the case of magnetosome chains is mainly affected by three contributions:

- The interaction of the magnetic moment with the external field of the experiment (the Zeeman energy),
- The dipole coupling of the particles along the chain axis (the uniaxial anisotropy),
- And the effect of the crystal structure on the directional magnetization (the magnetocrystalline anisotropy).

The goal is to implement FMR as a method for analyzing the magnetosome configurations through the spectrum line shape, in a bulk sample of cells. We associate the analysis with a theoretical model of the bulk sample and aim to obtain the average anisotropy properties as well as the distribution in the sample.

The second technique is photoemission electron microscopy (PEEM), where the magnetic remanence is measured for individual magnetosome assemblies with various configurations. One of the main results is a direct measurement of the effective magnetic anisotropy for each

of the magnetosome configurations. These values are thoroughly analogous to the theoretical values we get from the FMR simulations, validating the model that we have developed for the bulk sample.

Finally, we apply our methodology for the analysis of the magnetic anisotropy to estimate the presence and alignment of magnetite chains, which are embedded inside a calcite crystal during the crystal growth. By using FMR spectroscopy and by analyzing the line shape, we can conclude that the chains have uniaxial anisotropy and thus are almost linear inside the calcite crystals.

Parts of the FMR study results presented in this thesis, have been published as:

Ghaisari, S., M. Winklhofer, P. Strauch, S. Klumpp and D. Faivre. (2017), 'Magnetosome Organization in Magnetotactic Bacteria Unraveled by Ferromagnetic Resonance Spectroscopy', *Biophysical Journal* Vol. 113, No. 3, pp. 637-644.

The reults of the photoemission electro microscopy are at final revisions for submission as well.

2 Backgrounds and Experimental Methods

2.1 Ferromagnetic Resonance Spectroscopy

2.1.1 Theory of Ferromagnetic Resonance Spectroscopy

Ferromagnetic Resonance (FMR) is a powerful tool for determining magnetic anisotropies. The FMR spectrum shape strongly depends on the magnetic energy of the sample. In the case of magnetosome chains, this is mainly the effect of the crystal structure on the directional magnetization (magnetocrystalline anisotropy), the dipole coupling of the particles along the chain axis (uniaxial anisotropy), and the interaction of the magnetic moment with the external field of the experiment (Zeeman energy).

2.1.1.1 Magnetocrystalline Anisotropy

The crystallographic structure of a magnetic material strongly impacts the direction of its magnetization by influencing the spin-orbit coupling. This can be a source for the magnetic anisotropy of the material, and thus the magnetic energy depends on the magnetization axis direction inside a given crystalline structure. In a cubic system like that of magnetite, the magnetocrystalline anisotropy can be described as the difference of the energy between the three

cubic edges, called α_i. The direction cosine is the projection of the normalized magnetization vector onto the crystallographic axes, $\alpha_i = \frac{\vec{M}}{|M|} \cdot \vec{e}_i$.

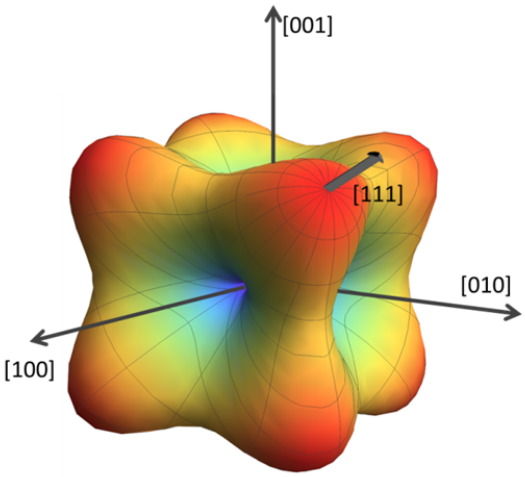

Figure 2.1 Cubic anisotropy energies depicted for a cubic crystal.

The first order magnetocrystalline anisotropy for cubic systems, such as Fe in polar coordinates is:

$$F_{\text{cub}} = K_1 \left(\frac{1}{4} sin^4\theta + \frac{1}{3} cos^4\theta + \frac{\sqrt{2}}{3} sin^3\theta \, cos\theta \, cos3\varphi\right). \qquad (2.1)$$

Assuming the [111] axis to be along the z axis, θ (polar angle) will be the angle between magnetization vector and the [111] axis. In case of magnetite the [111] axis is also the magnetic easy axis (Charilaou, et al., 2011). The parameter K_1 is the first-order anisotropy constant ($K_1 = -0.63 \times 10^4$ J/m^3 for single-crystal bulk magnetite at 150 K), which is the temperature at which the experiment is performed in order to reduce thermal fluctuations. An effective cubic field is also defined as, $H_{\text{cub}} = K_1/M$. The second-order anisotropy constant is neglected, since it only causes small differences in magnetite (Charilaou, et al., 2011).

2.1.1.2 Shape Anisotropy

The shape anisotropy (also referred as uniaxial anisotropy) is mainly the result of the surface magnetization. The boundaries of a single domain ferromagnetic material will cause an internal magnetic moment, acting back on the main magnetization, called the internal demagnetizing field. The direction dependency of this demagnetizing field is the shape anisotropy phenomenon and is defined by the geometry of the material. A spherical ferromagnet has no shape anisotropy, while a needle-like structure can be another extreme of a maximum shape anisotropy (Osborn, 1945).

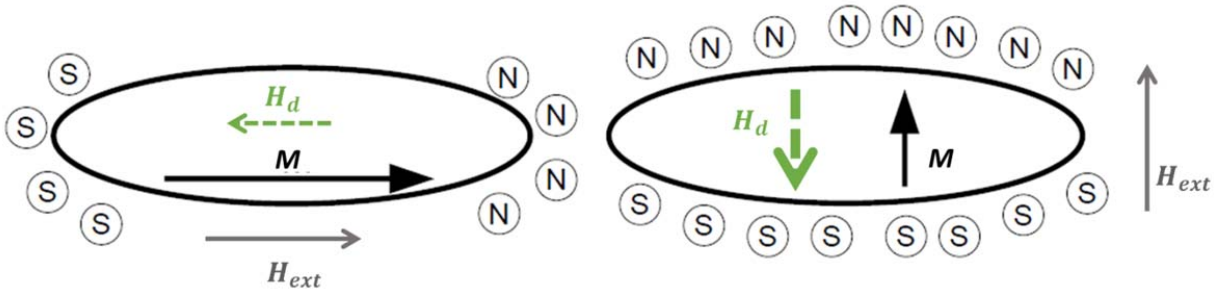

Figure 2.2 Demagnetizing field's angular dependency in an anisotropic geometry.

For the ellipsoid an effective uniaxial field can be defined as:

$$H_{\text{uni}} = 4\pi M N_{\text{eff}}, \qquad (2.2)$$

where N_{eff} is the effective demagnetizing factor ($N_{\text{eff}} = N_{\perp} - N_{\parallel}$) (Osborn, 1945).This term can be used as an equivalent to the uniaxial anisotropy of the inter-particle interactions, when neglecting the second neighbor contributions (Charilaou, et al., 2011).

The energy of this demagnetization field is given as the integral over the volume of the field and the overall magnetization moment:

$$E_{uni} = -\frac{1}{2}\int \vec{H}_{uni}.\vec{M}dV, \qquad (2.3)$$

and the free energy, which is energy per volume, will be calculated from this energy as:

$$F_{\text{shape}} = \frac{E_{uni}}{V} = 2\pi N_{\text{eff}} M^2 cos^2\theta. \qquad (2.4)$$

2.1.1.3 Zeeman Effect

In a homogeneous external magnetic field, a paramagnetic system experiences a split of its energy levels with an energy difference of $\Delta E = g\mu_B B_{ext}$, as depicted in Figure 2.3 where g is the g-factor, which correlates the angular momentum of an atom to its magnetic moment. The value of an effective g-factor for the free electron is usually more than 2 (Fletcher, 1954). In addition, $\mu_B = \frac{e\hbar}{2m_e}$ is the Bohr magneton.

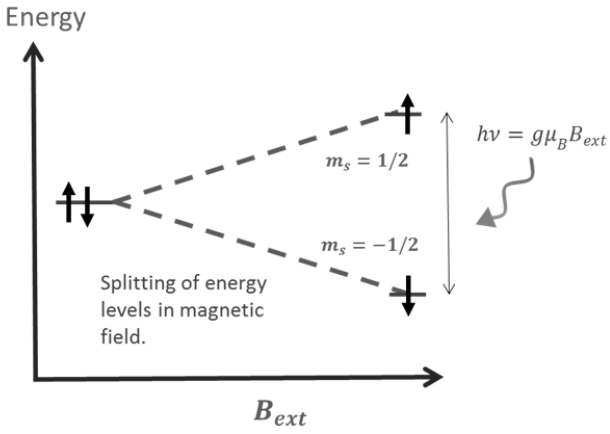

Figure 2.3 Zeeman energy split in the external field.

By applying a microwave photon with the same energy ΔE, the system resonates, and a single spin is lifted from the parallel ground state into the higher, excited state. In a paramagnetic material, this excitation is independent of other surrounding spins. But in a ferromagnetic system

with coupled magnetic moments, it is a collective excitation of all the magnetic moments. These collective excitations are called spin waves, or in a quantum mechanical term, magnons.

The magnetic moments of a ferromagnet precess around the effective field, which is caused by the overall effect of the magnetocrystalline anisotropy, shape anisotropy, spin orbit exchanges interactions, and external magnetic field. The time evolution of the magnetization is described by the Landau-Lifshitz equation (Stöhr and Siegmann, 2006) as follows:

$$\frac{d}{dt}\vec{M} = -\gamma\vec{M} \times \vec{B}_{eff} + \frac{\alpha}{M_s}\left[\vec{M} \times \frac{d\vec{M}}{dt}\right], \qquad (2.5)$$

where α is the Gilbert damping factor, which is caused mainly by the lattice coupling (it is not explicitly included in the calculations in this work, and is implemented as the spectrum line width).

2.1.1.4 Simulation of FMR spectra

Our FMR simulation starts with modeling magnetosome chains as an ellipsoid following the model of Charilaou et al. (Charilaou, et al., 2011). In this model, a single chain or a cluster of particles is represented by an ellipsoid, and the magnetic interactions between the particles are implicitly incorporated as the uniaxial shape anisotropy of that ellipsoid. This energy is directly correlated to the elongation of the ellipsoid and describes the fact that magnetization of the ellipsoid along its long axis is energetically preferred over magnetization along its short axis, just as the interactions between the particles in a chain will favor an orientation of the magnetic moments parallel to the chain axis. The more elongated the ellipsoid, the higher the anisotropy will be. For an ideal spherical structure, there is no uniaxial anisotropy. Also, the magnetocrystalline anisotropy energy is included in the total energy. This energy describes the

effect of crystalline directions on the total magnetic energy, with characteristic (material-dependent) preferred directions of magnetization (easy axes). It has been shown that this model is sufficiently accurate for calculating the resonance fields of a randomly oriented ensemble of MTB (Chariaou, et al., 2015, Charilaou, et al., 2011). The ellipsoid's long axis corresponds to the main axis of the chain and is oriented along the z-axis. The direction of the external field and of the equilibrium magnetization of the chain (determined by all external and internal magnetic interactions) are characterized by angles $(\theta_H, \varphi_H,)$ and (θ, φ), respectively (Figure 2.4).

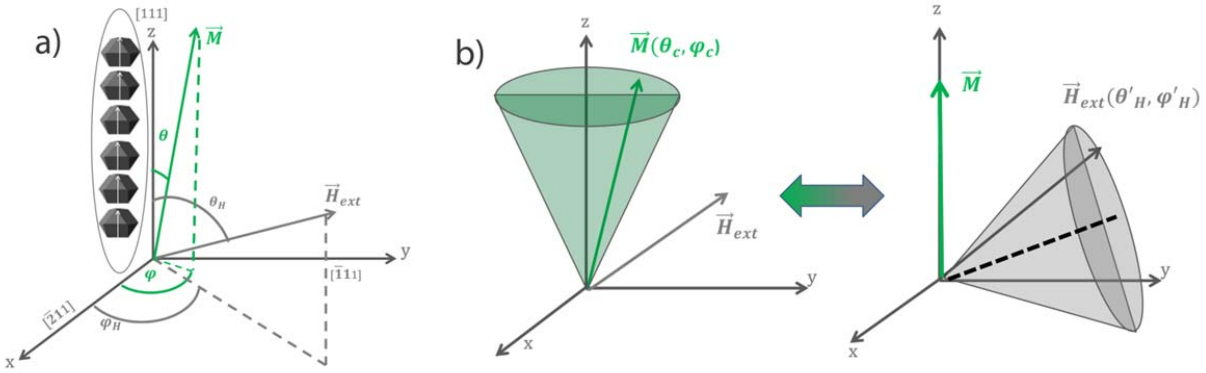

Figure 2.4 Coordinate definitions for the simulation. a) Ellipsoid model: A magnetosome chain is represented by an ellipsoid, fixed along the z axis. The easy <111> axis is also parallel to the z axis. An external field is applied at angles (θ_H, φ_H) and leads to an equilibrium orientation of the magnetic moment of the chain in the direction (θ, φ). b) In a sample, one typically has a distribution of chain orientations (θ_c, φ_c) around the z axis, which in the model is represented by the corresponding distribution of field directions that are experienced by the individual chains in their reference frame in which the chain is oriented along the z axis. These field directions (θ_H', φ_H') are distributed around the mean direction (θ_H, φ_H).

The free energy (F) contains the interaction energy of the magnetic moments with the applied field (Zeeman energy) and the internal energies due to the magnetocrystalline anisotropy and the uniaxial anisotropy:

$$F = F_Z + F_{\text{shape}} + F_{\text{cub}}. \qquad (2.6)$$

To calculate theoretical FMR spectra, the resonance field is determined for each orientation of the external field (θ_H, φ_H) (Figure 2.4) with the equilibrium magnetic moment of the ellipsoid representing the chain. Thus, to obtain the equilibrium direction of the magnetization vector $\overrightarrow{M}$, the free energy is minimized with respect to the angles (θ, φ) , $\partial_\theta F = \partial_\varphi F = 0$. This results in a set of equilibrium angles that are a function of the direction and strength of the external field, $\theta(\theta_H, \varphi_H, H)$ and $\varphi(\theta_H, \varphi_H, H)$. For resonance, the latter in turn has to satisfy the resonance condition:

$$\left(\frac{\omega_{\mathrm{res}}}{\gamma}\right)^2 = \frac{1}{\mathrm{M}^2}\left[\partial_{\theta\theta}\mathrm{F}\left(\frac{\partial_{\varphi\varphi}\mathrm{F}}{\sin^2\theta} + \frac{\cos\theta}{\sin\theta}\partial_\theta\mathrm{F}\right) - \left(\frac{\partial_{\theta\varphi}\mathrm{F}}{\sin\theta} - \frac{\cos\theta}{\sin\theta}\frac{\partial_\varphi\mathrm{F}}{\sin\theta}\right)^2\right], \qquad (2.7)$$

with $\gamma = g\mu_{\mathrm{B}}/\hbar$, (Charilaou, et al., 2011, David, 1981, Mann, et al., 1984, Sekerka, 1969). Simultaneous numerical evaluation of the free energy minimization and the resonance condition results in the resonance field as a function of the angles of the external field, $H_{\mathrm{res}}(\theta_H, \varphi_H)$.

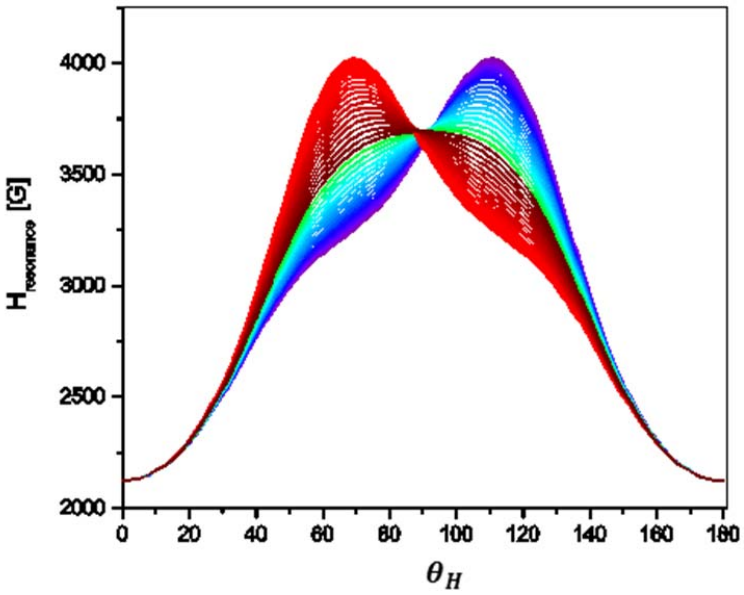

Figure 2.5 The calculated resonance field for different angles of external field. The x axis is referred to θ_H and colors show the curve for different values of φ_H.

The microwave absorption power can be derived from the imaginary part of the susceptibility tensor as a Lorentzian profile centered over the resonance field, but the inhomogeneity of the sample leads to a more Gaussian profile (Linder J. , et al. 2010).The actually measured spectrum is given by the first derivative of an absorption spectrum, because lock-in amplifiers are used in FMR experiments. Thus, the theoretical spectrum of a single cell is calculated as the derivative of a Gaussian with mean H_{res} and width ΔH:

$$S(\theta_H, \varphi_H) = \frac{-(H-H_{res})}{\Delta H^3\sqrt{2\pi}} e^{\frac{-(H-H_{res})^2}{2\Delta H^2}} \qquad (2.8)$$

Finally, FMR spectra for bulk samples that contain many cells with a distribution of orientations are obtained by superposition of spectra of the type described by eq. 2.2. Since this equation is based on the assumption that the long axis of the chain (or the ellipsoid) is oriented along the z direction, for each chain orientation the coordinate system is rotated such that the chain is along the z-axis. As a consequence, the spectra are calculated for the correspondingly rotated magnetic field. In other words, the spectrum of a bulk sample is calculated by a superposition of spectra given by eq. 2.8 with different field orientations.

2.1.1.5 Data Fitting

The following fitting procedure was used to match the theoretical and the experimental spectra and so to determine the parameters of the calculated spectra. The main emphasis was put on matching the key characteristics of the spectra. These are the field values which indicate the position of maxima, minima and the zero-crossing of the spectrum (p_1, p_2, d_1, d_2, H_{res}), and the relative intensity of these maxima and minima (Weiss, et al., 2004). These spectral features are

known to reflect the major anisotropic properties (Kopp, et al., 2006) and we take them as our reference points in the fitting procedure. In contrast, fitting the full spectrum sometimes resulted in nominally good fits that were not necessarily matching the key characteristics. We calculated a set of more than 500 theoretical spectra with different chain parameters values ($\mathrm{H_{uni}}, \mathrm{H_{cub}}, \Delta H, g$). For all theoretical spectra, the summed normalized chi-square of the positions (maxima, minima and zero crossing) was initially calculated. Within this range, the final optimal set was determined by minimizing the normalized chi-square sum of relative intensities. The parameter combinations resulting in a total chi-square below a threshold were retained as the final fit parameters for the experimental spectrum.

2.1.2 Experimental: Ferromagnetic Resonance Spectroscopy

We have performed three various types of FMR experiments depending on the measured samples. The first is in solution FMR or 3D FMR. This experiment is done on bacteria cells inside the aqueous media, using quartz EPR tubes. The second method is planar FMR or 2D, where the samples are dried on a silicon substrate. Angular dependent measurements are performed in an out of plane rotation. The third method is a single cell FMR method. Here, we use a microresonator again designed on a silicon substrate, and low concentration samples are dried on the substrate so that we have only two cells inside a microcavity. Angular dependent measurements are all in-plane for this measurement. In the following, more details on these methods are explained.

2.1.2.1 Solution FMR experiments

For FMR experiments, a 15 mL sample was taken from a bacterial culture flask and centrifuged (10 mins, 4°C, 5000 rpm). The resulting pellet was resuspended in 1 mL medium in conventional EPR tubes. The FMR experiments are performed at X-band (~ 9.3 GHz) with a Bruker CW ESP spectrometer ELEXSYS E500 at Institute of chemistry, University of Potsdam (Figure 2.6) in the group of Prof. Strauch. The spectra of the MSR-1 cells in the medium solution are recorded at a temperature of 150 K.

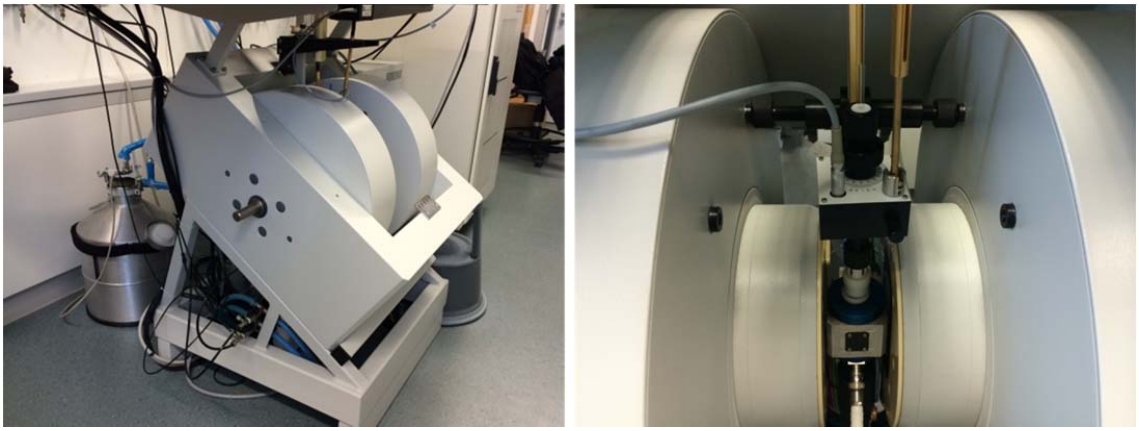

Figure 2.6 The Bruker CW ESP spectrometer.

For each sample of the studied strain, we did the measurement in two different states: The first state was a random orientation where the cells are initially frozen (150K) and fixed in the frozen medium in their random direction while the magnetic field is off. After this stabilization step, the field is switched on and the FMR experiment is performed.

After this, we performed an in-field orientation method. For this, an external magnetic field of 300 mT is applied on the cells in liquid medium, attempting to align them. Then the samples are frozen (150K) with the field remaining on, and the angular dependent FMR experiment starts.

Measuring a specific sample in two orientation states has the advantage that one can obtain a physical model from one state, which can (will) be used to test model predictions for the other state. The angular dependence is measured in steps of 10 ° from 0 to 180 °, using a mechanical goniometer to turn the sample tube inside the microwave cavity around its axis. For each angle, the field is sweeping from 10 to 610 mT. For lock-in detection of the ferromagnetic resonance, the applied magnetic field is modulated with a frequency of 30 kHz and amplitude of 1mT. All the experimental spectra were drift corrected and normalized to their maximum.

2.1.2.2 FMR planar experiment

The FMR experiments are performed at X-band (~ 9.3 GHz) with a Bruker CW ESP spectrometer ELEXSYS E500 in the group of Prof. Farle of the University of Duisburg. The applied magnetic field was swept from 0 to 700 mT with a modulation of 30 kHz and amplitude of 1.5 mT. The measurements were done in a conventional cavity.

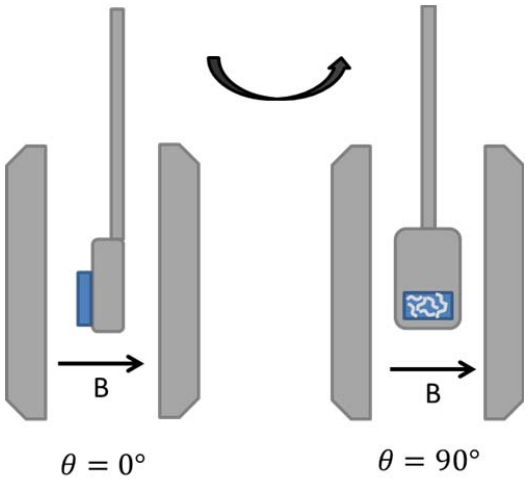

Figure 2.7 Schematic view of the sample position inside the cavity.

For this measurement a 10 μL droplet of the bacterial sample are placed and dried on a silicon substrate and the substrate is placed on a sample holder so that the magnetic field direction is perpendicular to the substrate plane. By rotating the sample holder, the field will change from an out-of-plane direction to in-plane direction. Temperature dependent FMR was also performed for the angles 0 & 90 °, starting from room temperature, passing through the Verwey transition at~110K, and cooling down until 100K.

2.2 X-ray Photoemission Electron Microscopy

2.2.1 Theory of X-ray Photoemission Electron Microscopy

Photoemission electron microscopy (PEEM) is a powerful tool for surface studies in material science, thin film magnetism, and biology (Scholl, et al., 2000). A photoemission electron microscope forms an image by collecting the emitted electrons from a solid surface. In 1905, Einstein proposed the idea of the photon as light quanta and explained the photoelectric effect

regarding a photon's energy to release an electron from a surface (Einstein, 1905). A photoemission electron microscope forms the image from the spatial distribution of electrons emitted from the surface.

Historically, PEEM was invented after the introduction of electron lenses in the early 1930s. Brüche built the first photoemission electron microscope, which worked with ultraviolet (UV) light to image photoelectrons emitted from a metal (Brüche, 1933). The principle design of his PEEM is still used. In Brüche's PEEM, UV light from a mercury lamp was focused by quartz lens onto the sample cathode. A relatively recent development is the substitution UV radiation with X-rays. In 1993 Stöhr *et al.* (Stohr, et al., 1993) showed the possibility of high-resolution imaging of magnetic domains with XPEEM. XPEEM instrumentation has evolved rapidly during the past decade, and almost every major synchrotron facility is now home to a PEEM instrument. PEEM is limited in resolution by the chromatic and spherical aberrations of the electron lenses. It has been shown that an aberration corrector can improve the resolution down to 1 nm (Fink, et al., 1997). The "SMART" PEEM at BESSY II (Feng, et al., 2005, Schmidt, et al., 2002) is one of the aberration-corrected XPEEMs.

2.2.1.1 The X-Ray Absorption and Photoemission Process

X-ray photoemission electron microscopes are mostly operating in an energy range of 80-2000 eV, called the soft X-ray regime. This covers the absorption edges of many important elements, particularly the transition metal ferromagnets. The electron optics of the XPEEM experiment image the photoelectron yield of the sample with magnification onto a detector, usually a

phosphor and a charge coupled device (CCD) camera. The CCD digitizes the signal, which can later be processed by PCs.

When matter absorbs X-rays, electrons are excited from core levels into unoccupied states, leaving empty core states. Secondary electrons are excited by the decay of the core hole. Auger process and inelastic electron scattering create a cascade of low energy electrons, of which some penetrate the sample surface, escape into the vacuum, and are collected by the PEEM optics. The secondary electron intensity, which closely follows the X-ray absorption spectrum of the sample, determines the XPEEM intensity (Stöhr and Siegmann, 2006).

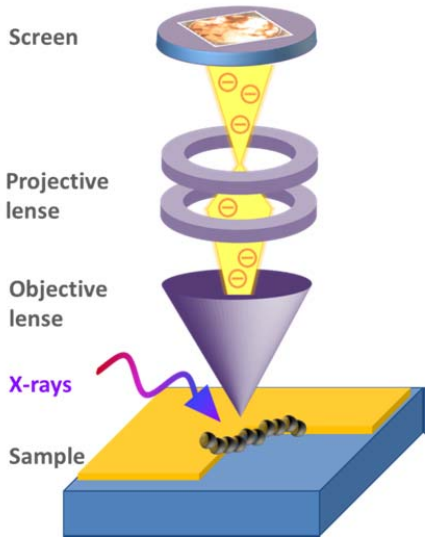

Figure 2.8 Schematics of a photoemission electron microscope adapted from (Kronast, et al., 2011)

In the case of X-ray illumination, the distribution of the low-energy secondary electrons can be approximated by $n_e = E/(E+W)^4$, where E is the kinetic energy and W is the work function of the material. The electrons have an energy spread about 20 eV, around the average energy. (Feng and Scholl, 2007). This energy spread perturbs the spatial resolution through chromatic

aberrations. Fortunately, a suitable aperture, placed behind the focal plane of the PEEM, reduces the effective width of the energy spread. Thus, in principle a spatial resolution of ~20 nm can be obtained with the energy filtering (Anders, et al., 1999).

The total electron emission of the sample is proportional to the X-ray absorption coefficient. PEEM images the lateral electron emission and thereby maps the local X-ray absorption of the sample as a function of X-ray energy. Local X-ray absorption spectra are obtained by monitoring the local image intensity while scanning the X-ray energy. Therefore, XPEEM is a full-field imaging technique, and spectra from many image points are taken in parallel (Feng and Scholl, 2007)

2.2.1.2 X-ray Magnetic Circular Dichroism

X-ray magnetic circular dichroism (XMCD) is a standard method to study magnetic thin films and surfaces. The first XMCD spectroscopy measurements were done by Schütz et al. (Schütz, et al., 1987) at the transition metal L edges. Following that and with the wide availability of polarized and tunable X-rays from synchrotron sources, X-ray dichroism techniques have significantly progressed.

An XMCD experiment is measuring the atomic magnetic moment of a ferromagnet relative to the polarization vector of the X-rays. The *d* states carry most of the magnetic moment of transition ferromagnet metals (Fe, Co, and Ni). Thus, strong XMCD effects (up to 40%) appear at $2p \rightarrow 3d$ transition, with the X-ray at their L edges energies.

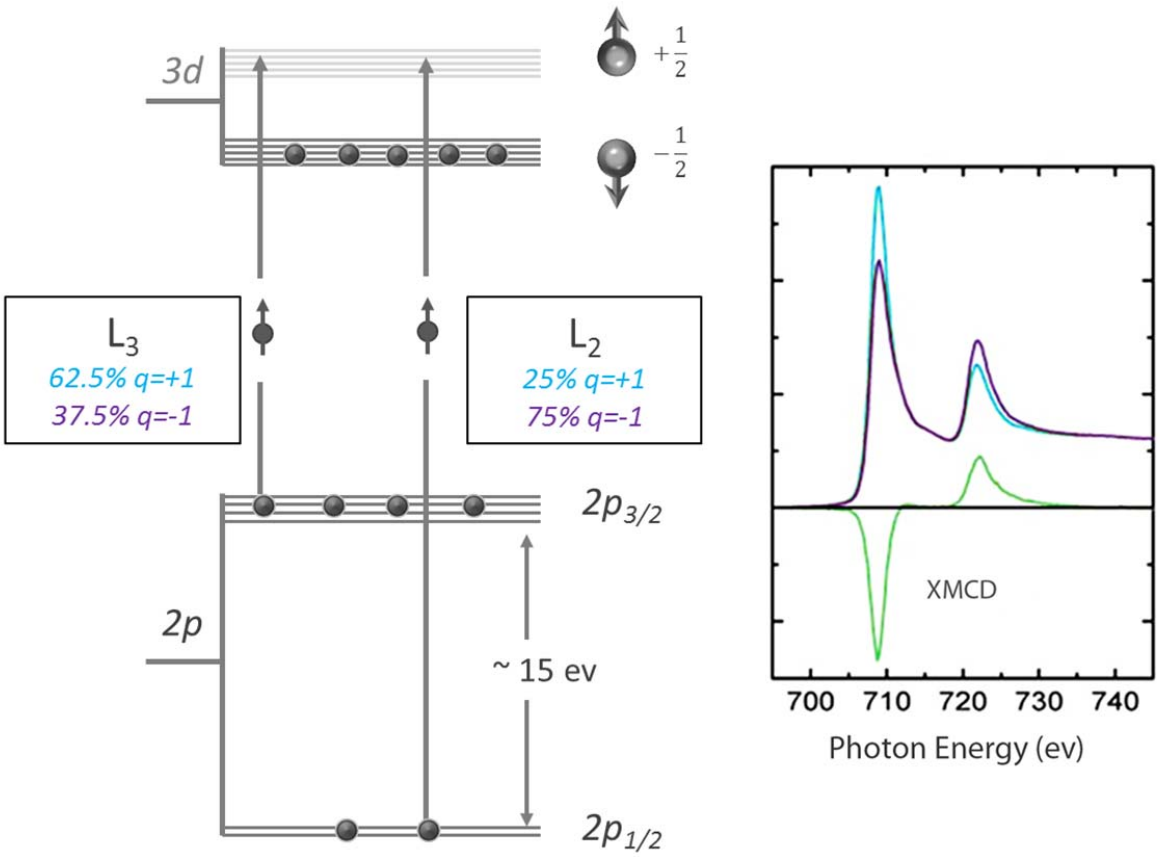

Figure 2.9 Illustration of the L-edge X-ray absorption processes of circularly polarized. We show an atomic one-hole *d* shell model of a magnetic material. In the atomic model we assume one spin-up hole and show the possible 2p core to 3d. valence transitions assuming circularly polarized light with angular momentum q. The fraction of spin-up electrons excited from the *p* core shell through absorption of X-rays with angular momentum q = ±1 is listed for the L_3 and L_2 edges. In the right side plot, purple and blue line are the XMCD L-edge absorption of photon with negative and positive momentum in Fe. The green line is the difference between these two absorptions. The two distinct peaks in L_3 (708 eV) and L_2 (721 eV) are the direct result of the spin-orbit coupling in the *p* shell. Atomic model adapted from (Stöhr and Siegmann, 2006).

The XMCD spectrum is basically defined as the absorption difference of two spectra acquired with opposite polarization. A simple atomic model can explain the quantum mechanical origin of the XMCD effect at the L-edge as shown in Figure 2.9. The sample is magnetized in the "up" direction; thus the spin-up states have higher energy than the spin-down states. Following Hund's law, the spin-down states with lower energy get filled, and the spin-up states with higher energy

are only partially filled. The spin-orbit interaction among the $2p$ core electrons causes the $2p$ states to split into separate $2p_{1/2}$ and $2p_{3/2}$ levels with different occupation numbers, namely two and four respectively. The transition of electrons from the $2p$ core shell to the $3d$ valence states occurs by the absorption of the circularly polarized X-ray. The fraction of spin-up electrons excited from the $2p$ core shell through absorption of photons with angular momentum q = ± 1 is listed for the L_3 and L_2 edges. Here we have assumed the X-rays to be incident parallel to the atomic magnetic momentum. At the L_3 edge ($2p_{3/2} \rightarrow 3d$), X-rays with positive (q = 1) photon spin excite more spin-up electrons and have higher absorption intensity than X-rays with negative (q = −1) photon spin. At the L_2 edge ($2p_{1/2} \rightarrow 3d$), it is the opposite. In a paramagnet, however, this does not lead to a change in absorption intensity, since the number of unoccupied valence states is equal for both spin directions (Wolfgang, 2004).

The XMCD is based on two steps. The first is the angular momentum transfer of the photons to the photo-excited electron from the $2p$ shell through the spin-orbit coupling. This coupling will be different for the $2p_{1/2}$ and $2p_{3/2}$levels. In the second step, the $3d$ valence shell with unequal spin-up and spin-down populations acts as the detector for the spin of the excited photoelectrons. For maximum effect, the photon spin needs to be aligned with the magnetization direction.

2.2.2 Experimental: X-ray Photoemission Electron Microscopy

2.2.2.1 Experimental Setup

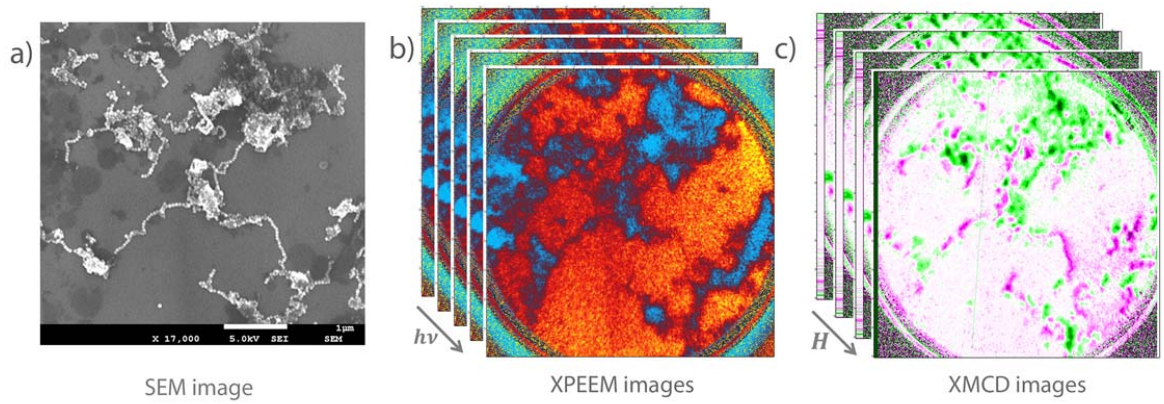

Figure 2.10 structural, elemental, and magnetic images. a) SEM image of the measured area used to study the structure and correlate them with the component and magnetic properties. The image is taken at the same field of view as the other two XPEEM and XMCD images. b) Stack of XPEEM images take at different photon energies at the Fe L3,2 edge. c) Stack of XMCD images, in a changing applied magnetic field. Each image is a result of difference between the absorption of two different X-ray helicities. The image is taken at the photon energy 707.3ev. Colors are showing the direction of magnetization. Magenta is parallel and green is antiparallel to the direction of the magnetic fields. The direction of the magnetic field is demonstrated by the black arrow.

High resolution magnetic images were taken at the SPEEM of the Bessy II storage ring in Berlin (Kronast and Valencia, 2016). This setup is based on an Elmitec III instrument with energy filter, permanently attached to an undulator beamline with full polarization, control covering an energy range from 80eV to 2000 eV. The lateral resolution of the SPEEM is about 30 nm for x-ray excitation. The XPEEM images are obtained at the Iron $L_{3,2}$ edges (700-740 eV). The intensity of magnetosomes in the images change according to the absorption and reached its maximum at ~708eV.

For magnetic imaging, the photon energy was tuned to the L3 resonance of Iron (707.3ev), to profit from the highest absorption difference between the two polarizations ($I_{neg} - I_{pos}/I_{neg} + I_{pos}$) and attain the element specific XMCD. The sample was mounted on a special sample holder, which can apply magnetic in-plane fields up to 120 mT (Sandig, et al., 2012). The imaging was performed in a series of field steps and for each field a sequence of images was taken with circular polarization (90° of polarization) and alternating helicity X-rays.

The result of the XMCD measurement in each applied magnetic field is a magnetization map, and from all the measured fields, a stack of XMCD images are obtained.

2.2.2.2 Data Analysis

Each of the displayed XMCD images has been calculated from a sequence of images taken with circular polarization (90 ° of polarization) and alternating helicity. After normalization to a bright field image, the sequence has been drift corrected, and frames recorded at the same photon energy and polarization have been averaged. The Fe magnetic contrast is displayed as the difference between the two average images with opposite helicity, divided by their sum. The magnetic contrast represents the magnetization component pointing along the incidence direction of the x-ray beam. The XMCD map represents the magnetization for every magnetosome arrangement, in a changing field. We extract the coordinates of each region of interest, and since the images are drift corrected, the coordinates are consistent throughout the stack. Then, we derive the XMCD intensity of the corresponding structure from every magnetic map and plot them as the remanence curve for each magnetosome structure. The SEM image is also correlated with the XMCD image so that the magnetic behavior can be directly correlated with the magnetosomes arrangement.

2.3 Magnetotactic Bacteria

Magnetotactic bacteria (MTB) are motile prokaryotes found in freshwater and marine environments. Bellini (Bellini, 1963) and Blakemore (Blakemore, 1975), have independently discovered the magnetoresponsive feature of these microorganisms, by observing their consistent

swimming toward a magnetic field. The bacteria use magnetic navigation, called magnetotaxis, to swim along the geomagnetic field. This presumably helps them to optimize the search for their proper habitat with sufficient oxygen concentration, in a one-dimensional excursion (Frankel, et al., 1997). Electron microscopy images of the bacteria cells have shown arrangements of nanoparticles located inside the cells (**Error! Reference source not found.**). These particles called as magnetosomes are magnetic minerals of magnetite (Fe_3O_4) {Stolz, 1986 #233} or in some cases greigite (Fe_3S_4){Lefèvre, 2011 #232}. They are responsible for the magnetic response of the cells by aligning passively with the magnetic field. Today several different species of MTB are known, and they exhibit a broad range of diversity in cell morphology and magnetosome size, number and configuration. There are vibrios, rods, spirilla, cocci, as well as multicellular forms, with various magnetosome in a range of 30-100 nm mostly in a chain or multichain structures (Bazylinski and Frankel, 2004, Isambert, et al., 2007).

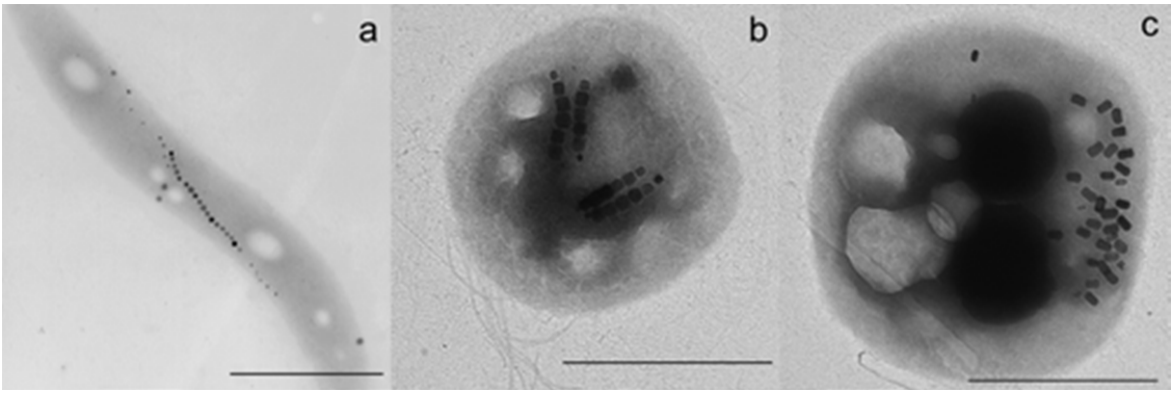

Figure 2.11 Electron macroscopy images of different MTB cells. The diversity of the cell morphology and magnetosome arrangement and shape, is shown. (a) a spirillum with a single chain of cubooctahedral magnetosomes, (b) a coccus with two double chains of slightly elongated prismatic magnetosomes, (c) a coccus with clustered, elongated magnetosomes. Scale bars in represent 1 μm (Faivre and Schüler, 2008), adapted with permission from the author.

Among all the discovered strains, a limited number of them could be cultured in the laboratory, for instance the *Magnetovibrio blakemorei* MV-1, *Desulfovibrio magneticus* RS-1, and

magnetococcus MC-1 (Bazylinski, et al., 1988, Meldrum, 1993, Sakaguchi, et al., 1996). But the most developed strains are *Magnetospirillum gryphiswaldense* strain MSR-1 (Schleifer, et al., 1991) and *Magnetospirillum magneticum* strain AMB-1 (Matsunaga, et al., 1991). Species from the genus *magnetospirilla* are genetically tractable, thus have advanced as the most studied model systems (Uebe and Schuler, 2016).

2.3.1 *Magnetospirillum gryphiswaldense* MSR-1

In *Magnetospirillum gryphiswaldense* MSR-1, a ~ 40 nm magnetite crystal nucleates and grows inside a vesicle. This structure is known as the magnetosome (Mann, et al., 1984). Such vesicle is composed of a ~ 5 nm phospholipid bilayer with several membrane-associated proteins that control the chemical condition and iron transport, and are crucial for the biological control of the chain formation (Faivre, 2015, Grünberg, et al., 2004).

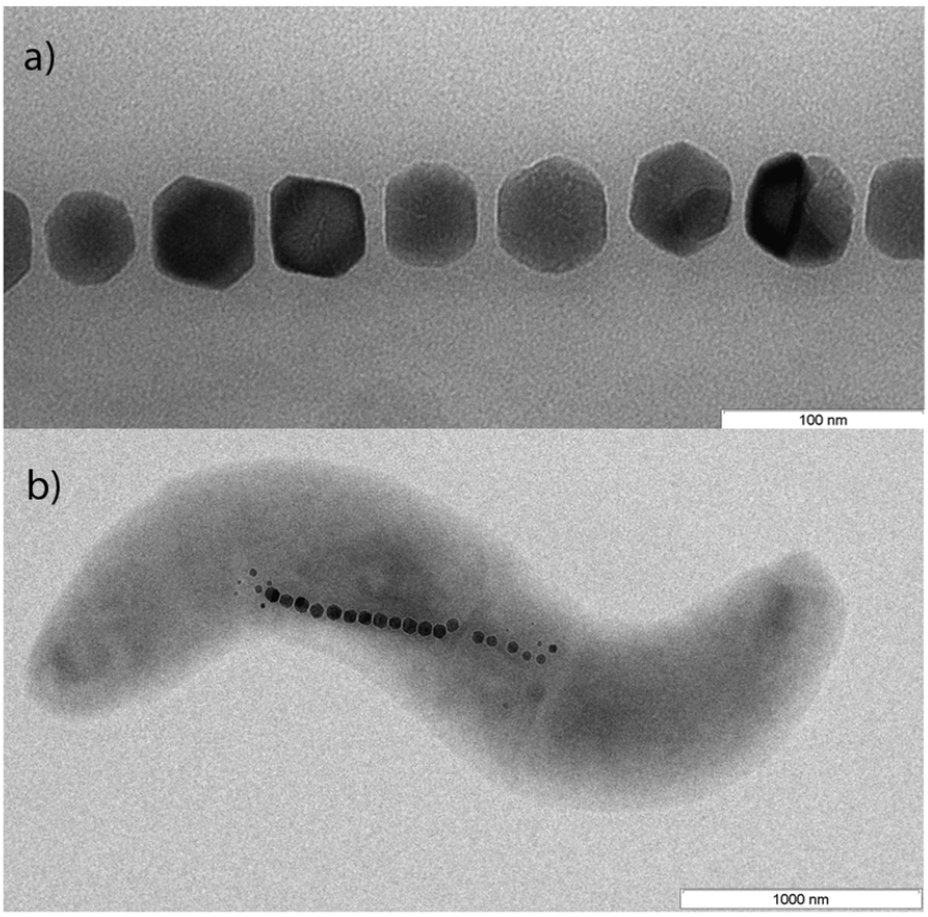

Figure 2.12 Transmission electron microscopy image of an MSR-1 cell. a) The magnetosome chain structure. b) MSR-1 cell with the magnetosome chain inside the cell.

The magnetosome complexes are arranged in a 1D chain assembly (Figure 2.12). The particles are stabilized by being connected to a cytoskeleton-like structure called the magnetosome filament. This filament is mainly made of a protein named MamK (Katzmann, et al., 2010). A connection between the filament and the vesicle occurs *via* the magnetosome connector MamJ, which is another protein specific to the MTB (Scheffel, et al., 2006). It has been shown that purely passive magnetic interactions of magnetic nanoparticles, will not guide to such a robust chain formation (Klumpp and Faivre, 2012).

The magnetosomes in the chain align along their [111] crystalline direction, which is the easy axis of magnetization of magnetite, all in parallel with the chain main axis (Faivre, 2015, Körnig, et al., 2014). This configuration maximizes the magnetic dipole moment of the chain and thus enables most efficient orientation of the cell in the Earth's magnetic field while swimming (Lefèvre, et al., 2011). This specific arrangement also exhibits characteristic anisotropy traits, which result from both the cubic magnetocrystalline anisotropy of individual crystals, and from the uniaxial fields generated by the dipole interactions between magnetosomes aligned in the chain (Charilaou, et al., 2011, Fischer, et al., 2008, Kopp, et al., 2006, Körnig, et al., 2014).

2.3.2 MSR-1 mutants: Δ*mamK and* Δ*mamJ*

The magnetosome organization can change by genetic modifications. As explained in the previous section, the two *mamK* and *mamJ* genes have been discovered to play a major role in the chain assembly of the MSR-1 strain. While MamK protein is suggested to form magnetosome-associated cytoskeletal filaments, MamJ is assumed to attach the magnetosome vesicles to these structures. In a *mamK* deletion strain, the magnetosome-associated cytoskeleton is absent, and the individual magnetosomes no longer form the typical magnetosome chain but instead organize in shorter and fragmented (Katzmann, et al., 2010, Komeili, et al., 2006).

The deletion of the *mamJ* gene in MSR-1 abolishes the formation of the chain normally seen for the wild type (WT). In the Δ*mamJ* mutant, magnetosomes instead form clusters within the cells (Scheffel, et al., 2006). The Δ*mamJ* mutant is however not further affected in biomineralization and forms wild type-sized and -shaped magnetite crystals. MamJ protein is known to interact with the MamK filament and to lead the localization of the magnetosomes in along the filament (Scheffel and Schüler, 2007)

2.3.3 MSR-1 mutant Δ*F3*

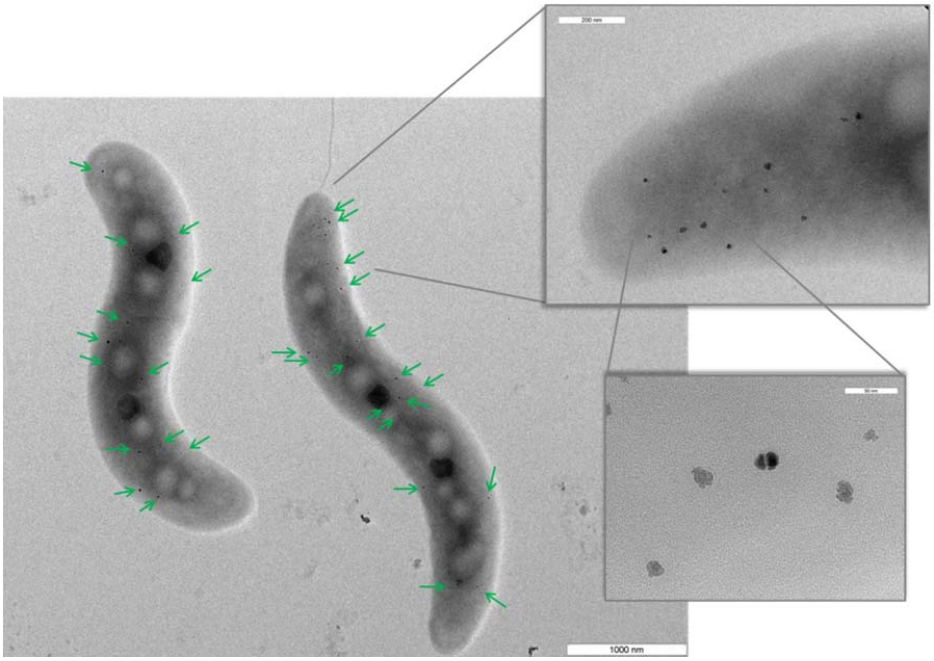

Figure 2.13 MSR-1 mutant Δ*F3*. This mutant produces scattered magnetite particles with an average diameter of ~23.6 nm and ~24 particles per cell.

The strain Δ*F3* is a MSR-1 mutant in which the three highly homologous genes *mamF*, *mmsF*, and *mamF2* have been deleted (Dr. René Uebe, University of Bayreuth, Department of Microbiology; unpublished). The proteins encoded by these genes are speculated to regulate magnetite crystal nucleation and growth by direct interaction with iron ions or the magnetite surface (Murat et al. 2012; Rawlings et al, 2014; Lohße, et al., 2014). Consequently, the magnetite particles formed by the Δ*F3* strain are smaller than those of the wild type. However, as shown in the TEM images of Figure 2.13, this mutant is also unable to form magnetosome chains and the particles are scattered all over the cell. Cryo-electron tomography has shown that most of the magnetosomes are located close to the membrane. But it is not clear whether they are connected to the cytoplasmic membrane or not (Uebe et al, unpublished).

Widdrat *et al.* have performed high resolution TEM analysis of the magnetosomes isolated from the Δ*F3* mutant (Taukulis, et al., 2015) and characterized their size distribution and shape factor of them. From their study, the average particle size is ~ 23.6 nm and the shape factor (width / length) is 0.975, thus almost isotropic. Furthermore, 60% of particles were reported to be twinned or aggregated. Kumari *et al.* have done first order reversal curves (FORC) measurements on these magnetosomes, and concluded that the sample was mostly superparamagnetic particles with no dipole interactions between them (Kumari, et al., 2014).

2.3.4 Cell Culture

Magnetospirillum gryphiswaldense strain MSR-1 (DSM 6361) as well as Δ*mamJ* and Δ*F3* mutants were used in this study (Faivre and Godec, 2015, Scheffel, et al., 2006). The medium has been prepared as in (Faivre, et al., 2008). Briefly, 20 mL of cells from a subculture are transferred to the 200 mL medium in 0.5 L rubber sealed flasks, with micro-aerobic conditions (1 % O_2 in the headspace). Then, the flasks are incubated under gentle shaking (100 rpm) at 28 °C for 24 hours, and 72 h for Δ*mamJ* and Δ*F3* (Heyen and Schüler, 2003).

2.3.5 Magnetosome Isolation

The cells of *Magnetospirillum gryphiswaldense* strain MSR-1 were grown in 5 L medium at 28 °C and 130 rpm in a 10 L flask (Lohße, et al., 2016). After 24 h of incubation cells were harvested by centrifugation (15 min, 10.500 g, 4°C), washed twice with ice-cold 20mM Hepes (pH 7.4), 5mM EDTA and pelleted in a 50ml Falcon tube by centrifugation at 14.500 g, 4°C for 10 min. The cell pellet was stored at -20°C until use.

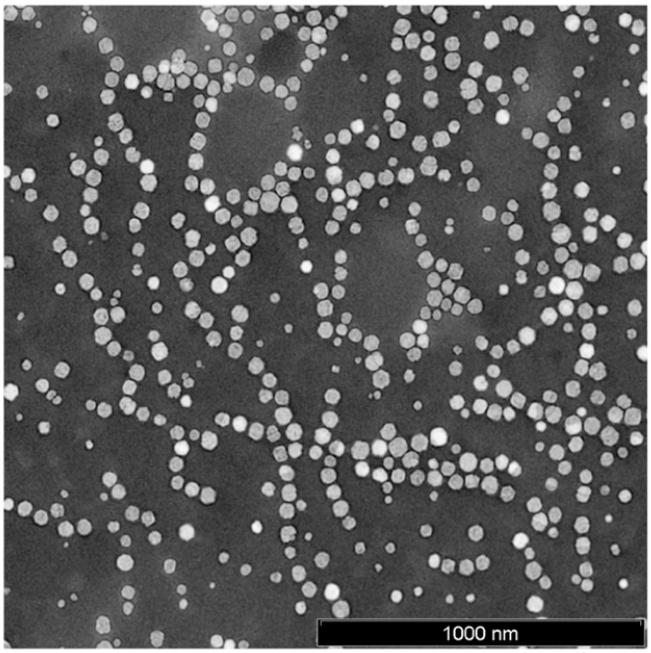

Figure 2.14 TEM image of isolated magnetosome chains from MSR-1 cells.

For the magnetosome isolation, I used a cell disruptor and applied three times a pressure of 2 kbar for disrupting the cell membranes. Then the cell debris was centrifuged (1000 rpm, 5 min, 4 °C) and the supernatant was transferred to a glass beaker. Next, the magnetosomes were collected by placing a magnet on the beaker's wall. Finally, the accumulated magnetosomes, were washed 5 times with washing buffer, high salt buffer and extraction buffer. A different method for extracting the magnetosomes was performed by Dr. Rene Uebe (University of Bayreuth, Department of Microbiology) where cell disruption was done with a microfluidizer processor, magnetic separation, and ultracentrifugation as described in Kraupner *et al.* (Kraupner, et al., 2017). This method resulted in isolated chains with higher purification, and thus I used them for the experiment (Figure 2.14).

2.4 Magnetite

Magnetite Fe_3O_4 is one of the most studied ferrimagnetic compounds. (Goya, et al., 2003, Rozenberg, et al., 2006, Simpson, et al., 2005, Subías, et al., 2004). Magnetite has a face centered cubic lattice with an inverse spinal structure. Magnetite crystalizes with the inverse spinel structure with the formula $[Fe^{3+}]_A[Fe^{3+}Fe^{2+}]_BO_4$, with the tetrahedral (A) and octahedral sites (B). The tetrahedral sites are all occupied by ferric Fe^{3+} ion ($\approx -5\mu_B$). The ferrous Fe^{2+} ($\approx 4\mu_B$) and the remaining Fe^{3+} ($\approx 5\mu_B$) cations are distributed in the octahedral sites (B). The tetrahedral and octahedral sites form two magnetic sublattices with antiparallel spins. This results a ferrimagnetic order and the excess magnetic moment per formula will be $(5_B + 4_B - 5_A)\mu_B = 4\mu_B$ (Goering, et al., 2006).

The spinal structure leads to magnetite's crystalline magnetic anisotropy. The [111] direction along the cube diagonal is a preferred direction of magnetization called as the magnetic easy axis and the magnetic hard axis is along the [100] edges.

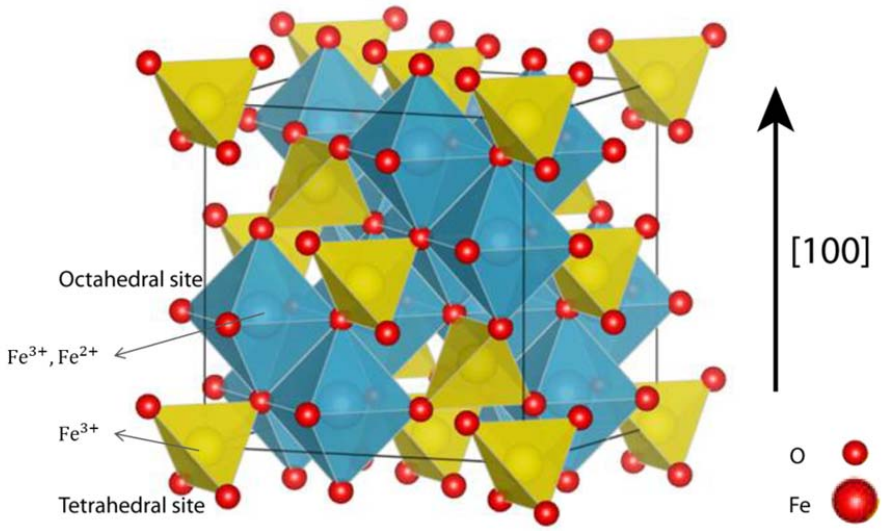

Figure 2.15 Inverse spinel structure of magnetite.

Magnetite is one of the highest magnetic minerals with a magnetic saturation 480 kAm^{-1}at room temperature. A remarkable phenomenon that happens in magnetite is the Verwey transition. Verwey discovered a sudden change in the conductivity of magnetite at temperatures below 125K (Verwey and Haayman, 1941). The Verwey transition is also reflected in many other physical properties such as jump in the magnetic susceptibility, sharp peak in specific heat, and change of crystalline symmetry from cubic to monoclinic (Özdemir, et al., 1993, Zhang and Satpathy, 1991). The reason for such a behavior is known to be in the presence of the mixed-valence in the B sites, with a hypothesis that electronic exchange between ferrous and ferric ions is different below and above the Verwey transition (Chiba, et al., 1975). But still, there are several ongoing studies for answering this question (Chang, et al., 2016).

2.5 Electron microscopy

2.5.1 Scanning Electron Microscopy (SEM)

SEM imaging was performed on JEOL JSM-7500F microscopes. For sample preparation, a few μL of magnetosome suspension were deposited on Si substrates and air-dried. The Si substrates were partially coated by a sputtered mixture of Pd (20%) and Au (80%) nanoparticles. The coating border has been utilized as a marker for localizing the magnetosome chains on the substrates for further microscopies such as Photoemission electron microscopy (PEEM). The SEM images were used for structural and configuration analysis of the magnetosomes.

Figure 2.16 Sputtered pattern on the SEM substrate. The magnetosomes are placed on the cross section of the layeres.

2.5.2 Transmission Electron Microscopy (TEM)

Samples of bacterial cells, with optical density (OD) higher than 0.2 at λ = 565nm, were washed and centrifuged (5000 rpm, 5 min, and 4 °C) for 2-3 times with milli-Q water. 20 μL of highly concentrated bacteria suspension or isolated magnetosomes solution were placed on top of the carbon coated TEM grids for 15 min. After this the liquid is removed with Kimwipe paper and

grids are rinsed with a drop of milli-Q water to remove residual salt precipitates. Imaging was performed on Zeiss EM 912 Omega with 120 kV acceleration voltage.

3 Results and Discussion

This chapter presents the anisotropy analysis of various magnetosomes configurations in both intact and isolated forms. The first two parts of the chapter are the FMR experimental results and theoretical analysis of spectra for different MSR-1 strains. The following part of the chapter presents how the formulated work in magnetic anisotropies derivation is validated utilizing XPEEM. The final section is an example of the application of the anisotropy analysis, for verifying the success of embedding magnetosome chains in calcite crystals.

3.1 FMR Spectroscopy of Different MSR-1 Strains

This section presents the ferromagnetic resonance (FMR) results for studying the structural and magnetic properties of the magnetosomes. The section starts with reviewing the experimental results of WT MSR-1, Δ*mamJ,* Δ*F3* cells and analyzing their spectral features. More quantitative analysis is presented in the simulation section. After this the results of an FMR experiment on single MSR-1 cells, will be presented. Finally, I will discuss how the structural properties of the sample can be inferred from the FMR spectral features.

3.1.1 FMR Experimental Results

3.1.1.1 Randomly Aligned *versus* Oriented Wild type Cells

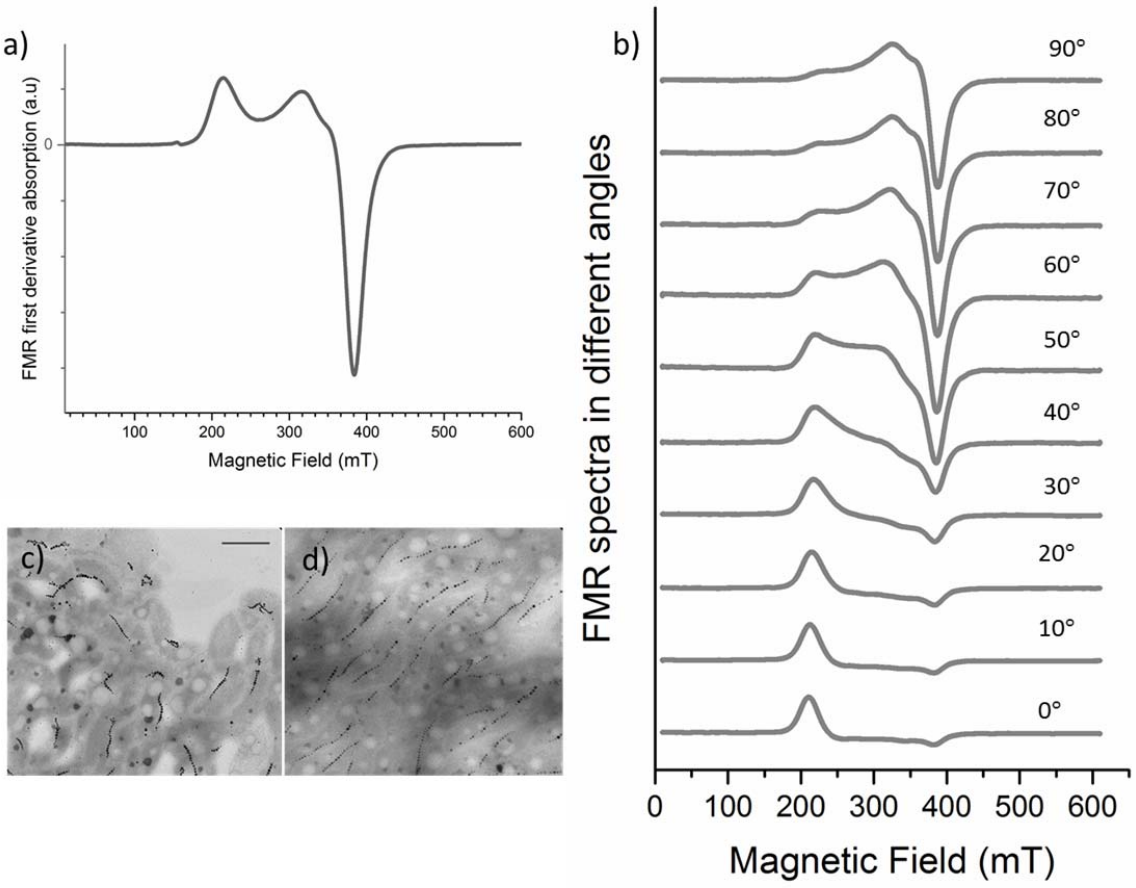

Figure 3.1 FMR experimental spectra of WT cells. a) Randomly oriented cells. b) Oriented cells in different angular measurements. For different angles the positions of the maxima and the main minimum are the same. c) TEM image of MSR-1 randomly oriented cells. d) TEM image of MSR-1 WT cells, dried in the presence of an external magnetic field.

Two sets of FMR measurements are performed on the MSR-1 WT cells (Figure 3.1). The first experiment is performed with randomly oriented cells, where the liquid solution of sample is frozen when there is no magnetic field applied and the cells are fixed in their random direction

(Figure 3.1 a,c).The second experiment is on samples aligned in a magnetic field. This sample was frozen after applying the field, thus was fixed in the oriented configuration (Figure 3.1 b,d). The TEM images of WT samples show how the chains are positioned in both random and aligned cases (Figure 3.1 c,d). The chain structure is almost stable, due to rigid connection of magnetosome to the cells' cytoskeletal filaments.

For a sample of randomly oriented WT cells, the spectrum Figure 3.1a has the typical form already measured for magnetosome chain structures, with double peak at positive intensity and one higher peak in negative intensity (Abraçado, et al., 2014, Fischer, et al., 2008). The low field maximum (in a range of 200-300 mT) and high field minimum (around 380-400 mT) and the asymmetry of their intensity ($A = p_1/d_2 \neq 1$), are the other significant features of the spectrum. This characteristic form of the spectrum is due to randomly oriented uniaxial anisotropy axes (Fischer, et al., 2008, Kopp, et al., 2006, Mastrogiacomo, et al., 2010, Weiss, et al., 2004). The spectrum shape did not change in different angles of measurement, since the orientations of the chains are uniformly distributed in all angular directions.

In contrast, the sample with pre-aligned cells (Figure 3.1b) does not cover the whole axial orientation space and therefore has angular dependent spectra. By changing the angle of measurement around the frozen aligned sample, the spectrum shape changes. The high intensity peak positioned at 210 mT gets lower, and small negative peak at ~380 mT gets more pronounced. Through this modulation, the positions of the maxima and minima remain fixed, while their amplitude changes.

3.1.1.2 *ΔmamJ* Mutant's Free Particles Arrangements

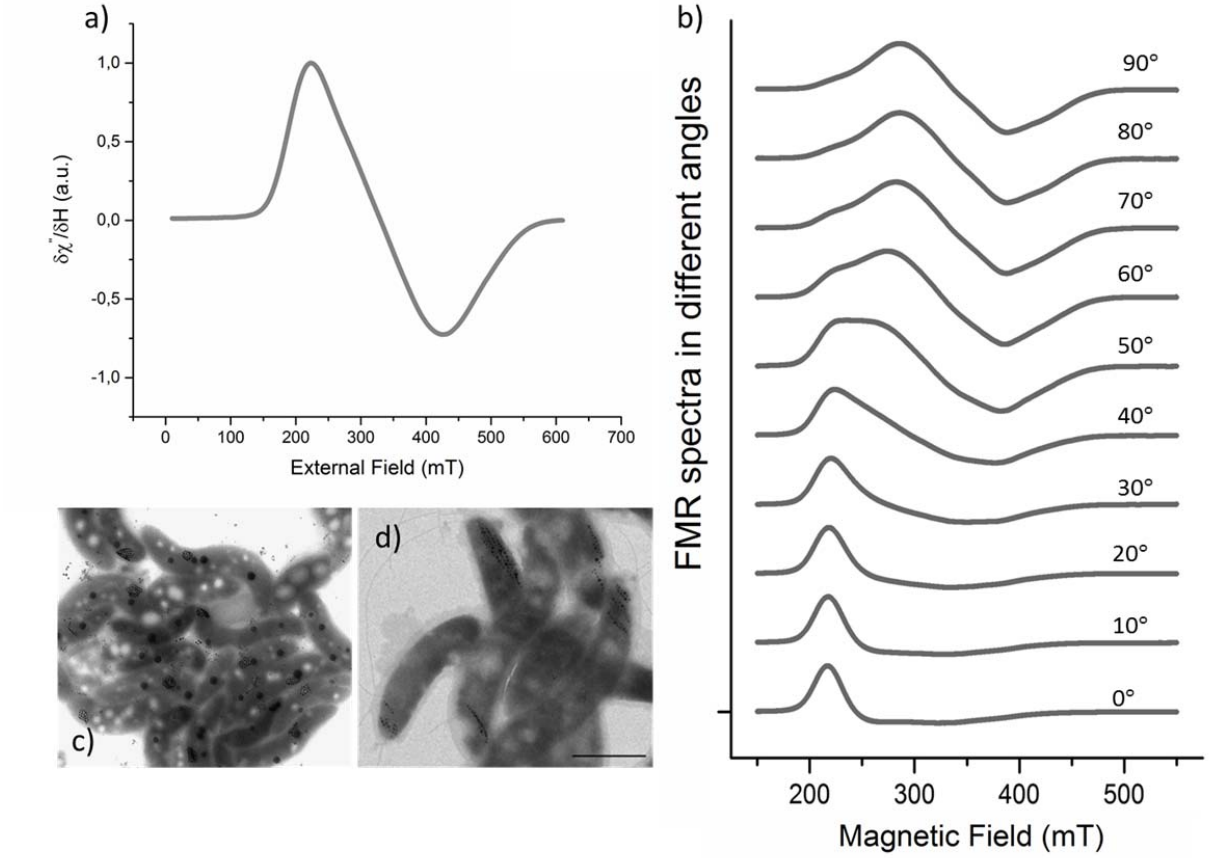

Figure 3.2 FMR experimental spectra of Δ*mamJ* cells. a) Randomly oriented cells. b) Spectra of cells oriented with a magnetic field and frozen. Different spectra are for changes of angular measurements. c) TEM image of Δ*mamJ* randomly oriented cells. The magnetosomes form a isotropic cluster. d) TEM image of Δ*mamJ* cells, dried in the presence of an external magnetic field. The magnetosome cluster gets elongated with the field. The scale bar in the TEM images represents 1 μm.

The FMR experiment for the *ΔmamJ* cells has been also performed in two different sets. One freezing the sample with no applied magnetic field (called as randomly oriented measurement). The second experiment was done on samples that where frozen after applying a directional magnetic field (called as the oriented measurement).

Compared to the WT spectrum, the spectrum for randomly oriented Δ*mamJ* cells is almost symmetric about the zero crossing point, with the intensities of the maximum and minimum in the same range (Figure 3.3 a). The spectrum had no angular dependency and was not changing in different angles of measurement. The second experiment, with post field freezing, showed that the spectra have a different line shape and strong angular dependency. The spectrum is asymmetric in 0° and changes to a more symmetric line while it gets close to 90°.

In contrast with the WT, the *ΔmamJ* cells lack the MamJ protein that connects magnetosomes to the cytoskeletal magnetosome filament. Thus the magnetosomes form an isotropic cluster, instead of a chain. The cluster does not transfer magnetic field's torque the cells to align them. But rather, the field affects the intracellular magnetosome arrangement itself. In the presence of a magnetic field the isotropic clusters of magnetosomes changes to elongated clusters or short chains with the long axis in the direction of the field (Figure 3.2 c,d), consistent with earlier observations (Körnig, et al., 2014). Thus, differences between the spectra in the two measurements also reflect different magnetosome arrangement. For oriented cells, the asymmetry of the spectra is higher in lower angles and at angles close to 90° gets more symmetric.

Temperature dependent measurements on the randomly oriented Δ*mamJ* cells (Figure 3.3), are performed as well. This is to test the effect of H_{cub} changes on the FMR spectra of these cells, since H_{cub} changes with the temperature (Bickford, 1950). In the experiment, the temperature increase does not alter the features of the spectrum and thus, the magneto-crystalline anisotropy cannot play a role in the spectrum of *ΔmamJ* cells with isotropic magnetosome clusters. This is consistent with the absence of a consistent crystallographic orientation in this magnetosome arrangement.

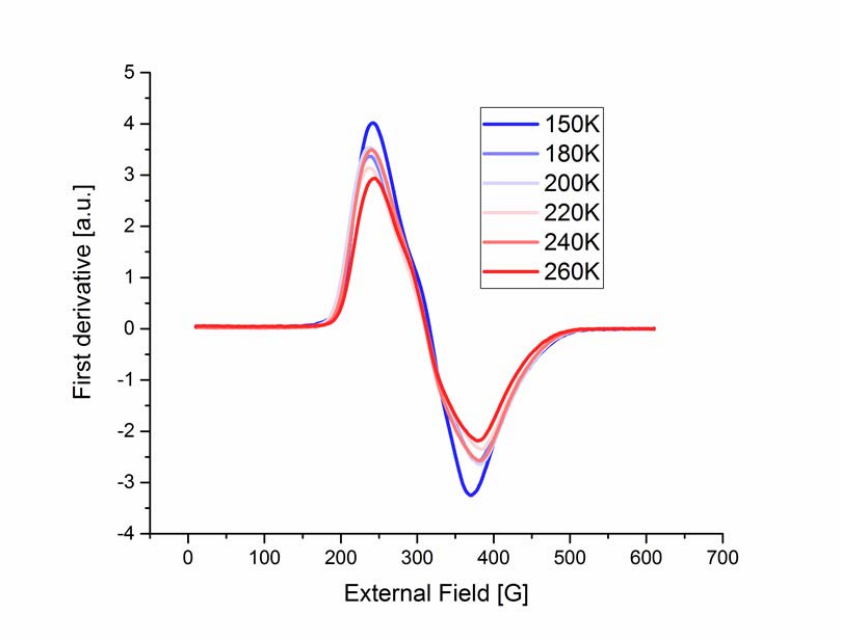

Figure 3.3 FMR spectra for Δ*mamJ* at different temperatures.

3.1.1.3 Scattered Individual Magnetosomes in Δ*F3* Cells

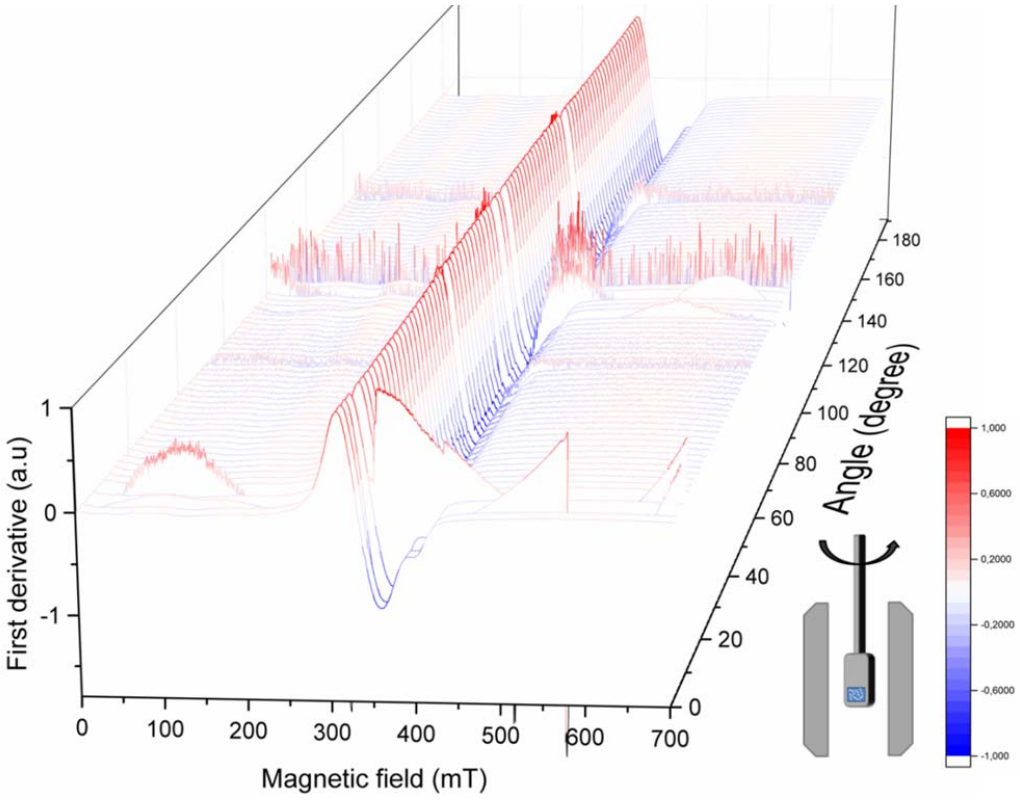

Figure 3.4 Angular dependent FMR spectrum measured at room temperature. The signal intensity is normalized to its maximum and has arbitrary units. The color is correlated to the signal intensity and the zero intensities are colored white. The rotation starts from the applied field being out plane. Some parts of the spectra are noisy (close to 140°), which according to the time of the measurement can be correlated with some electricity fluctuations.

Two sets of FMR measurements are performed on these cells. The first is an angular dependent FMR at room temperature for studying the uniaxial or crystalline anisotropy of the sample and then a temperature-dependent FMR respectively at 0° and 90° angles. This can reveal the effect of the magnetocrystalline change on the spectral shape.

The angular dependent measurement (Figure 3.4) was performed starting from the magnetic field being perpendicular to the plane ($\theta = 0°$) and continuing to in-plane field ($\theta = 90°$), and ending at $\theta = 180°$. The spectrum line shape does not show strong angular dependence.

The color code in the spectrum is correlated with the intensity. For positive intensities it is coded with red, for negative with blue, and white indicates zero intensity. The zero points in the first derivative curves are the maximum intensities in the absorption lines (integration of FMR spectrum), and known as the effective resonance field.

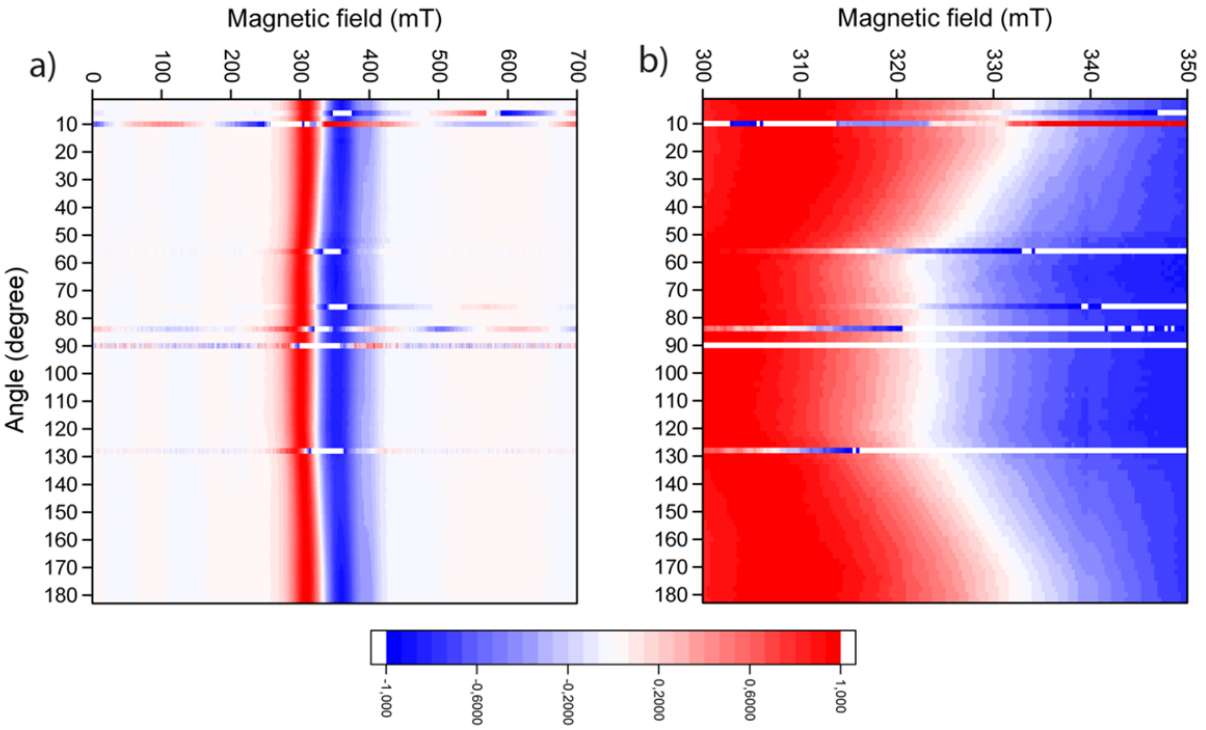

Figure 3.5 Heat map of the FMR spectrum. The color red is for the positive intensity (peaks), blue for the negative intensities (dips), and white is where the intensity is zero, which between 300-400 mT is the zero crossing point correlated with the maximum absorption. a) The full field range of the spectrum.b) a closer look at the field range of 300-350 mT. At this range one can see a periodic angular dependency of the spectrum.

In Figure 3.5, the heat map of the FMR spectra is plotted for a better view on the main spectral features. In Figure 3.5a, the white line passing through the middle of the graph is correlated with the points where the FMR spectra are passing the zero line and has zero intensity. In other words, this is the resonance field pattern in a rotating field. In a wide field range, the resonance field

seems to be almost constant. But in a narrower field range, it actually has a periodic angular dependency with a two-fold symmetry (Figure 3.5b).

As mentioned before, the second set of experiments are the temperature dependent FMR. The magnetocrystalline anisotropy of magnetite is strongly dependent on temperature (Bickford, 1950) and in low temperatures around 110K the crystal goes through the Verwey transition (Rozenberg, et al., 2006). This causes the crystalline anisotropy constant to change its sign from negative to positive and can be observed by the line shape change in FMR (Gehring and Charilaou, 2011)

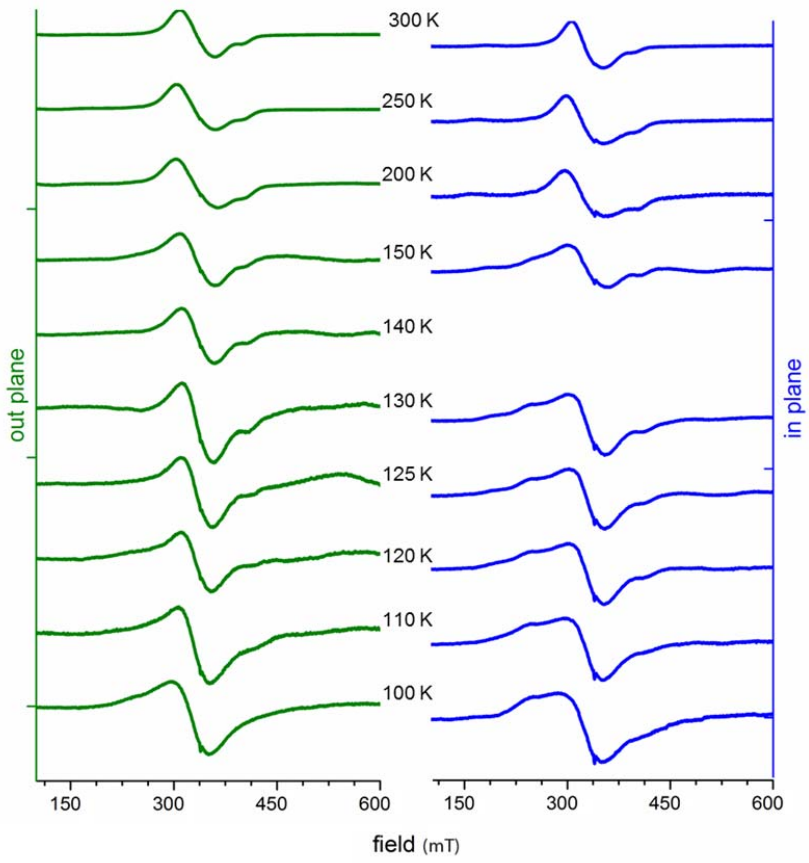

Figure 3.6 Temperature dependent FMR spectra. The spectra are recorded at two angles of 0 (out-plane) and 90 (in-plane) degrees. The crystalline anisotropy changes with temperature and this can be observed in the spectrum line change.

In both cases of out-plane and in-plane measurements, the line shape changes are qualitatively matching. Only, the appearing and vanishing shoulders are less pronounced for the out plane measurement. The spectrum line has a small shoulder at the negative peak around 370 mT when it is measured in 300K. This shoulder starts vanishing as the temperature decreases until at 120 and 110 K its almost disappeared. This can be noted as the isotropic temperature (T_i) where the crystalline anisotropy is zero. In lower temperatures, another shoulder starts appearing at the positive peak around 300mT. This can be a result of the crystalline anisotropy sign change.

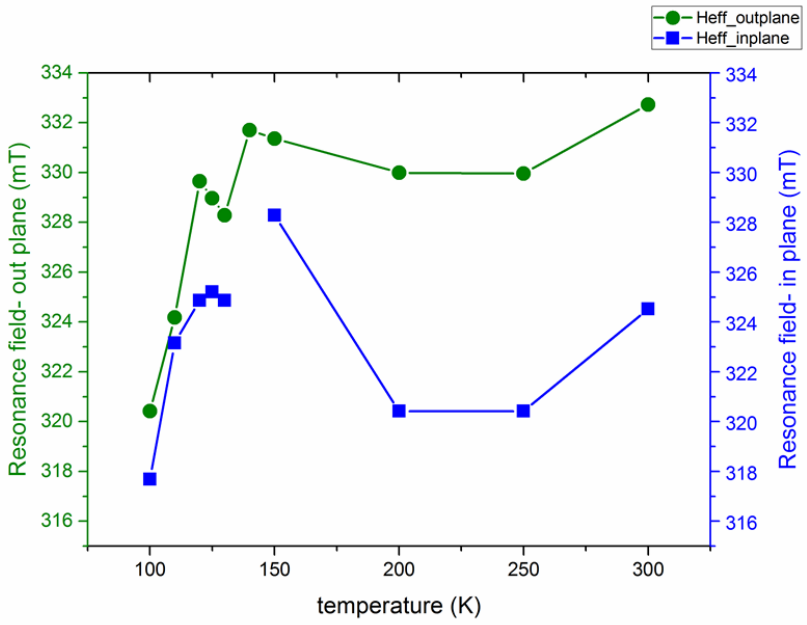

Figure 3.7 Resonance field of the temperature dependent FMR. The resonance field is extracted from the maximum of the absorption curve (integration of the FMR spectrum). Green line is for 0 degree and Blue for 90 degree measurement.

For further analysis, I derive the effective resonance field (H_{res}) values from the temperature dependent measurement (Figure 3.6). Here the qualitative behavior of out plane and in plane spectra is similar, but the out plane lines reach higher resonance than in plane ones. This

difference between out plane and in plane spectra was actually not expected, as the assumption was the random orientation of the scattered particles. TEM of these cells have shown that in some cells the particles have a bigger size than the average and thus can interact and form short chains. One explanation for the difference between the out plane and in plane spectra can be the small population of these short chains.

3.1.2 FMR Simulations

3.1.2.1 Simulation of WT FMR Spectra

Using the eq.2.8, as described in the methods section, the FMR spectrum for a single ellipsoid is calculated. For producing the spectra for the bulk sample, the different angles of chains (ellipsoids in the model) have to be considered. In a sample of randomly oriented cells, the chains can be aligned in every direction. This is represented by a superposition of random field directions, i.e., by a sum over all possible sets of (θ_H, φ_H) with a weight factor $sin\theta_H/4\pi$ accounting for the surface element and normalization (Charilaou, et al., 2011).

To quantify the magnetic anisotropies of the magnetosome chains, I simulate the FMR spectrum of randomly oriented cells, using the previously proposed ellipsoid model (Charilaou, et al., 2011, Kopp, et al., 2006).

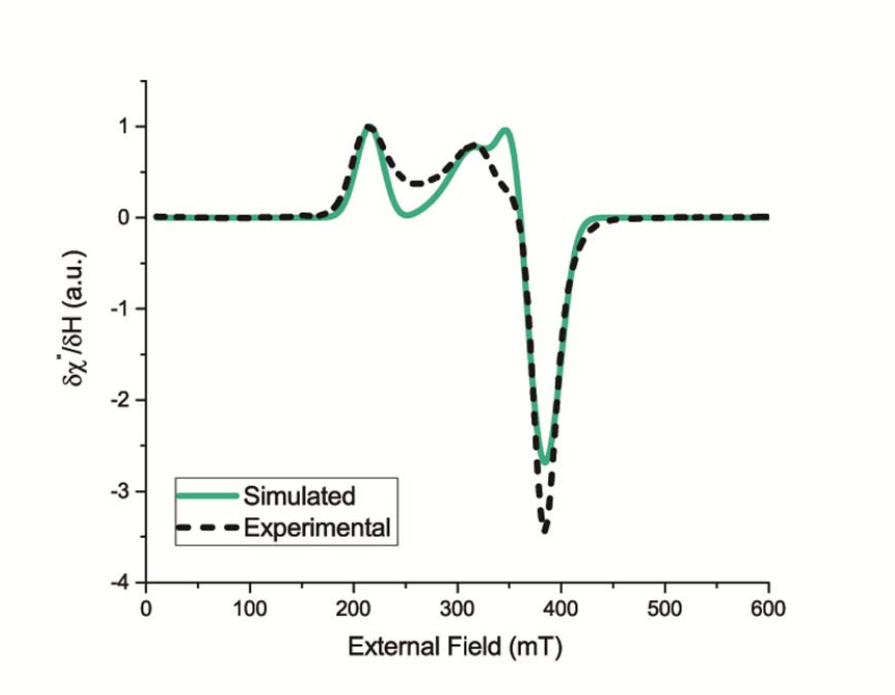

Figure 3.8 Comparison of simulated (green) and experimental (gray) FMR spectra for randomly oriented MSR-1 cells. The simulated spectrum corresponds to the best fit with parameters given in Table 1.

Figure 3.8, presents the simulated FMR spectrum for a sample of randomly aligned ellipsoids against the experimental results. The uniaxial anisotropy (H_{uni}), magnetocrystalline anisotropy (H_{cub}) of the modeled ellipsoids were the main fit parameters. From the best fit of the experimental spectrum, the intrinsic magnetic parameters of MSR-1 WT chains are derived, as shown in Table 3.1.

Table 3.1 Magnetic parameters of the samples obtained from fitting the simulated spectra with the experimental spectra. The error for these values is ±3.1 kA·m-1 for H_{uni} and ±1.6 kA·m-1 for H_{cub}. For *ΔmamJ* random, the simulated spectrum is independent of the H_{cub} due to the random alignment of magnetic easy axis of magnetite in the cluster.

	Wild type		**Δ*mamJ***	
	zero-field freezing (random)	in-field freezing (pre-aligned)	zero-field freezing (random)	in-field freezing (pre-aligned)
H_{uni} (kA·m-1)	70	70	0.8	40
H_{cub} (kA·m-1)	-20	-20	-	-20*

*This value was adapted from the WT and used for the simulation of Δ*mamJ* spectra as well..

The $H_{\mathrm{uni}} = 70\ kA.m^{-1}(880\ \mathrm{Oe})$, derived from the WT samples FMR, represents the average uniaxial field of the chains in the sample and corresponds to a demagnetizing factor $N_{\mathrm{eff}} = 0.1490$. These values are comparable to the ones reported in earlier works (Charilaou, et al., 2011).

The derived cubic magnetocrystalline anisotropy field for the chains (-20 $\mathrm{kA \cdot m^{-1}}$) corresponds to a magnetocrystalline constant of $K_1 = -1.16 \times 10^4\ J/m^3$. For stoichiometric bulk magnetite from magnetization curve analysis at the same temperature, a value of -8 $\mathrm{kA \cdot m^{-1}}$ is reported (Kaiskol and Honig, 1989). This difference is because the magnetocrystalline energy compared to the uniaxial energy is a second order term in the total energy of the chain. The crystalline constant of $K_1 = -1.16 \times 10^4\ J/m^3$ is closer to the value reported for bulk magnetite at room temperature (K_1= *-1.1x*$10^4\ J/m^3$). A similar shift in temperatures, where the magnetosomes resemble properties of bulk magnetite at a higher temperature, has also been reported for the Verwey transition, which occurs between 100 K and 110 K in magnetosomes (Fischer, et al., 2008). While for stoichiometric bulk magnetite the transition occurs at 123-125 K (Bickford, 1950, Pan, et al., 2005, Prozorov, et al., 2007).

The uniaxial anisotropy (H_{uni}) and magnetocrystalline anisotropy (H_{cub}) determined from the randomly oriented WT sample, are applied for the simulation of the FMR spectra of oriented cells as well, since the same sample was used and the chains are not deformed. Under theoretically ideal conditions, where all chains are perfectly aligned along the z-axis, a symmetric FMR spectrum is expected, since microwave absorption will be uniform in the ensemble. Figure 3.10a depicts the simulated spectra of such an ideally aligned sample, but this does not match the asymmetric experimental spectra. The simulation results show that the asymmetric spectrum shape arises when a portion of misalignment is defined into the model. Thus the asymmetry in the experimental spectra can be also caused by imperfections in the alignments in the sample. I model the orientation of the chains in this sample by applying a Fisher distribution function to describe a sample that were aligned in the z-direction with a range of deviation from the main direction (eq. 3.1). This distribution function has been used in paleomagnetic studies and was found to capture the angular dispersion of chain axes in fossil samples (Fisher, 1953). The Fisher distribution function in my framework is described as

$$F(\theta'_H, \varphi'_H; \kappa, \theta_H, \varphi_H) = \frac{\kappa}{4\,\pi \sinh(\kappa)}\, e^{\kappa \cos\delta}, \tag{3.1}$$

where the angle $\cos\delta$ is defined as:

$$\cos\delta = \cos\theta'_H \cos\theta_H + \sin\theta'_H \sin\theta_H \cos(\varphi'_H - \varphi_H). \tag{3.2}$$

The parameter κ is the precision parameter of the Fisher distribution. $\kappa = 0$ corresponds to a uniform distribution of the chain direction over the whole sphere (i.e., the case of the random samples) and for a perfect alignment κ approaches ∞ (Figure 3.9).

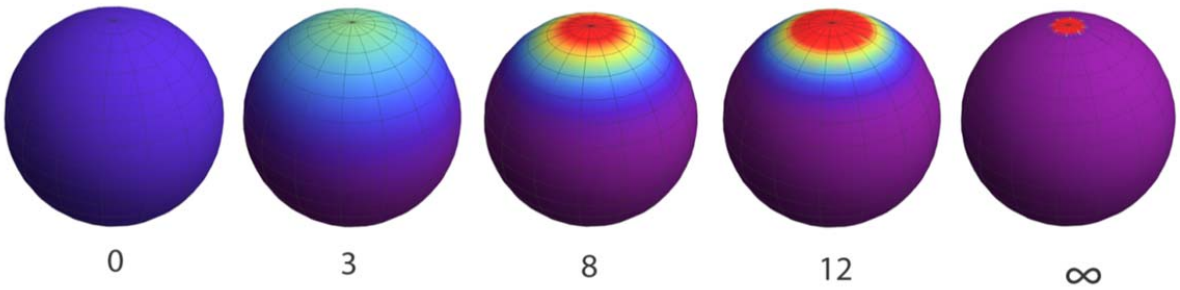

Figure 3.9 Spatial distribution of directions for different values of κ in 3D space. At small values of κ the possibility of finding the chains in any direction is equal. As κ increases, they become more aligned and the probability distribution at the field direction increases.

In the simulations to define an orientation distribution for the chains, every chain is assumed to align perfectly with the magnetic field and a distribution of magnetic field directions is defined, instead. The distribution of field directions is defined as a set of angles noted as (θ'_H, φ'_H). All these fields have a Fisher distribution centered around the main direction, which is the true field direction of the FMR in the laboratory frame (θ_H, φ_H).

The Fisher distribution represents the circle distance between (θ_H, φ_H) and (θ'_H, φ'_H) on the unit sphere. The distribution is assumed to be azimuthally symmetric, and the normalization is such that the integral over the unit surface is unity,

$$\int_0^{2\pi} d\varphi'_H \int_0^{\pi} \sin\theta'_H \, d\theta'_H \, F(\theta'_H, \varphi'_H; \kappa, \theta_H, \varphi_H) = 1. \qquad (3.3)$$

With the definitions above, the resulting spectrum of a bulk sample that is oriented along the z-axis with precision parameter κ while being exposed to an external field in the direction (θ_H, φ_H) has the form:

$$S_{tot}(\theta_H, \varphi_H) = \sum_{\theta'_H, \varphi'_H} F(\theta'_H, \varphi'_H; \kappa, \theta_H, \varphi_H) * S(\theta'_H, \varphi'_H) \sin\theta'_H. \qquad (3.4)$$

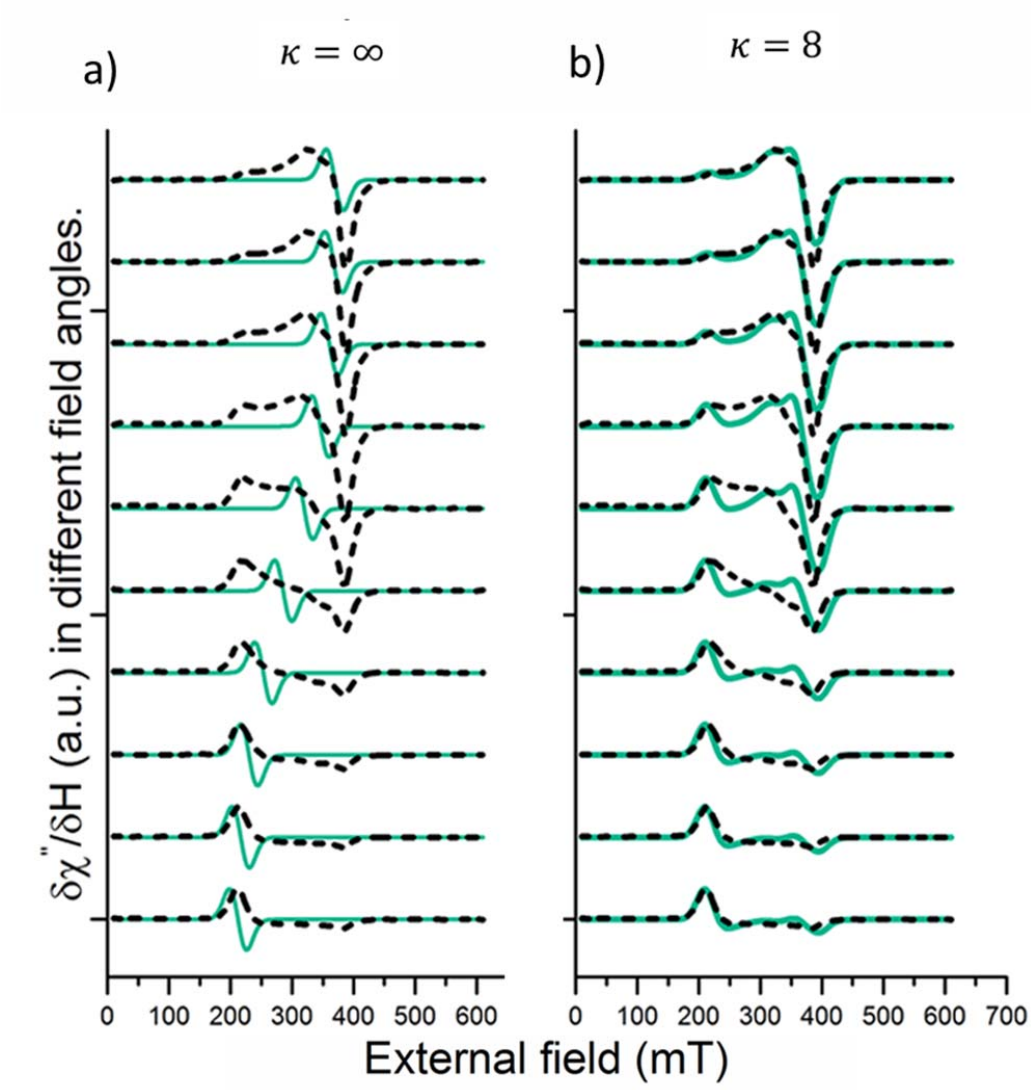

Figure 3.10 Comparison of simulated (green) and experimental (black) FMR spectra for oriented MSR-1 cells. The simulated spectra is for a modeled sample with Fisher distribution. a) When $\kappa = \infty$ there is no distribution thus it is the case of a perfectly aligned sample. b) $\kappa = 8$ is an oriented sample with a specific fisher distribution and this assumption improves the fit.

I simulated the FMR spectra of oriented cells using κ as a fit parameter to find the best match between the simulated and experimental spectra. Decreasing κ from high values (perfect alignment) toward values below 10, increases the width and asymmetry of the calculated FMR spectra, which is more similar to the experimental spectra. Thus, κ is used as a fit parameter to

find the best match for the spectral features. From the chi-square tests, the best fit is obtained at $\kappa = 8$. Figure 3.10 b presents the simulated *vs.* experimental spectra. The asymmetry of the spectra and the line broadening match the experimental spectra. The changes in various angles are also well produced, in comparison with the perfect aligned ($\kappa = \infty$) case.

3.1.2.2 Simulations of Δ*mamJ* FMR *S*pectra

I simulated and fitted the spectrum for randomly oriented Δ*mamJ* cells with the same procedure as for WT cells. The fit parameters values are shown in Table 1. The small uniaxial field ($H_{\mathrm{uni}} = 0.8$ kA m^{-1} or 10 Oe, $N_{\mathrm{eff}} = 0.001 \cong 0$) is indicative of a more isotropic ellipsoid close to a spherical shape (aspect ratio $\cong 1$) for the magnetosome arrangement, in agreement with the TEM image (Figure 3.2 c). The value of the magnetocrystalline anisotropy (H_{cub} or K_1) in the simulations of this sample did not affect the results. Therefore, this parameter is not determined by fitting the Δ*mamJ* spectrum. The orientation of the magnetocrystalline easy axis of magnetosomes in the cluster can be the cause since the magnetosomes can orient randomly with no uniform direction. Thus, a global magnetocrystalline order is not detectable. It should be noted, that the Δ*mamJ* spectra resemble spectra for wild type cells at temperatures below the Verwey transitions (Gehring and Charilaou, 2011), where the directions of the easy axes of magnetization are randomized by that transition, while in this case, they are randomized by the random orientation of particles in the clusters.

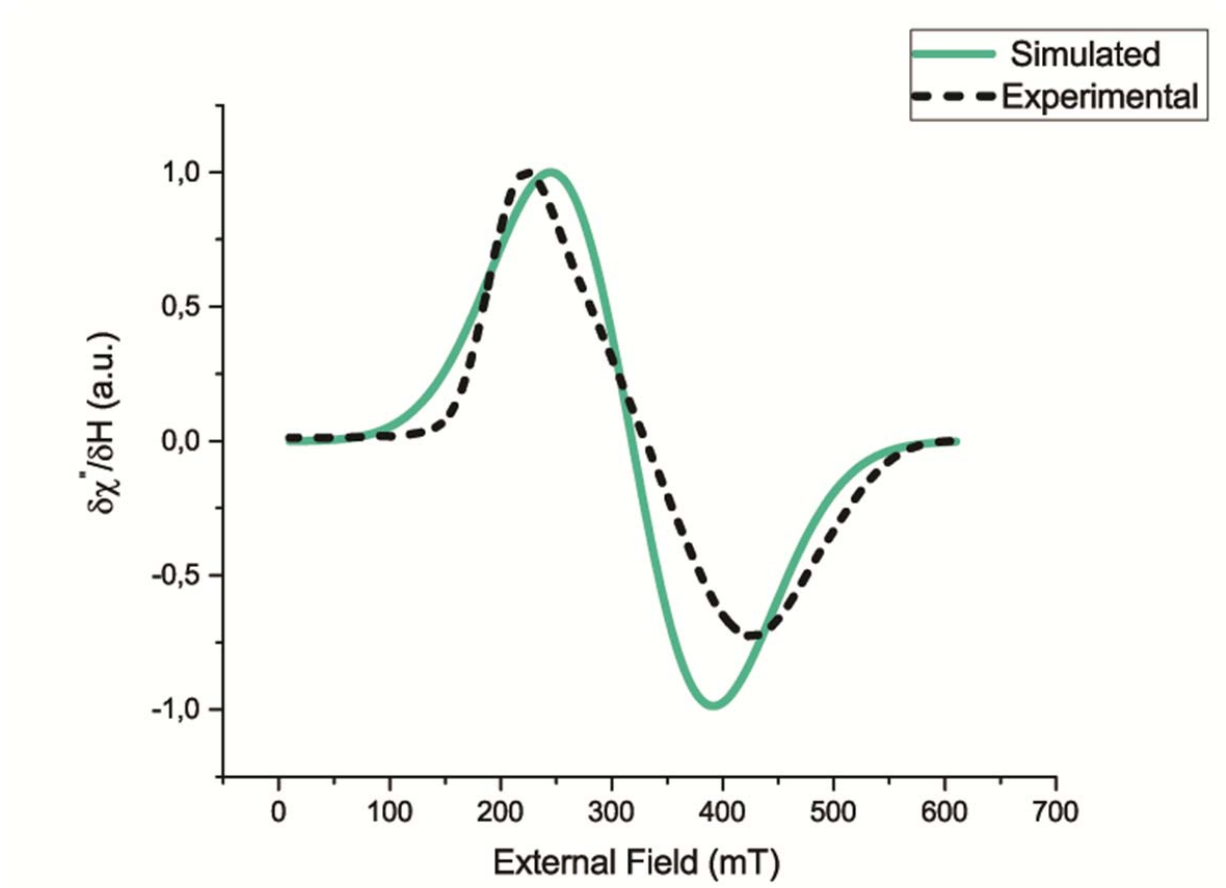

Figure 3.11 Simulated FMR spectrum of *ΔmamJ's* magnetosome cluster (green line). The gray line represents the experimental spectrum. The *ΔmamJ* cells were with no alignment during the measurement.

Unlike the magnetosomes in WT, which are fixed in their positions by MamJ proteins, the magnetosomes in Δ*mamJ* cells are free, and thus can rearrange in an external magnetic field (Körnig, et al., 2014, Scheffel, et al., 2006). This rearrangement is seen in the TEM images of samples frozen in the presence of a magnetic field (the "aligned" samples), where clusters are elongated in the direction of the field consisting of parallel short chains (Figure 3.2 d). The corresponding FMR spectra (Figure 3.12) for these samples exhibit an angular dependence, but are qualitatively different from the aligned WT spectra. The ellipsoid model does not accurately capture the interactions between the magnetosomes in the random clusters, but can be used to

estimate the uniaxial anisotropy. Matching the spectra results in a uniaxial anisotropy field of $H_{\mathrm{uni}} = 40\ \mathrm{kA/m}\ (500\ \mathrm{Oe})$, which corresponds to an ellipsoid with an aspect ratio of 1.30, shorter than the wildtype chains, but more elongated than the spherical Δ*mamJ* clusters from the randomly oriented samples. Moreover, the initial magnetic field applied before freezing could have oriented the magnetic easy axis of the magnetosomes parallel to each other. Thus, for the simulations, the magnetocrystalline anisotropy of this sample is considered to be similar to that of the WT sample. In the magnetosome cluster of Δ*mamJ*, each magnetosome is surrounded by more neighbor particles compared to the linear chain structure. This causes the possibility of two adjacent particles having a repulsive dipole interaction and hence reducing the absolute value of the total magnetostatic energy. Whereas in the case of linear chains, all the easy axes are aligned in parallel, and the dipole interaction is in favor of increasing the absolute value of this energy.

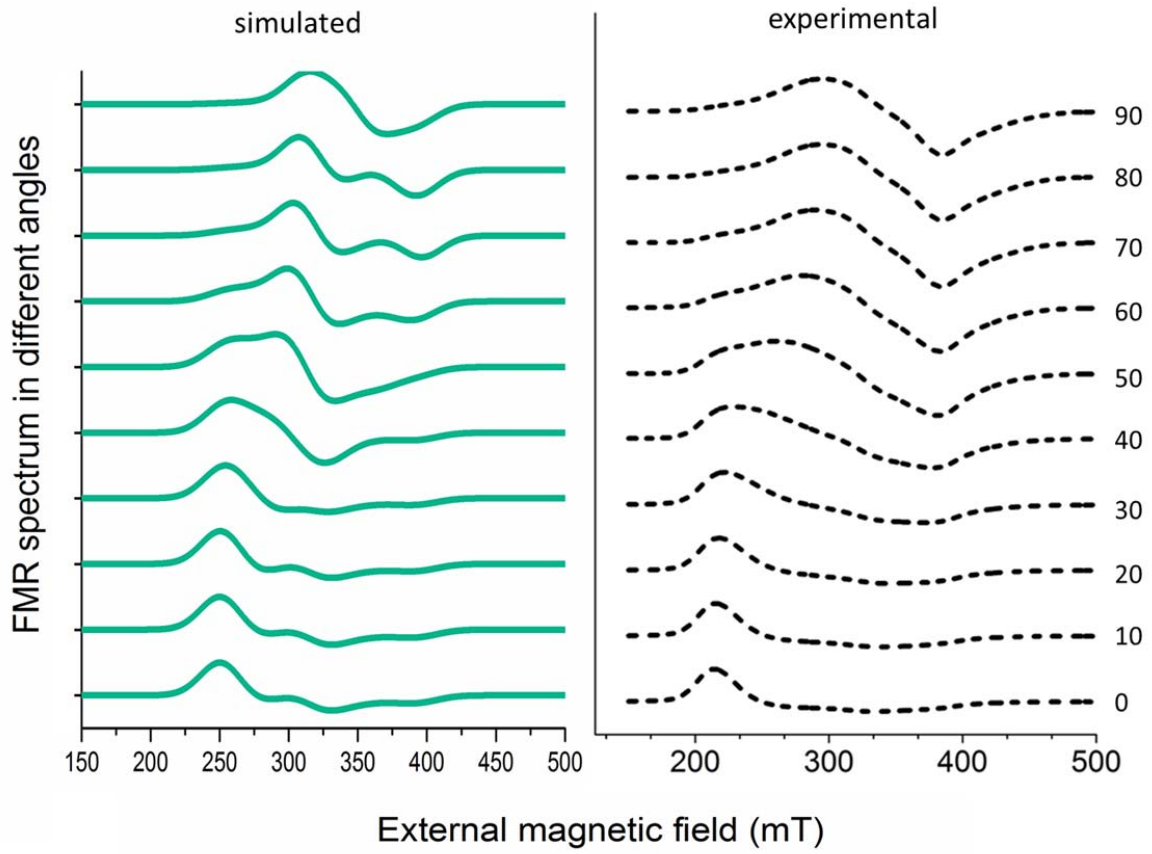

Figure 3.12 FMR spectra for ΔmamJ cells oriented in the magnetic field at different angles (from 0 to 90 degrees). The simulated spectra are calculated for H_{uni}=500 Oe .

Thus, in the cluster, the magnetostatic energy is lower, and on average the resonance conditions are fulfilled in lower fields. In the linear chains higher fields are required, especially when the external field is perpendicular to the chains. For a more explicit analysis on the magnetocrystalline anisotropy and easy axis directions, a model with inter-particle dipole interactions is more appropriate than the ellipsoid model.

3.1.2.3 Δ*F3* Scattered Particles Spectra Analysis

For simulation of this spectra, the uniaxial anisotropy is assumed to be zero or really small. This is concluded from the calculated shape factor of these particles which is ~1. The linewidth is the fit parameter and the spectra are calculated for different values of magnetocrystalline anisotropy fields ($H_K = K_1/M_s$).

Figure 3.13 shows the results of this simulation for a population of randomly oriented spherical particles with different cubic crystalline anisotropy. The plots are calculated from the ellipsoid model with H_{uni}=0, a line width of 14 mT and a changing magnetocrystalline constant K_1. The magnetocrystalline anisotropy field of the simulation, start from $H_{cub} = -20\ kA/m$, increases to zero and continues in positive values. Figure 3.13 presents the simulated FMR spectra with changing H_{cub}values. The spectrum at $-20\ kA/m$ is broader at the negative peak, with a small shoulder at field positions ~380 mT. This shoulder vanishes and the spectra gets almost isotropic close to $H_{cub} = 0$. As H_{cub} increases in positive values another shoulder appears at the positive peak around 300 mT.

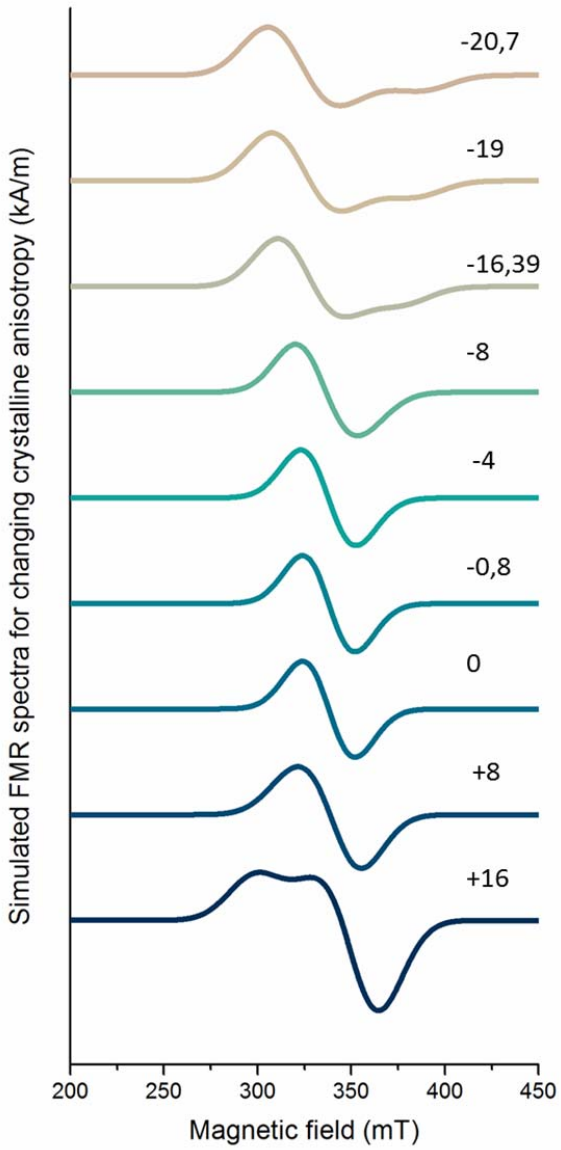

Figure 3.13 Simulation of FMR spectra for different magnetocrystalline anisotropies of scattered particles. The positive values are correlated to lower temperatures and the negative is as the temperature gets close to room temperature. The spectrum at -20.7 kA/m has a small shoulder around the 370 mT negative peak, and this shoulder vanishes as the magnetocrystalline approaches zero, which is the isotropic point. At +16 kA/m a small shoulder appears around the 300 mT peak.

The values for K_1 are taken from the work of Bickford (Bickford, 1950), where the anisotropy constant of magnetite is measured in different temperatures. Figure 3.14. depicts the correlation of the used H_{cub}, with temperature. The anisotropy constant decreases by increasing the

temperature for positive values to negative values by passing through the isotropic point and Verwey transition.

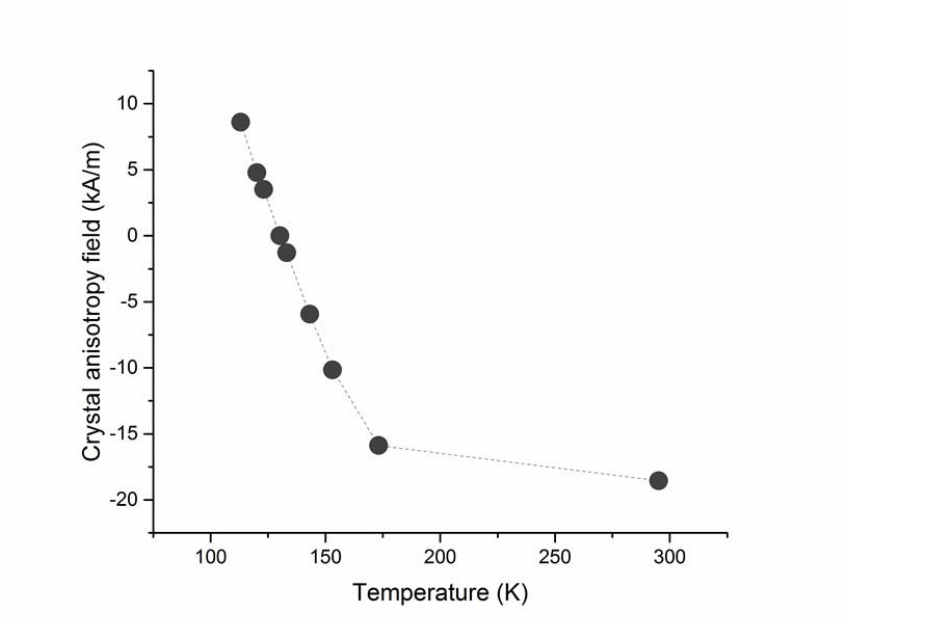

Figure 3.14 Dependence of magnetocrystalline anisotropy field on temperature. The values are adapted from (Bickford, 1950).

The Simulated spectra at different H_{cub} values are compared with the experimental spectra measured at various temperatures. The simulated spectrum at $-20{,}7$ and 16 kA/m can be correlated with the FMR measurement at 300 K and 100 K respectively. Figure 3.15 presents the results of simulated spectra and the correspondence experimental spectra. Figure 3.15a shows that all the spectrum features, including the zero point (effective resonance field), peak positions, and line width, are matching in both field position and intensity. Thus, the magnetosomes of this mutant can be considered to have a magnetocrystalline constant of $K_1 = -1.2x10^4\ J/m^3$, which is actually comparable to the value we obtained for WT magnetosomes.

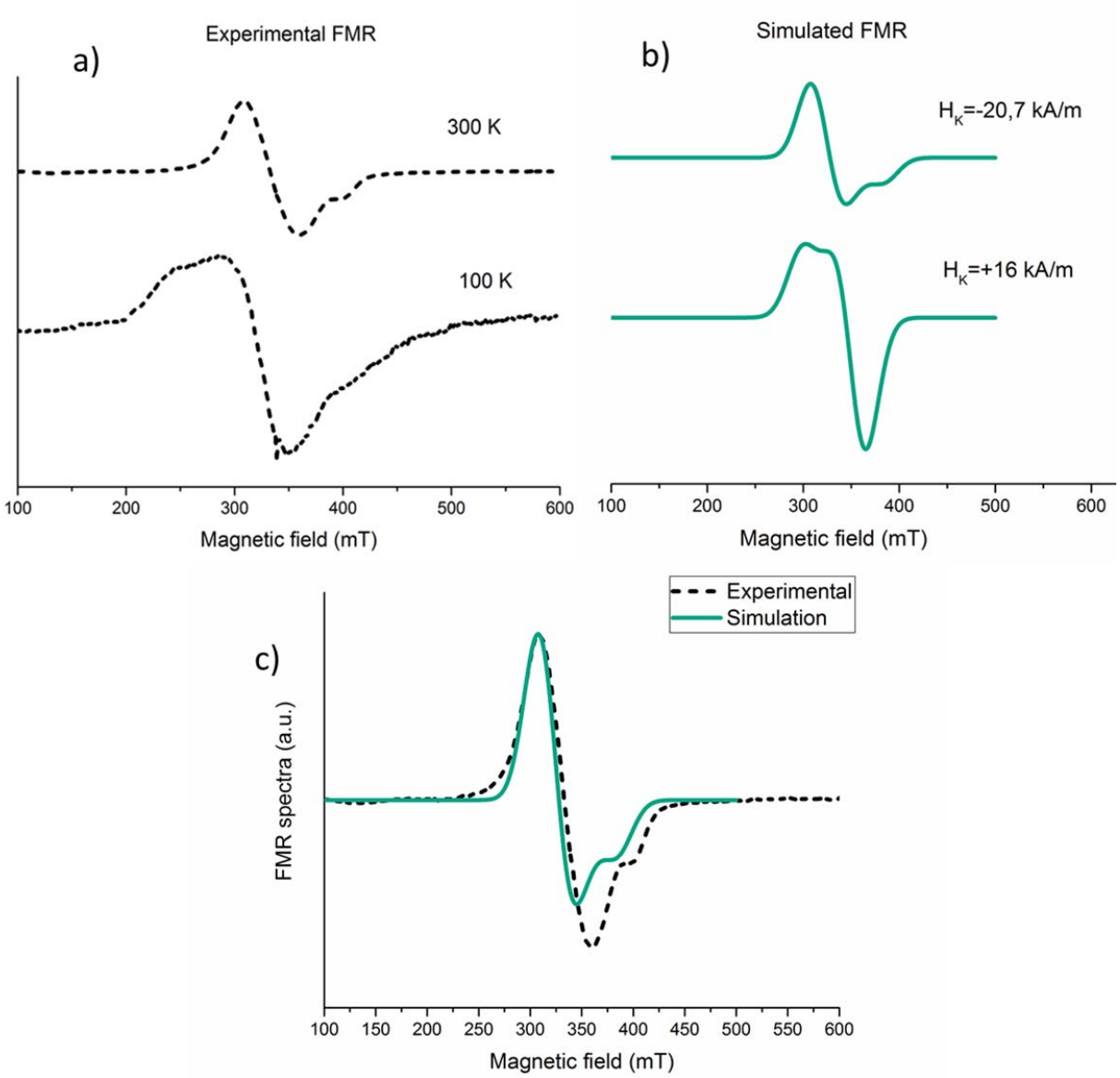

Figure 3.15 Simulated FMR spectra for scattered particles *vs.* the experimental in plane spectrum. a) Experimental spectra for different temperatures. b) The corresponding simulated spectra. c) The good fit of the simulated spectra at $H_K = -20{,}7\ kA/m$ with experimental spectra at 300K.

The particles produced by Δ*F3* mutant, are an excellent opportunity for studying the magnetocrystalline anisotropy of the magnetosomes. In these cells, the particles are scattered over the cell, and are distant enough for not having any dipole interaction with the other

magnetosomes in the cell. Thus the effect of the magnetocrystalline anisotropy is not affected by the stronger dipole interactions.

3.1.3 Discussions

Figure 3.16 gives an overview of all the FMR spectra of bulk MSR-1 samples presented in the previous sections. FMR is a ferromagnetic spectroscopy and it is only sensitive to the magnetic materials, which are the magnetosomes. The magnetosome assemblies or orientations are changing in each set of FMR measurements, and the spectra line shape and its main features, such as peak positions, peak intensities, and zero crossing point, are strongly influenced by this. This influence can be categorized to be mainly from two aspects:

- The alignment of the magnetosomes in the samples.
- The anisotropy of the magnetosomes, which can be both uniaxial anisotropy and magnetocrystalline anisotropy.

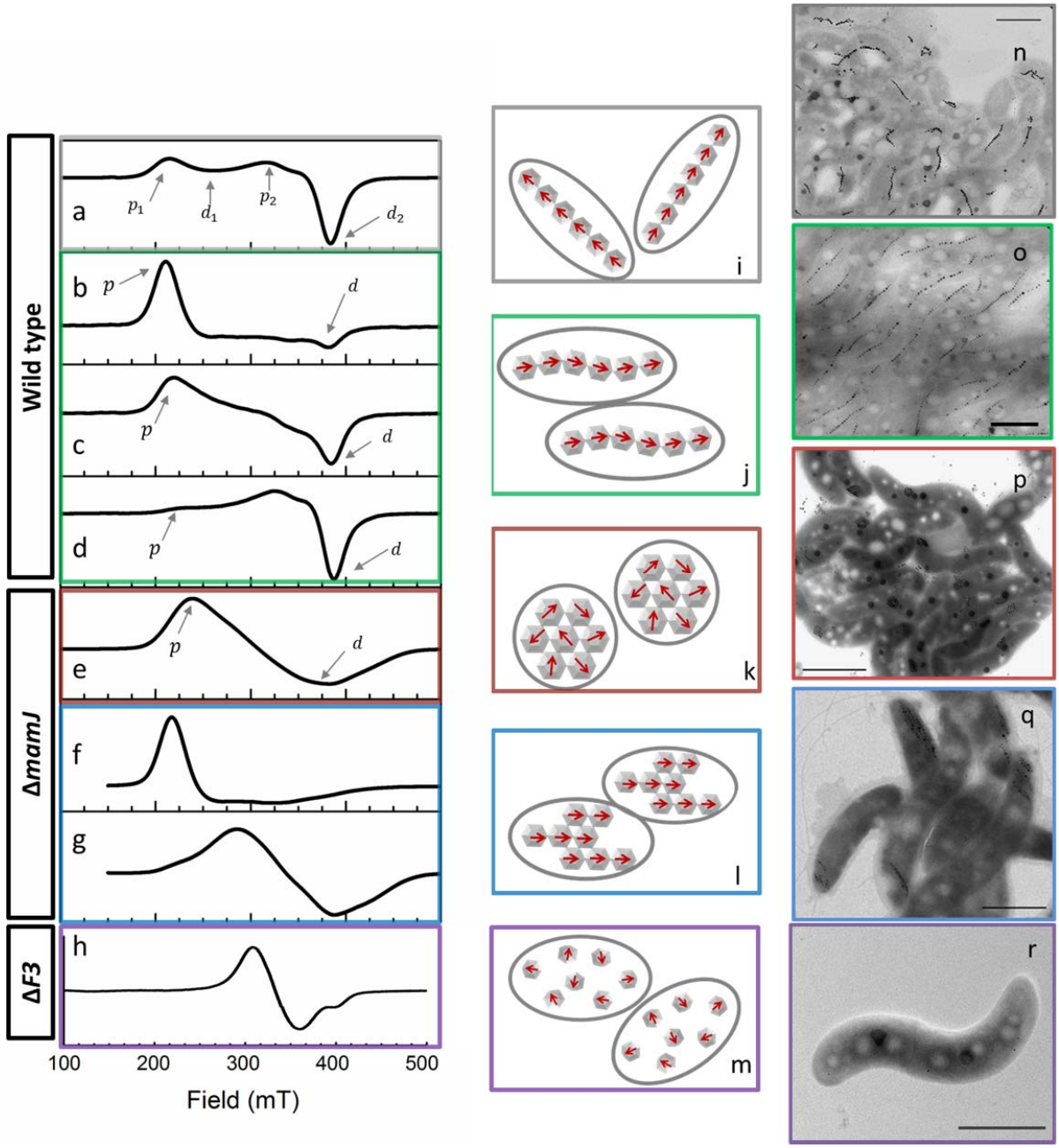

Figure 3.16 FMR spectra of different MSR-1 samples performed at 150K. FMR spectra of different MSR-1 samples performed at 150K. All the spectra are normalized to their maximum. a) Spectrum for randomly oriented wild type cells. b-d) Spectra for oriented WT samples with the magnetic field at 0, 45 and 90 degrees relative to the chain orientation. e) Spectrum for the mutant Δ*mamJ*. The symmetric spectrum reflects the isotropic structure of the magnetosome clusters. f,g) Spectra of Δ*mamJ* samples that were oriented with a magnetic field. The field during measurement is at angles 0 and 90° with the axis of orientation. h) spectrum for randomly oriented Δ*F3* cells. i-m) Schematic representation of the magnetosome chains or clusters in these samples and their orientation. n) TEM image of MSR-1 randomly oriented cells. o) TEM image of MSR-1 WT cells, dried in the presence of an external magnetic field. p) TEM images of MSR-1 ΔmamJ mutant, normally dried cells. q) ΔmamJ cells dried in the presence of a magnetic field. r) Δ*F3* with small particles scattered inside the whole cell. Scale bars represent 1 µm.

3.1.3.1 The Effect of Alignment Changes on FMR Spectra

The angular dependent FMR measurements reveal alignment properties of the sample. This can be inferred from both line characteristics in each angle, as well as from the line changes in a rotational measurement. For the randomly oriented WT sample, the angular independency of the measurement is an evidence of uniform distribution of chains. But this random distribution is also the main reason for the broad nonsymmetrical line shape (Figure 3.1 a). With the aligned samples although theoretically a symmetric line shape is expected (Figure 3.10 a), the experimental FMR has an asymmetric line shape. The discrepancy likely reflects a finite angular distribution of chain orientations about the pre-alignment direction. There are at least two non-mutually exclusive reasons why this could be the case: The alignment of the chains could be imperfect and limited by the cell volume and geometry, especially in case of high concentration of cells in sample. Moreover, magnetosome chains in the cells are not all perfectly linear, and bent chain segments could be considered as (short) chains that are not perfectly aligned with the field. Both interpretations are supported by experimental evidence (Körnig, et al., 2014, Li, et al., 2013). Including the possibility of imperfect alignment into the model, resulted in improved agreement with the experimental spectra (Figure 3.10 b).

Table 3.2 Cumulative probability distribution of chain orientation around the average direction for different κ values.

Angle (degree)	κ =3	κ=8	κ =12
0	0	0	0
5	9,353127	15,38192	18,87933
10	20,8389	33,72433	40,87333
15	31,86526	50,18232	59,57657
20	42,21705	64,0998	74,1327
25	51,72565	75,20565	84,5198
30	60,27661	83,58251	91,33292
35	67,81117	89,56751	95,45348
40	74,3224	93,62814	97,75992
45	79,84709	96,25192	98,9599
50	84,45531	97,87183	99,54303
55	88,23916	98,83091	99,80913
60	91,30226	99,37757	99,92383
65	93,7508	99,67883	99,97082
70	95,68683	99,84005	99,98925
75	97,2037	99,92425	99,99621
80	98,38353	99,96736	99,99876
85	99,29628	99,98912	99,99968
90	100	100	100

With this theory, I extended the ellipsoid model by introducing a distribution of orientations, characterized by the Fisher distribution function (Fisher, 1953). In Fisher distribution, the degree of alignment is characterized by the parameter κ and the degree of alignment of chains can be quantitatively assessed in the simulations. For the case of oriented MSR-1 WT cells, the best fit is obtained for κ =8. This value defines a distribution of the angle of alignment with standard deviation 25°. This can be explained as 75% of the chains are oriented within this angle around the z axis, 90% are within 35° (Table 3.2). The degree of alignment found here is comparable to what was found in a recent study by Li et. al. (Li, et al., 2013). Based on SEM analysis of the related strain AMB-1 cells, which also has a linear magnetosomes chain, they showed that chains were imperfectly aligned by the external magnetic field with a standard deviation of 21 ° of the chain angles relative to the field direction.

The simulation also shows that the distribution of chain orientations in the sample can cause a broadening of the resonance spectrum. This broadening can be explained by the fact that the measured spectrum is a superposition of the signals of individual chains, which are under different angles with the field and experience resonance at different field strengths. In other words, the angle-resolved spectra can be seen as a decomposition of the spectrum of randomly oriented cells, which is given by a superposition of all possible angles, similar to what has been reported for oriented cells of RS-1 and MSR-1 before (Chariaou, et al., 2015, Charilaou, et al., 2014). The asymmetric shape of the spectrum can then be explained in this way, because most chains are subject to a projection of the field and thus a reduced field strength and a correspondingly larger resonance field. The remaining differences between the simulated and the experimental spectra may be due to the diversity of magnetic uniaxial energies in the sample that arise from different chain lengths and arrangements (e.g. broken or bent chains). This can be included in the model further by introducing e.g. a fraction of random background in the simulation (Figure 3.17) or calculating the different dipole interactions in various magnetosome arrangements.

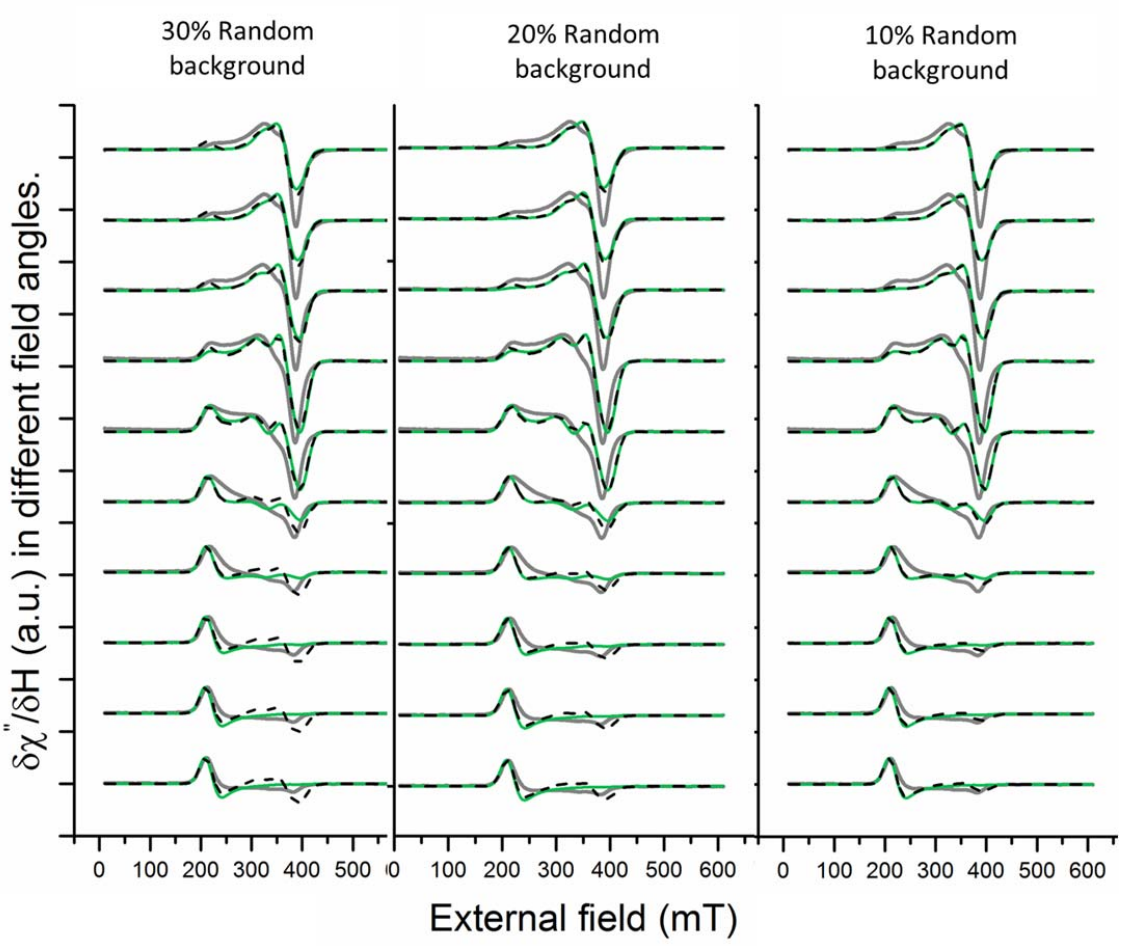

Figure 3.17 Simulated FMR spectra of a sample with a fraction of random background in addition to the orientation distribution (Black dashed lines). The green line is the case with 100% orientation distribution and the gray line experimental data.

3.1.3.2 The Effect of Anisotropy Changes on FMR Spectra

The $H_{\text{uni}} = 70\ kA.m^{-1}$, derived for WT samples, represents the average uniaxial field of the chains in the sample and corresponds to a demagnetizing factor $N_{\text{eff}} = 0.1490$. This demagnetizing factor represents an ellipsoid with an aspect ratio of 1.56 (Osborn, 1945), which might be interpreted as reflecting a rather short chain. One should however take into account that the ellipsoid is only an approximation for the chain's structure and its uniaxial energy, which is

due to the inter-particle interactions as well. Moreover, not all chains are perfectly linear, and this can cause the average uniaxial anisotropy of the bulk sample to be less than the value expected for a chain of 20 particles. The small uniaxial field of ($H_{\mathrm{uni}} = 0.8\ \mathrm{kA\ m^{-1}}$) of randomly aligned Δ*mamJ* indicates isotropic ellipsoids close to a spherical shape (aspect ratio $\cong 1$) for the magnetosome arrangement. This is in coherent with the magnetosome forms at the TEM images. By comparing the FMR spectra shapes of these two different samples, it is concluded that the symmetry of the line shape is a direct measure for the isotropy of the sample. The Δ*mamJ* cells with the spherical arrangement of magnetosomes can be referred as an extreme isotropic structure, while the WT sample is a anisotropic structure with asymmetric FMR spectra.

Moreover, the spectra of oriented Δ*mamJ* cells are an intermediate case in between the spherical cluster and the chains, with uniaxial anisotropy field of $H_{\mathrm{uni}} = 40\ \mathrm{kA/m}$. The asymmetry of the spectra is higher in lower angles and at angles close to 90° gets more symmetric. Thus the uniaxial anisotropy can affect the extent of angular changes of the spectra. The effective resonance field can be a good reference to quantify the angular changes of the spectra.

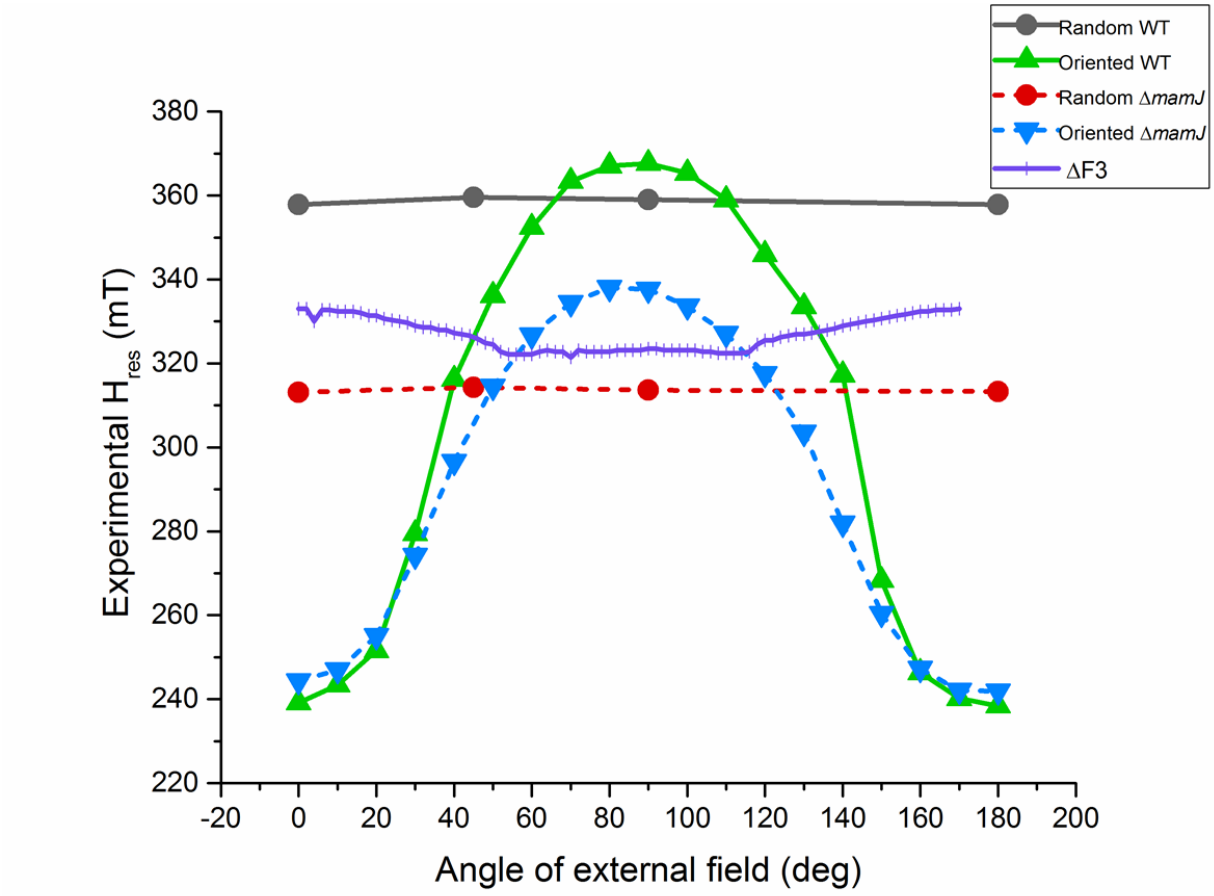

Figure 3.18 Effective resonance fields of all experiments extracted from the FMR spectra in Figure 3.16.

The FMR spectra are actually the first derivative of the microwave absorption by the sample, thus the zero crossing point of the spectrum is known as the maximum absorption point. The field position of this point is referred as the effective resonance field (H_{res}). This parameter can be used as a measure to observe the average absorption of a sample. The effective resonance fields of the different WT and Δ*mamJ* spectra in changing angles are depicted in Figure 3.18. As it has been discussed before, the randomly aligned samples are angular independent and thus appear in the plot as a constant line. Still, the line for WT is higher than for Δ*mamJ* and this applies to the

oriented samples as well. Both oriented WT and Δ*mamJ* have an two-fold symmetric angular dependent measurement, with WT having a higher field range starting from around 250 mT to 360 mT. This can be correlated to the higher uniaxial anisotropy of the chains, and thus a proof that the uniaxial anisotropy can affect the line shape in a randomly oriented sample and the effective resonance field range in the angular measurement of an oriented sample.

Table 3.3 summarizes the effective resonance field (H_{res}) of for oriented WT and Δ*mamJ* from Figure 3.18, as well as for Δ*F3* from Figure 3.5.

Table 3.3 Resonance field for different strains.

	H_{res} (mT) min	**H_{res} (mT) max**	**ΔH_{res} (mT)**
Oriented WT cells	238	368	130
Oriented *ΔmamJ*	250	330	80
Δ*F3*	320	335	15

For Δ*F3* cells the range (ΔH_{res}) is less than 10% of WT cells. For the Δ*F3* cells this small angular dependency is not theoretically expected, since the particles are all randomly oriented in the cell. Comparison of ΔH_{res} of WT and Δ*mamJ* with the value for Δ*F3*, show a probability of small magnetosome chains formation in some of the Δ*F3* cells.

3.2 PEEM

3.2.1 XMCD Magnetic Measurement Results

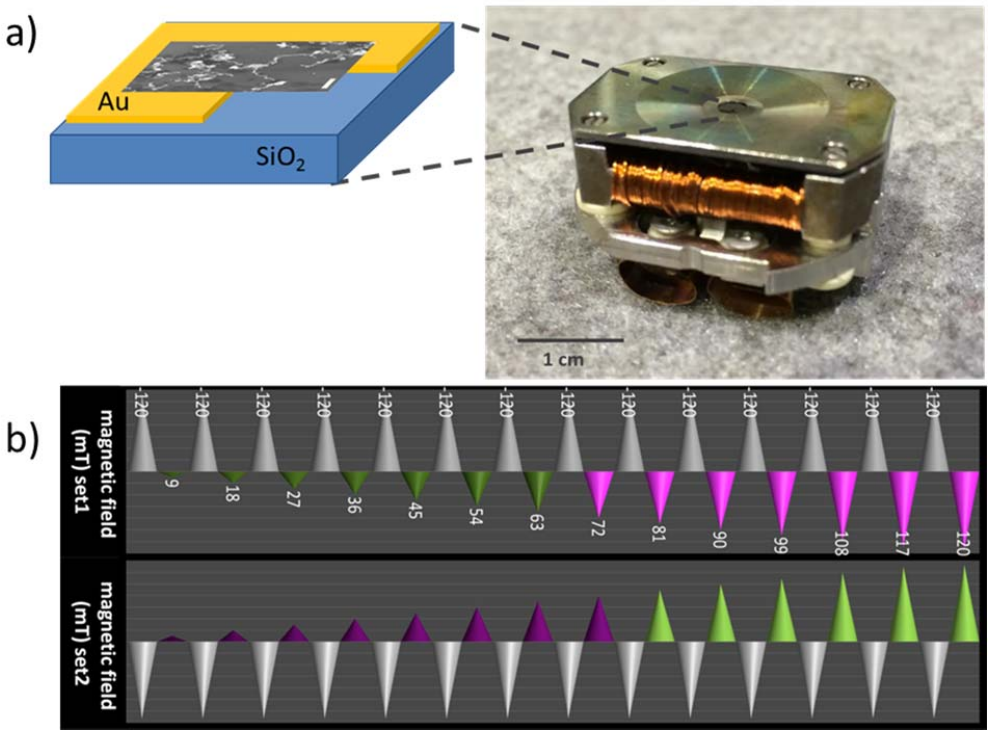

Figure 3.19 Sample holder for PEEM. a) Two coils on both sides of the holder produce the magnetic field that is applied on the sample during the measurement. b) A graphical view on the magnetic field profile. Each arrow in the image represents a magnetic field. The XMCD images are obtained after a sequence of -120mT saturating field (gray arrow) and the opposite reversing field (colored arrow). The imaging is performed after the reversing field is switched off, while the samples where in a remanence magnetization. Set1 and set2 are the same procedure in the counter direction. The black arrows indicate the field in which the direction of magnetization is flipped.

The XMCD experiment was designed to measure the remanent magnetization of the magnetosomes. Remanence is a measure for magnetization stability, which has been previously studied for both bulk and single magnetosome samples (Hanzlik, et al., 2002, Moskowitz, et al., 1988, Penninga, et al., 1995). The field profile for the experiment is depicted in Figure 3.19b.

Two sets of measurements were performed with a similar design but an opposite direction of the fields. Each XMCD image is obtained after the application of a sequence of a 120 mT saturating field, B_{sat}, followed by a reverse field, B_{rev}. B_{rev} is increased in each step (Figure 3.19b) and is applied to overcome the magnetization remanence of the sample after it is saturated with the 120 mT field. When B_{rev} is strong enough to overcome the remanence, the magnetization changes its direction with B_{rev}. In this way, the remanence of the chain is measured.

The results of the XMCD imaging in the changing field are the series of magnetization maps for the field of view (Figure 3.20). In these maps, the magnetization direction is color-coded to show the magnetic moments of the magnetosomes, parallel or antiparallel with the direction of the applied field, which is along the X-ray beam as well. In these maps, in the first set of images, as long as an area is color coded with green, it has a negative direction of magnetization and this indicates that it is still resisting the positively directed reversing magnetic field. The change of the color to magenta, represents the reversing of the magnetic moments to the positive direction with the field. In the second set the direction of the applied field, and thus the color codes are contrariwise.

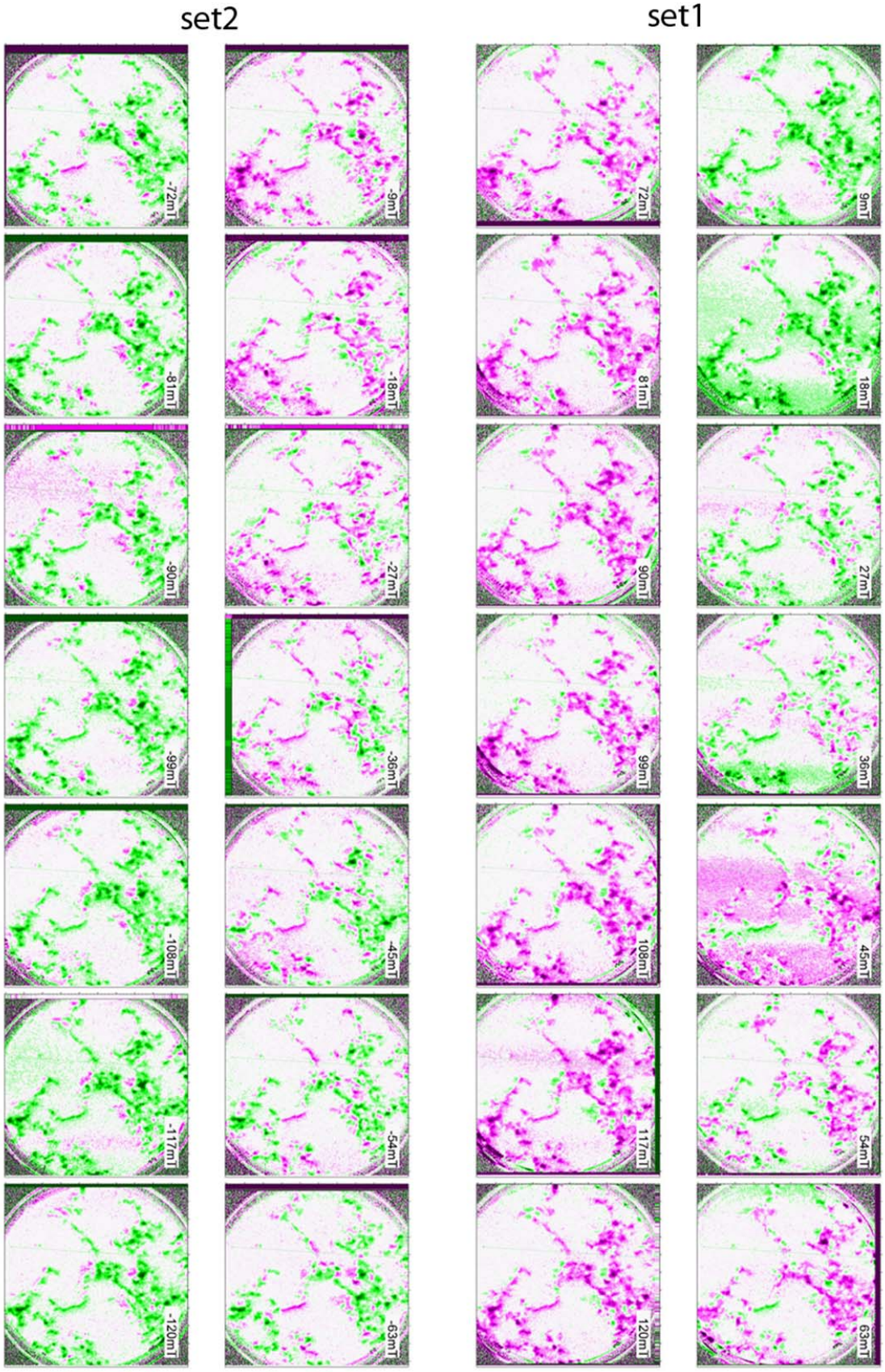

Figure 3.20 XMCD remanent maps after different applied magnetic fields.

I use these maps to analyze the remanence of each structure and to understand the effect of magnetosome arrangements on their magnetization stability. A qualitative review of the maps reveals differences between the magnetic stability of linear and clustered magnetosome structures. For instance in Figure 3.20, set 1, there is a linear structure that is the most stable structure and resists on changing its magnetization direction (remains green) up to the field of 72 mT. Also another example is the magnetosome aggregate in the middle, for which the magnetization direction is changing partially and not all in once.

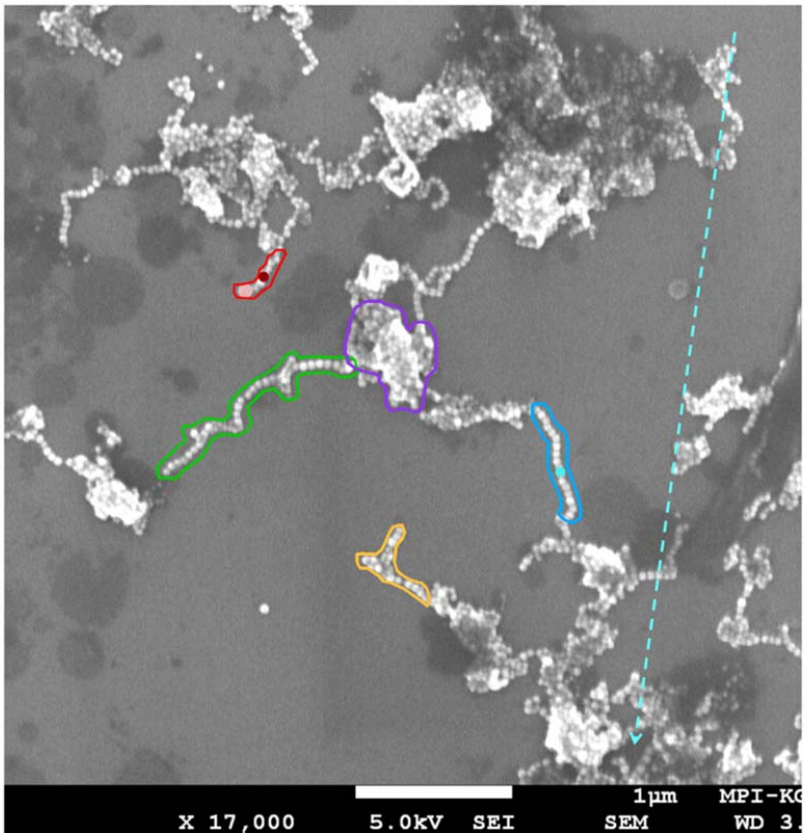

Figure 3.21 SEM image of the field of view. The regions of interest are color coded, and the blue arrow is showing the direction of the external field. This image is utilized for analyzing the magnetosome arrangements in each structure.

More definite information of the structures' morphology is drawn from the SEM image (Figure 3.21). Since the SEM image and the XMCD maps are coordinated, a region of interest can be selected based on its morphology at the SEM image, and its magnetic behavior in the XMCD maps be directly extracted. In the following, I will make a review on the extracted remanent curves of some of the structures.

The first interesting structure is the linear chain. This straight chain resembles that of intact cells. The magnetization of this structure is extracted from the series of XMCD maps and plotted as the remanent curve (Figure 3.22). The remanence has a significant stepwise change, after remaining constant in the first few field steps before 72mT. This indicates that the magnetization of the chain is resisting the reversing field (B_{rev}) and only switches when this field increases up to ~72mT. Owing to the spatial resolution of the acquired XMCD magnetic map, I can track how each of the magnetosomes in the chain are reacting to different strengths of B_{rev}.

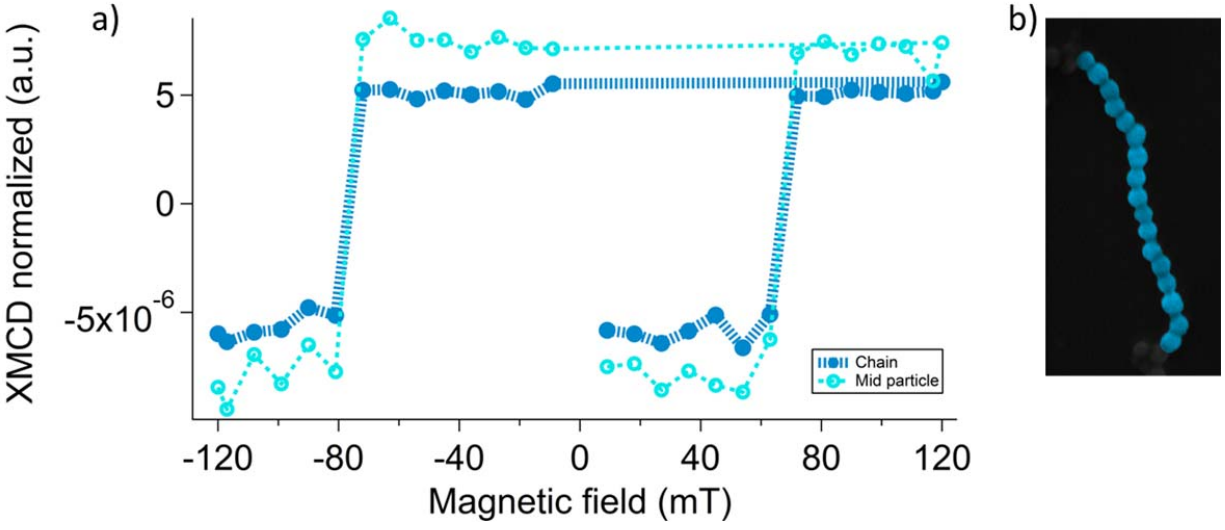

Figure 3.22 a) Remanence curve for linear chain extracted from the XMCD images. The positive x-axis of each curve is for the set 1 measurements and the negative x-axis side is for set 2. b) The SEM image of the linear chain.

Interestingly, all magnetosomes change their magnetization direction simultaneously in the entire chain. This causes the whole chain to behave as a single domain material, with a stable and homogenous magnetization. The remanence of a single magnetosome in the middle of chain can be extracted to depict the behavior of a magnetosome as an entity in comparison with the whole chain. The magnetization of this particle changes direction at the same B_{rev} as the whole chain, but it has a higher XMCD intensity and correspondingly a higher magnetization. This shows that the particle in the middle is more perfectly aligned along the chain, than the average magnetization of the whole chain. This is due to the interactions of this particle with the neighboring particles in the chain.

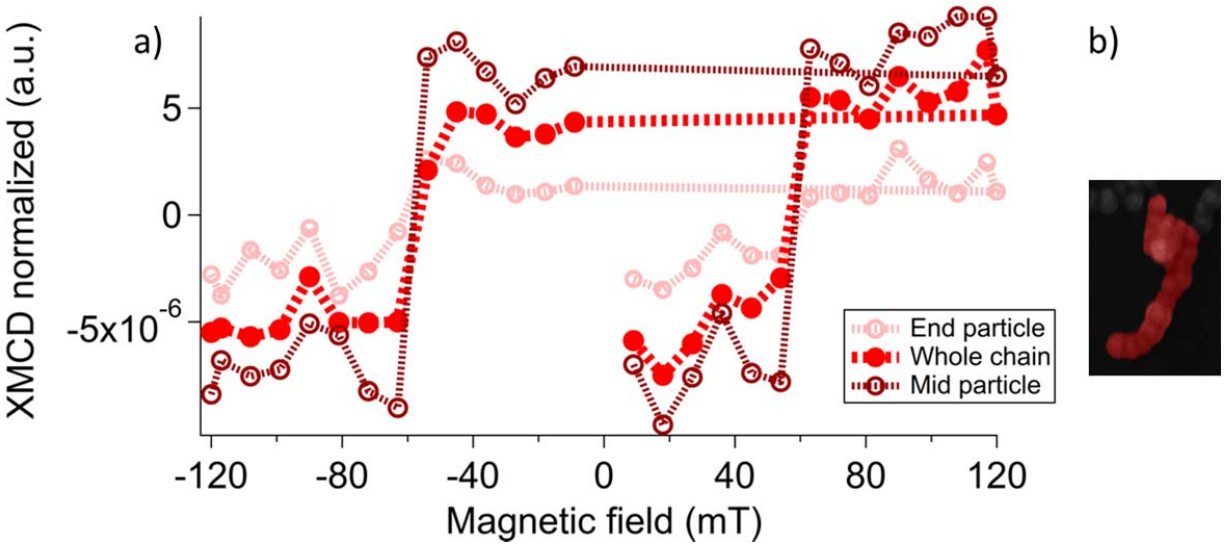

Figure 3.23 a) Remanence curve for linear chain with ending particle. b) The SEM image of the measured structure.

Another linear chain is located at the top of the area (marked with red). The corresponding remanent curve (Figure 3.23) demonstrates that this chain structure is also a single domain. In this plot the single magnetosome in the middle of the chain has a higher intensity as well. Moreover, in this structure a single magnetosome at the end of chain can be measured and

compared with a particle that is in the middle of the chain. The ending particle has a lower XMCD intensity, which can be the result of being less affected by dipole interactions of neighbor particles and more deviated from the chain line.

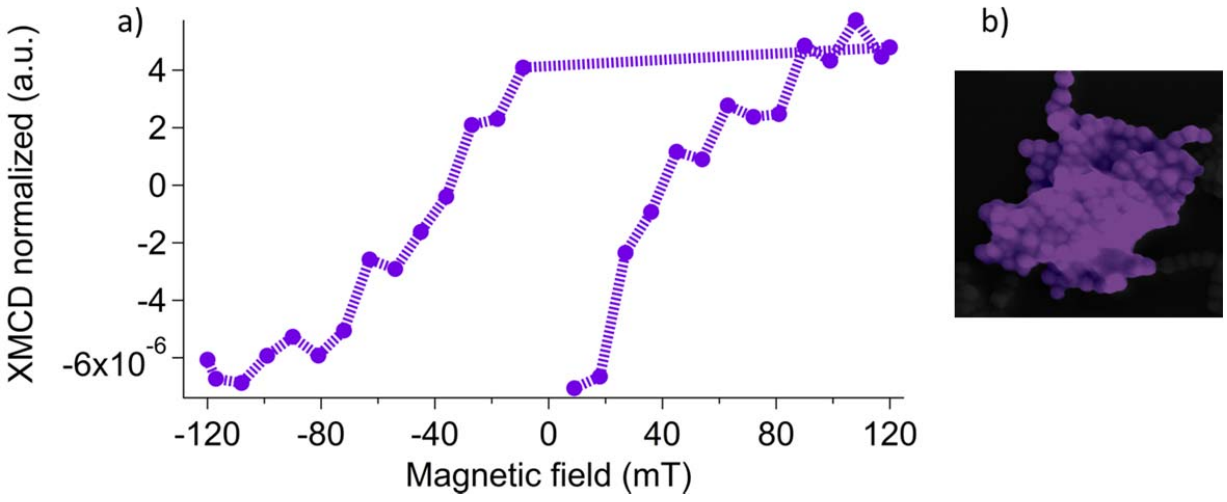

Figure 3.24 a) Remanence curve for magnetosome cluster. b) The SEM image of the cluster.

The cluster arrangement located at almost the center (marked in purple), is another remarkable structure, since it is an informative comparison with the linear chain and furthermore can be a reminiscence of the magnetosome structure found in the Δ*mamJ* mutant. As mentioned before, the XMCD magnetic images, map the partial changes of magnetization direction in this structure at low B_{rev}. This is also observed in the remanent curve of the cluster (Figure 3.24), which has a gradual change with the field steps from the lowest B_{rev}.

The magnetosome cluster in contrast to the linear chain is reacting more like a multi-domain structure with a low resistance to the reversing fields, although each magnetosome is a single-domain structure itself. This can be explained due to the random orientation of the magnetosomes' easy axis in the cluster (Ghaisari, et al., 2017), and the wide variety of possible dipole interaction between the particles.

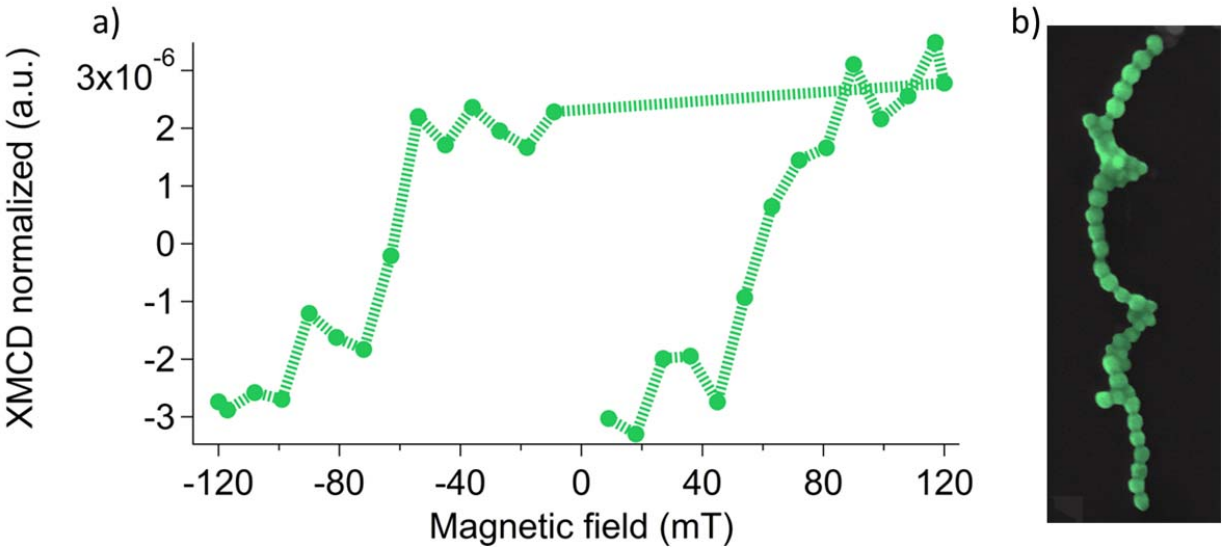

Figure 3.25 a)Remanence curve for segmented magnetosome chain. b) The SEM image of the segmented magnetosome chain

An intermediate configuration between the linear chain and cluster can be the segmented chain, sectioned by some nodes of particles. The remanence behavior of this chain (Figure 3.25) is also in-between those structures. The magnetization is not switching in one field step, instead the XMCD intensity of the chain changes gradually starting from B_{rev}~ 54mT. The magnetic maps illustrate how each section reacts to the reversing field, and that the linear sections have higher remanence and stability than the nodes.

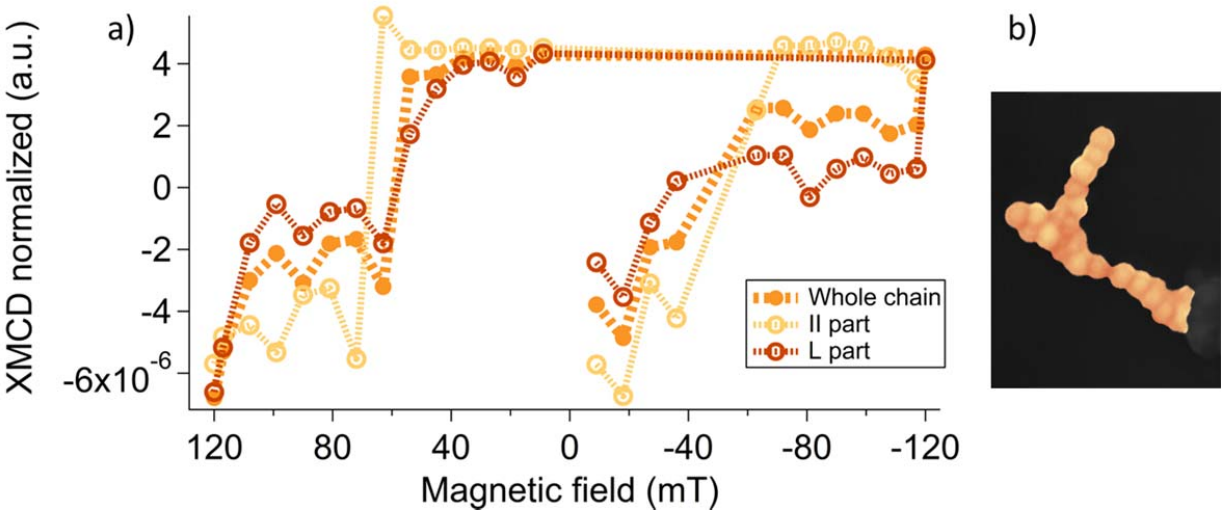

Figure 3.26 a) Remanence curve for cane like magnetosome configuration. b) The SEM image of the measured structure.

Figure 3.26, depicts the remanence of a cane like structure located at the lower part of measured area. The notable point of this structure is the almost right angled chain sections, which is a suitable structure to compare the effect of parallel *vs.* perpendicular magnetic field. The remanence magnetization for the perpendicular section starts with a specific negative value, and then it is almost zero even at the higher fields. The zero intensity is actually when the magnetization of this section is directed along its chain axis and thus perpendicular to the magnetic field and beam, thus there is no magnetization along the beam and the detected intensity is then almost zero. This occurs because B_{rev} is not strong enough to overcome the dipole interaction between the magnetosomes in this chain. For the parallel section, remanence curve is following the chain like pattern as before.

3.2.2 Simulation of the Energy Barriers

The simulations were performed in collaboration with Dr. Bahareh Kiani (Department Theory and Bio-Systems, Max Planck Institute of Colloids and Interfaces). The simulations are carried out by employing the model developed in Kiani *et al*. (Kiani, et al., 2015) for magnetosome chains to obtain the equilibrium orientations of the particle's magnetic moments, from Monte Carlo simulations. In this model, a magnetosome chain is described as a linear chain of N spherical magnetosome particles connected to the rigid filament. The full energy of the system includes the dipole-dipole interactions energy E_{dd}, the external magnetic field-dipole interaction energy E_B and the magnetocrystalline anisotropy energy term $E_{crystal}$.

$$\begin{aligned} E &= E_{dd} + E_B + E_{crystal} \\ &= -\frac{\mu_0}{4\pi}\sum_{i=1,j>i}^{N}\frac{1}{r_{ij}^3}\left(\frac{3(\boldsymbol{m}_i\cdot\boldsymbol{r}_{ij})(\boldsymbol{m}_j\cdot\boldsymbol{r}_{ij})}{r_{ij}^2}-(\boldsymbol{m}_i\cdot\boldsymbol{m}_j)\right)-\sum_{i=1}^{N}(\boldsymbol{m}_i\cdot\boldsymbol{B}) \\ &+ K_1\left(\frac{1}{4}\sin^4(\theta)+\frac{1}{4}\cos^4(\theta)+\frac{\sqrt{2}}{3}\sin^3(\theta)\cos(\theta)\cos(3\varphi)\right) \end{aligned} \qquad (3.4)$$

$\mu_0 = 4\pi \times 10^7 \mathrm{NA}^{-2}$ is the vacuum permeability, the $\boldsymbol{m}_i$ and $\boldsymbol{m}_j$ are the magnetic moments of the dipoles and the $\boldsymbol{r}_{ij}$ is the distance vector between them, with $r_{ij} = |\boldsymbol{r}_{ij}|$. K_1 is the first-order anisotropy constant which is $-1.1 \times 10^{+5}\mathrm{Jm}^{-3}$ for magnetite at room temperature (Bickford, 1950). It is assumed that all dipoles have equal absolute value $|\boldsymbol{m}_i| = m$ and that the magnetosome chains are fixed in their location. The magnetocrystalline anisotropy energy is defined as a cubic lattice, oriented with the [111] axis in the direction of the chain. For magnetite, the direction of the easy magnetization is indeed the diagonal [111] and in magnetotactic bacteria, the direction of the chain axis (filament) overlaps with the easy axis for most crystals (Scheffel, et al., 2006).

The Monte Carlo simulation is carried out at room temperature under an external magnetic field with angle π with respect to the direction of the chain. Each Monte Carlo step includes a random change between – 5 to + 5 degree in the polar and azimuthal orientation of the magnetic moment for every single particle. The total number of steps in the simulation is 10^{+7}. The magnetic moment direction of the chain is measured in every step of the increasing external field, starting from 0 to 120 mT.

Experimentally, the applied reversing field had to reach a specific strength of 72mT to be able to change the magnetization direction of the linear magnetosome chain structure. This is because the external field has to overcome an energy barrier in this structure, caused by the effect of inter-particles dipole interactions and magnetocrystalline anisotropy. From simulating the interaction of the external magnetic field with the chain and calculating the magnetization equilibrium moments, the required field for overcoming the energy barrier is calculated in two conditions with and without magnetosome membrane.

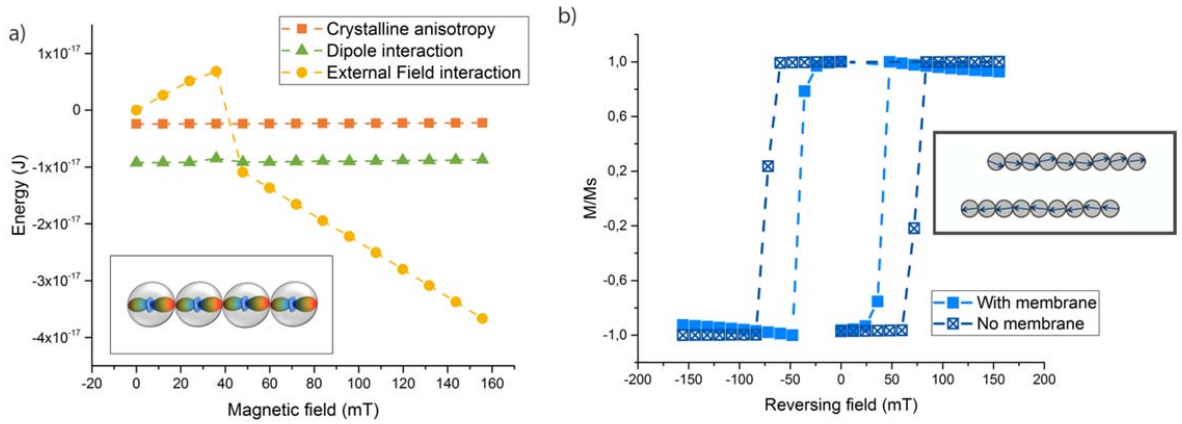

Figure 3.27 Simulation results for a linear magnetosome chain. a) The calculated energies for a single particle in the chain. The inset is a graphical demonstration of the energies of each particle in the middle of the chain, counting the dipole interaction and the magnetocrystalline energies. b) The calculated remanence curve of a linear chain. The two colors are showing results for the magnetosomes with and without the membrane.

The calculated coercivity field of remanence for the chain is 48 mT, which is smaller than the experimental value (72 mT). During the theoretical magnetization reversing mechanism, of each particle in the chain, the equilibrium states direction (calculated by the Monte-Carlo simulation) is following a "semi-symmetrical fanning mechanism" as described by Jacob and Bean (Jacobs and Bean, 1955). When the magnetization is reversed through a fanning configuration, the energy trajectory is lower and reversing occurs in lower fields comparing to a "coherent rotation" suggested by the Stoner-Wohlfarth (SW) theory (Stoner and Wohlfarth, 1948). Besides, the theoretical assumption is that particles are perfect spheres, but it has been shown that even a small elongation of the shape in magnetite will cause an anisotropy which can be in the same order of the magnetocrystalline anisotropy (Rudolf, et al., 2008).

3.2.3 Discussions on the magnetic stability of magnetosome assemblies

Magnetocrystalline anisotropy of a single crystal magnetite is reported to be ~11-14 kJ/m^3 (Hansen and Mørup, 1998). Contribution of the shape anisotropy can significantly vary due to small changes in the sample geometry, and thus reported values for anisotropy of magnetite ensembles is in a wide range of 10-41 kJ/m^3 (Deatsch and Evans, 2014). As it has already been mentioned in section 3.1, FMR is one of the standard and frequently used techniques for measuring the magnetic anisotropy of ferromagnetic material, and for the magnetosome chains as well (Ghaisari, et al., 2017),(Charilaou, et al., 2011, Gehring and Charilaou, 2011, Kobayashi, et al., 2006, Kopp, et al., 2006). But one drawback of FMR is the strong dependency of the results on numerical simulations, which is the only way to extract the magnetic anisotropies from the measured resonance fields. Besides, the FMR spectrum of a bulk sample is the superposition of

all the modes caused by the diversity of magnetic interactions in the sample. The measured reversing field (B_{rev}) for each specific structure can be an estimate of the anisotropy field of that structure, and consequently the effective anisotropy (K_{eff}) of the structure can be directly calculated from:

$$\Delta E = K_{eff} V, \qquad (3.5)$$

where on the other hand

$$\Delta E = -\vec{m}.\vec{B}_{rev}. \qquad (3.6)$$

thus the effective anisotropy is calculated from

$$K_{eff} = M_s.\vec{B}_{rev}., \qquad (3.7)$$

where M_s is the saturation magnetization of magnetite.

The results of this calculation are shown in Table 1, and the anisotropy fields are also compared with values reported in previous FMR works.

Table 3.4 The measured reversing fields and calculated effective anisotropies for different magnetosome structures.

	straight chain	Cluster	segmented chain
Anisotropy fields from FMR studies [mT]	87±5 , intact (Charilaou, et al., 2011) 88±20 , intact (Ghaisari, et al., 2017)	40 , intact Δ*mamJ*	-
	63.6±0.7 , isolated magnetosomes (Kopp, et al., 2006)	43±0.8 , isolated magnetosomes (Kopp, et al., 2006)	-
Current experimental reversing field [mT]	67.5±4.5	40.5±4.5	58.5±4.5
Calculated Effective anisotropy [kJ/m^3]	32.4±2	19.44±2	28.08±2

The average anisotropy field of a magnetosome chain ensemble in previous FMR studies has been reported to be in a range of 63mT for isolated chains and 43mT for clusters of magnetosomes (Kopp, et al., 2006). Although the measured magnetosomes in the work of Kopp et. al. are from a different strain (Kopp, et al., 2006), the range of the results are comparable to what is measured *via* XPEEM for a single structure. The average anisotropy of intact cells are reported to be higher than the isolated chains(Ghaisari, et al., 2017),(Charilaou, et al., 2011), where this can be due to higher ordered particles in the cells. The anisotropy field of the cluster is comparable with reported values from the intact cells of the MSR-1 Δ*mamJ* mutant. This mutant is known for having magnetosome particles in a cluster arrangement (Scheffel, et al., 2006).

The remanence curve and effective anisotropy of the linear magnetosome chain, show the stability of magnetization for this assembly. The magnetosome particles have a size range of

magnetic single domain ferromagnets, thus each magnetosome has a permanent magnetic moment. The magnetic stability of the assembly as a whole is then only affected by the dipole interactions between the particles, which can change through the change of their configuration. The results for the linear chain show that a uniform direction of magnetic moments in this structure, causes a stable total magnetic moment with a high magnetic anisotropy. The clustered configuration, with the lower effective anisotropy, and random orientation of particles in the assembly, confirms the opposite case. The non-uniform dipole interaction of similar single domain particles, results a low magnetic stability in the whole structure.

3.3 An Application of Anisotropy Analysis

This project is initiated by Dr. Victoria Reichel and Dr. Matthew Hood in the group of Dr. Damien Faivre at MPIKG. The aim is to embed organized magnetic fillers within calcite ($CaCO_3$) crystals. This makes the calcite crystals magnetoresponsive and can be of interest in several applications, such as magnetic tunable filtration system, sensors, or encapsulation of bio-active molecules for drug delivery (Mihai, et al., 2013), (Ikoma, et al., 2007). For this purpose, synthetic magnetite chains and magnetosomes isolated from MTB were utilized. The elongated chains can then provide a sufficient torque on the calcite crystals when placed in a magnetic field. The calcite is precipitated, in a solution with magnetite chins, and in the presence of a magnetic field so that the chains aligned while getting are trapped in the crystals..

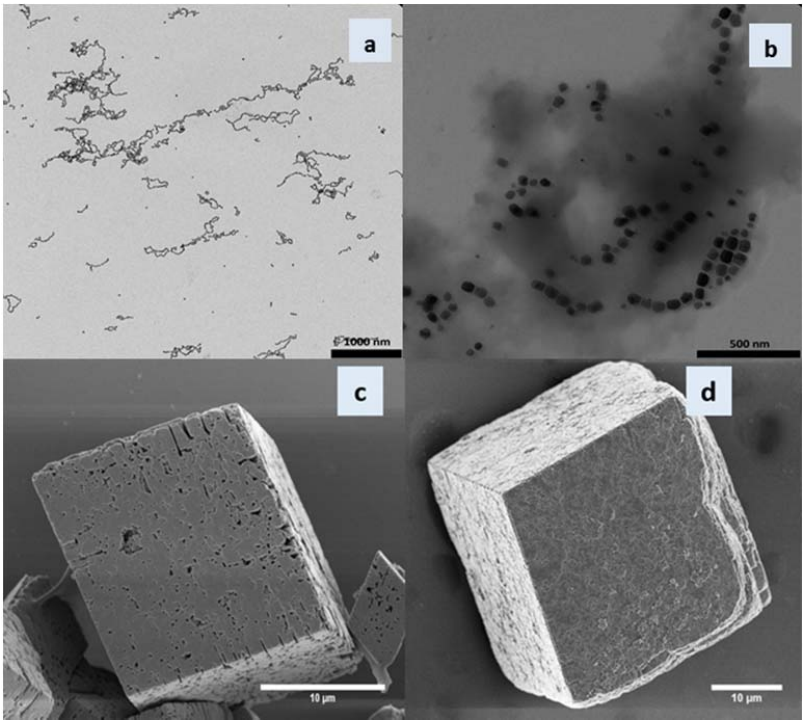

Figure 3.28 SEM images of calcite crystals after vapor diffusion decomposition method. a) Synthetic magnetite chains. b) MTB isolated magnetosomes. c) Calcite crystals entrapping synthetic magnetite chains. d) Calcite crystals entrapping MTB isolated magnetosomes [Image with permission from Dr. Victoria Reichel].

One of the practical issues of this project was to indicate the existence of the magnetite chains in the calcite crystals, and the linearity of the chains after the precipitation. In this case, FMR is a suitable tool to investigate the elongation of the chains, by measuring their uniaxial anisotropy. Angular dependent measurements are performed on the sample. Before the FMR measurement, a magnetic field of 30 mT is applied on the sample, with the purpose of aligning the chains-crystal combinations. After a few seconds, the sample is frozen with the field being applied. Angular dependent FMR measurements are shown in Figure 3.29.

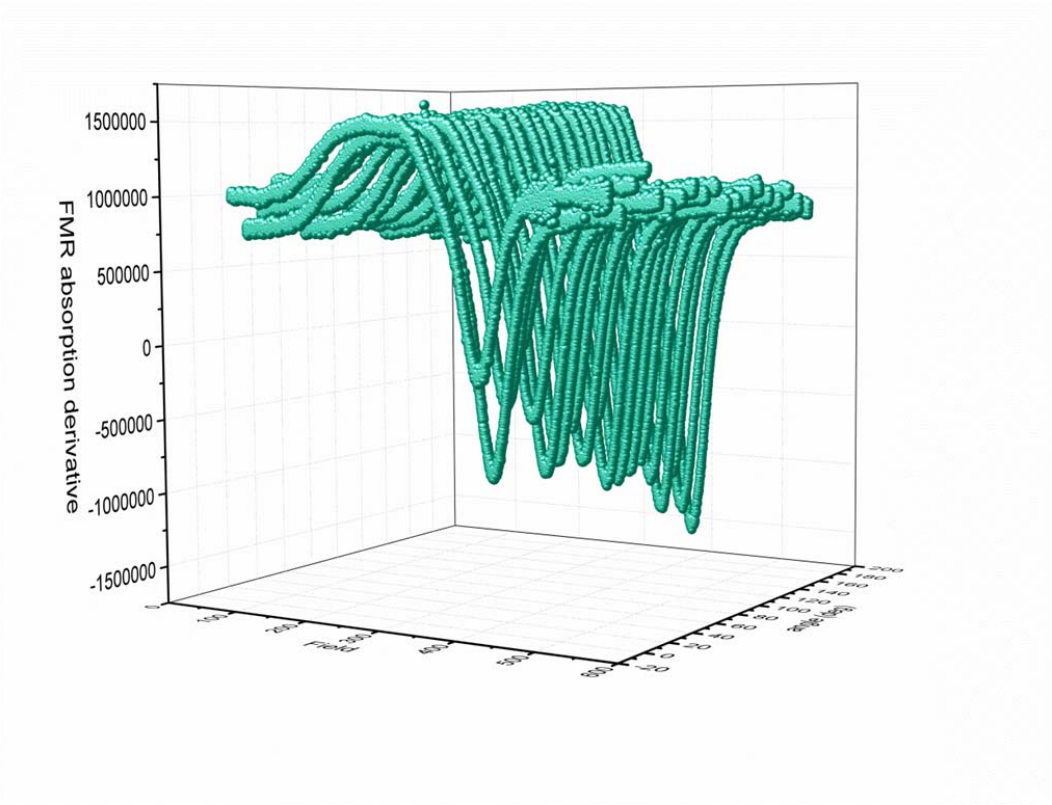

Figure 3.29 FMR spectra of calcite crystals containing chains of nanoparticles.

From this measurement, no angular dependency is observed, but the FMR spectrum at each angle has a line shape of a uniaxial chain, comparable with the randomly aligned MSR-1 wild type cells. It can be concluded that the chains are not clustered of agglomerated with in the calcite, otherwise the spectra would have been symmetric. The FMR spectra of Δ*mamJ* is a good reference for this. But angular independency, indicates that there is also no alignment of chain-calcite structures in the sample. This can be due to two reasons; Either that the chains were not well aligned with the magnetic field during precipitation, and are embedded randomly during the precipitation, or that the chain-calcite structures are too heavy and the magnetic torque of the

chain is not sufficient for rotating them. This work is still an ongoing project with further investigation on the questions.

4 Conclusions and Outlook

4.1 Conclusions

In this work, a framework of experimental and theoretical analysis is developed to study the anisotropy of magnetosome assemblies. The aim was to characterize the anisotropy properties through FMR and PEEM in both bulk and single particle scale, and use this for two main purposes:

- Characterizing the average anisotropy in a bulk sample and correlating this to both the particle configuration and structure orientation.
- Estimating the magnetic stability of various formed particle configurations, based on their anisotropies.

I presented how FMR line shape changes for different magnetosome configurations can be utilized as a method to characterize the average anisotropy properties of a bulk sample. The MSR-1 WT, Δ*mamJ, and* Δ*F3* strains were used as reference samples, giving us access to coherent samples with linear chains, isotropic clusters and randomly scattered configurations of single domain nanoparticles, respectively. It has been shown that the symmetry of the FMR spectrum line is directly correlated with the uniaxial (shape) anisotropy of the magnetosome assemblies. The uniaxial anisotropy of WT and Δ*mamJ* cells was also estimated, using FMR

simulations. Moreover, the angular dependent FMR measurement is a proper method for indicating the alignment of structures in a bulk sample. If the spectrum is independent of the measured angle, there is no particular orientation, and the structures are randomly aligned. But an angular dependency of the spectra can be a measure for the chains alignment. I enhanced this orientation analysis by adding a distribution of orientations to the modeled sample and evaluating the distribution that can be in the measured sample. Samples of Δ*F3* cells with scattered single magnetosomes also provided an excellent opportunity to observe the influence of magnetocrystalline anisotropy of the magnetosomes. Since in the magnetosome chain structures the uniaxial anisotropy is stronger and can dominate the effect of magnetocrystalline anisotropy. The effective resonance field (H_{res}), the field in which maximum absorption occurs, is also used as an indicator of the sample's anisotropy and orientation. The range of the effective resonance field can be also associated with the anisotropy magnitude. Table 3.3 summarizes these values for different samples.

In addition to the anisotropy analysis, the XPEEM measurement is performed to evaluate the magnetization stability of different magnetosome configurations. The linear chain has the most stable magnetization of all studied configurations. It acts as a single domain structure with a high remanence up to 72 mT. The value is comparable to the uniaxial anisotropies deciphered from the FMR simulation. This verifies the capability of FMR as a tool for determining the average uniaxial anisotropy of a bulk sample of MTB, and thus characterizing the magnetosomes structural properties.

4.2 Outlook

As it has been discussed, the FMR spectrum of the bulk sample is a superposition of all the possible different resonance modes in the sample. The variety of modes is caused by the diversity of uniaxial anisotropies (chain lengths). Since the effective resonance field is directly correlated with the uniaxial anisotropy, the diversity of uniaxial anisotropies in a bulk sample will cause the resonance condition to be fulfilled in a wider field range. One suggestion for further studies is to use the FMR spectrum of the single chain as a basis function for a Fourier transform of a bulk experimental FMR spectrum. From these analyses, one can theoretically apply a Fourier transform on the bulk spectra and presumably extract the distribution of chain lengths, as well as the frequency (population) of each length in the bulk sample. This can improve the application of FMR spectra analysis, as a tool to study the magnetosome chain length distribution in bulk samples of magnetotactic bacteria.

Bibliography

Abraçado, L. G., E. Wajnberg, D. M. S. Esquivel, C. N. Keim, K. T. Silva, E. T. S. Moreira, U. Lins and M. Farina. (2014), 'Ferromagnetic Resonance of Intact Cells and Isolated Crystals from Cultured and Uncultured Magnetite-Producing Magnetotactic Bacteria', *Physical biology* Vol. 11, No. 3, pp. 036006-036006.

Anders, S., H. A. Padmore, R. M. Duarte, T. Renner, T. Stammler, A. Scholl, M. R. Scheinfein, J. Stöhr, L. Séve and B. Sinkovic. (1999), 'Photoemission Electron Microscope for the Study of Magnetic Materials', *Review of Scientific Instruments* Vol. 70, No. 10, pp. 3973-3981.

Arakaki, A., J. Webb and T. Matsunaga. (2003), 'A Novel Protein Tightly Bound to Bacterial Magnetic Particles in Magnetospirillum Magneticum Strain Amb-1', *J Biol Chem* Vol. 278, No. 10, pp. 8745-50.

Bazylinski, D. A. and R. B. Frankel. (2004), 'Magnetosome Formation in Prokaryotes', *Nature Reviews Microbiology* Vol. 2, No. 3, pp. 217-230.

Bazylinski, D. A., R. B. Frankel and H. W. Jannasch. (1988), 'Anaerobic Magnetite Production by a Marine, Magnetotactic Bacterium', *Nature* Vol. 334, No. 6182, pp. 518-519.

Bellini, S. (1963), 'Su Di Un Particolare Comportamento Di Batteri D'acqua Dolce', *Università di Pavia.*

Bickford, L. R. (1950), 'Ferromagnetic Resonance Absorption in Magnetite Single Crystals', *Physical Review* Vol. 78, No. 4, pp. 449-457.

Blachowicz, T. and A. Ehrmann. (2016), 'Stability of Magnetic Nano-Structures with Respect to Shape Modifications', *Journal of Physics: Conference Series* Vol. 738, No. 1, pp. 012058.

Blakemore, R. (1975), 'Magnetotactic Bacteria', *Science* Vol. 190, No. 4212, pp. 377.

Brüche, E. (1933), 'Elektronenmikroskopische Abbildung Mit Lichtelektrischen Elektronen', *Zeitschrift für Physik* Vol. 86, No. 7-8, pp. 448.

Ceylan, S., C. Friese, C. Lammel, K. Mazac and A. Kirschning. (2008), 'Inductive Heating for Organic Synthesis by Using Functionalized Magnetic Nanoparticles inside Microreactors', *Angewandte Chemie International Edition* Vol. 47, No. 46, pp. 8950-8953.

Chang, L., D. Heslop, A. P. Roberts, D. Rey and K. J. Mohamed. (2016), 'Discrimination of Biogenic and Detrital Magnetite through a Double Verwey Transition Temperature', *Journal of Geophysical Research: Solid Earth* Vol. 121, No. 1, pp. 3-14.

Chariaou, M., L. Rahn-Lee, J. Kind, I. García-Rubio, A. Komeili and Andreas U. Gehring. (2015), 'Anisotropy of Bullet-Shaped Magnetite Nanoparticles in the Magnetotactic

Bacteria Desulfovibrio Magneticus Sp. Strain Rs-1', *Biophysical Journal* Vol. 108, No. 5, pp. 1268-1274.

Charilaou, M., J. Kind, I. García-Rubio, D. Schüler and A. U. Gehring. (2014), 'Magnetic Anisotropy of Non-Interacting Collinear Nanocrystal-Chains', *Applied Physics Letters* Vol. 104, No. 11.

Charilaou, M., M. Winklhofer and A. U. Gehring. (2011), 'Simulation of Ferromagnetic Resonance Spectra of Linear Chains of Magnetite Nanocrystals', *Journal of Applied Physics* Vol. 109, No. 9, pp. 1-6.

Chiba, K., K. Suzuki and S. Chikazumi. (1975), 'Diffuse Electron Scattering from Magnetite above the Verwey Transition Temperature', *Journal of the Physical Society of Japan* Vol. 39, No. 3, pp. 839-840.

David, L. G. (1981), 'Ferromagnetic Resonance Condition and Powder Pattern Analysis for Dilute, Spherical, Single-Domain Particles of Cubic Crystal Structure', *Journal of Magnetic resonance* Vol. 45, pp. 81-87.

Deatsch, A. E. and B. A. Evans. (2014), 'Heating Efficiency in Magnetic Nanoparticle Hyperthermia', *Journal of Magnetism and Magnetic Materials* Vol. 354, pp. 163-172.

Einstein, A. (1905), 'On a Heuristic Point of View Concerning the Production and Transformation of Light.', *Annalen der Physik*.

Faivre, D. (2015), 'Formation of Magnetic Nanoparticle Chains in Bacterial Systems', *MRS Bulletin* Vol. 40, No. 06, pp. 509-515.

Faivre, D. and T. U. Godec. (2015), 'From Bacteria to Mollusks: The Principles Underlying the Biomineralization of Iron Oxide Materials', *Angewandte Chemie - International Edition* Vol. 54, No. 16, pp. 4728-4747.

Faivre, D., N. Menguy, M. Pósfai and D. Schüler. (2008), 'Environmental Parameters Affect the Physical Properties of Fast-Growing Magnetosomes', *American Mineralogist* Vol. 93, No. 2-3, pp. 463-469.

Faivre, D. and D. Schüler. (2008), 'Magnetotactic Bacteria and Magnetosomes', *Chemical Reviews* Vol. 108, No. 11, pp. 4875-4898.

Feng, J., E. Forest, A. A. MacDowell, M. Marcus, H. Padmore, S. Raoux, D. Robin, A. Scholl, R. Schlueter, P. Schmid, J. Stöhr, W. Wan, D. H. Wei and Y. Wu. (2005), 'An X-Ray Photoemission Electron Microscope Using an Electron Mirror Aberration Corrector for the Study of Complex Materials', *Journal of Physics: Condensed Matter* Vol. 17, No. 16, pp. S1339.

Feng, J. and A. Scholl. (2007), 'Photoemission Electron Microscopy (Peem)', In P. W. Hawkes and J. C. H. Spence (Eds.), *Science of Microscopy*, Springer New York.

Fink, R., M. R. Weiss, E. Umbach, D. Preikszas, H. Rose, R. Spehr, P. Hartel, W. Engel, R. Degenhardt, R. Wichtendahl, H. Kuhlenbeck, W. Erlebach, K. Ihmann, R. Schlögl, H. J. Freund, A. M. Bradshaw, G. Lilienkamp, T. Schmidt, E. Bauer and G. Benner. (1997), 'Smart: A Planned Ultrahigh-Resolution Spectromicroscope for Bessy Ii', *Journal of Electron Spectroscopy and Related Phenomena* Vol. 84, No. 1, pp. 231-250.

Fischer, H., G. Mastrogiacomo, J. F. Löffler, R. J. Warthmann, P. G. Weidler and A. U. Gehring. (2008), 'Ferromagnetic Resonance and Magnetic Characteristics of Intact Magnetosome Chains in Magnetospirillum Gryphiswaldense', *Earth and Planetary Science Letters* Vol. 270, No. 3, pp. 200-208.

Fisher, R. (1953), 'Dispersion on a Sphere', *Proceedings of the Royal Society* Vol. A, pp. 295-305.

Fletcher, G. C. (1954), 'Calculations of the First Ferromagnetic Anisotropy Coefficient, Gyromagnetic Ratio and Spectroscopic Splitting Factor for Nickel', *Proceedings of the Physical Society. Section A* Vol. 67, No. 6, pp. 505.

Frankel, R. B., D. A. Bazylinski, M. S. Johnson and B. L. Taylor. (1997), 'Magneto-Aerotaxis in Marine Coccoid Bacteria', *Biophysical Journal* Vol. 73, No. 2, pp. 994-1000.

Gao, J., H. Gu and B. Xu. (2009), 'Multifunctional Magnetic Nanoparticles: Design, Synthesis, and Biomedical Applications', *Accounts of Chemical Research* Vol. 42, No. 8, pp. 1097-1107.

Gehring, A. U. and M. Charilaou. (2011), 'Magnetic Anisotropy and Verwey Transition of Magnetosome Chains in Magnetospirillum Gryphiswaldense', *Geophys. J. Int.*, pp. 1215-1221.

Ghaisari, S., M. Winklhofer, P. Strauch, S. Klumpp and D. Faivre. (2017), 'Magnetosome Organization in Magnetotactic Bacteria Unraveled by Ferromagnetic Resonance Spectroscopy', *Biophysical Journal* Vol. 113, No. 3, pp. 637-644.

Goering, E. (2011), 'Large Hidden Orbital Moments in Magnetite', *physica status solidi (b)* Vol. 248, No. 10, pp. 2345-2351.

Goering, E., S. Gold, M. Lafkioti and G. Schütz. (2006), 'Vanishing Fe 3d Orbital Moments in Single-Crystalline Magnetite', *EPL (Europhysics Letters)* Vol. 73, No. 1, pp. 97.

Goya, G. F., T. S. Berquó, F. C. Fonseca and M. P. Morales. (2003), 'Static and Dynamic Magnetic Properties of Spherical Magnetite Nanoparticles', *Journal of Applied Physics* Vol. 94, No. 5, pp. 3520-3528.

Grünberg, K., E.-C. Müller, A. Otto, R. Reszka, D. Linder, M. Kube, R. Reinhardt and D. Schüler. (2004), 'Biochemical and Proteomic Analysis of the Magnetosome Membrane in Magnetospirillum Gryphiswaldense', *Applied and Environmental Microbiology* Vol. 70, No. 2, pp. 1040-1050.

Hansen, M. F. and S. Mørup. (1998), 'Models for the Dynamics of Interacting Magnetic Nanoparticles', *Journal of Magnetism and Magnetic Materials* Vol. 184, No. 3, pp. L262-274.

Hanzlik, M., M. Winklhofer and N. Petersen. (2002), 'Pulsed-Field-Remanence Measurements on Individual Magnetotactic Bacteria', *Journal of Magnetism and Magnetic Materials* Vol. 248, No. 2, pp. 258-267.

Heyen, U. and D. Schüler. (2003), 'Growth and Magnetosome Formation by Microaerophilic Magnetospirillum Strains in an Oxygen-Controlled Fermentor', *Applied microbiology and biotechnology* Vol. 61, No. 5-6, pp. 536-544.

Ikoma, T., T. Tonegawa, H. Watanaba, G. Chen, J. Tanaka and Y. Mizushima. (2007), 'Drug-Supported Microparticles of Calcium Carbonate Nanocrystals and Its Covering with Hydroxyapatite', *Journal of nanoscience and nanotechnology* Vol. 7, No. 3, pp. 822-827.

Isambert, A., N. Menguy, E. Larquet, F. Guyot and J. P. Valet. (2007), 'Transmission Electron Microscopy Study of Magnetites in a Freshwater Population of Magnetotactic Bacteria', *American Mineralogist* Vol. 92, No. 4, pp. 621.

Jacobs, I. S. and C. P. Bean. (1955), 'An Approach to Elongated Fine-Particle Magnets', *Physical Review* Vol. 100, No. 4, pp. 1060-1067.

Kaiskol, Z. and J. M. Honig. (1989), 'Influence of Deviations from Ideal Stoichiometry on the Anisotropy Parameters of Magnetite Fe3(1−Δ)O4', *Physical Review B* Vol. 40, No. 13, pp. 9090-9097.

Katzmann, E., A. Scheffel, M. Gruska, J. M. Plitzko and D. Schüler. (2010), 'Loss of the Actin-Like Protein Mamk Has Pleiotropic Effects on Magnetosome Formation and Chain Assembly in Magnetospirillum Gryphiswaldense', *Molecular Microbiology* Vol. 77, No. 1, pp. 208-224.

Kiani, B., D. Faivre and S. Klumpp. (2015), 'Elastic Properties of Magnetosome Chains', *New Journal of Physics* Vol. 17, No. April.

Klumpp, S. and D. Faivre. (2012), 'Interplay of Magnetic Interactions and Active Movements in the Formation of Magnetosome Chains', *PLOS ONE* Vol. 7, No. 3, pp. e33562.

Kobayashi, A., J. L. Kirschvink, C. Z. Nash, R. E. Kopp, D. A. Sauer, L. E. Bertani, W. F. Voorhout and T. Taguchi. (2006), 'Experimental Observation of Magnetosome Chain Collapse in Magnetotactic Bacteria : Sedimentological , Paleomagnetic , and Evolutionary Implications', Vol. 245, pp. 538-550.

Komeili, A., Z. Li, D. K. Newman and G. J. Jensen. (2006), 'Magnetosomes Are Cell Membrane Invaginations Organized by the Actin-Like Protein Mamk', *Science* Vol. 311, No. 5758, pp. 242.

Kopp, R. E., C. Z. Nash, A. Kobayashi, B. P. Weiss, D. A. Bazylinski and J. L. Kirschvink. (2006), 'Ferromagnetic Resource Spectroscopy for Assessment of Magnetic Anisotropy and Magnetostatic Interactions: A Case Study of Mutant Magnetotactic Bacteria', *Journal of Geophysical Research: Solid Earth* Vol. 111, No. 12, pp. 1-15.

Körnig, A., J. Dong, M. Bennet, M. Widdrat, J. Andert, F. D. Müller, D. Schüler, S. Klumpp and D. Faivre. (2014), 'Probing the Mechanical Properties of Magnetosome Chains in Living Magnetotactic Bacteria', *Nano Letters* Vol. 14, No. 8, pp. 4653-4659.

Körnig, A., M. Winklhofer, J. Baumgartner, T. P. Gonzalez, P. Fratzl and D. Faivre. (2014), 'Magnetite Crystal Orientation in Magnetosome Chains', *Advanced Functional Materials* Vol. 24, No. 25, pp. 3926-3932.

Kraupner, A., D. Eberbeck, D. Heinke, R. Uebe, D. Schuler and A. Briel. (2017), 'Bacterial Magnetosomes - Nature's Powerful Contribution to Mpi Tracer Research', *Nanoscale* Vol. 9, No. 18, pp. 5788-5793.

Kronast, F., N. Friedenberger, K. Ollefs, S. Gliga, L. Tati-bismaths, R. Thies, A. Ney, R. Weber, C. Hassel, M. R. Florian, A. V. Trunova, C. Wirtz, R. Hertel, A. D. Hermann and M. Farle. (2011), 'Element-Specific Magnetic Hysteresis of Individual 18 Nm Fe Nanocubes', *Nano Lett.* Vol. 11, pp. 1710-1715.

Kronast, F. and S. Valencia. (2016), 'Speem : The Photoemission Microscope at the Dedicated Microfocus Pgm Beamline Ue49-Pgma at Bessy Ii', *Journal of large-scale research facilities* Vol. 2, No. A90, pp. 1–6

Kumari, M., M. Widdrat, É. Tompa, R. Uebe, D. Schüler, M. Pósfai, D. Faivre and A. M. Hirt. (2014), 'Distinguishing Magnetic Particle Size of Iron Oxide Nanoparticles with First-Order Reversal Curves', *Journal of Applied Physics* Vol. 116, No. 12, pp. 124304.

Kurtoğlu, E., A. Bilgin, M. Şeşen, B. Mısırlıoğlu, M. Yıldız, H. F. Y. Acar and A. Koşar. (2012), 'Ferrofluid Actuation with Varying Magnetic Fields for Micropumping Applications', *Microfluidics and Nanofluidics* Vol. 13, No. 4, pp. 683-694.

Lee, Y., J. Lee, C. J. Bae, J. G. Park, H. J. Noh, J. H. Park and T. Hyeon. (2005), 'Large-Scale Synthesis of Uniform and Crystalline Magnetite Nanoparticles Using Reverse Micelles as Nanoreactors under Reflux Conditions', *Advanced Functional Materials* Vol. 15, No. 3, pp. 503-509.

Lefèvre, C. T., F. Abreu, U. Lins and D. A. Bazylinski. (2011), 'A Bacterial Backbone: Magnetosomes in Magnetotactic Bacteria', In M. Rai and N. Duran (Eds.), Springer Berlin Heidelberg.

Li, J., K. Ge, Y. Pan, W. Williams, Q. Liu and H. Qin. (2013), 'A Strong Angular Dependence of Magnetic Properties of Magnetosome Chains: Implications for Rock Magnetism and Paleomagnetism', *Geochemistry, Geophysics, Geosystems* Vol. 14, No. 10, pp. 3887-3907.

Linder J. , R. Meckenstock and M. Farle. (2012), 'Applications of Ferromagnetic Resonance', In E. N. Kaufmann (Ed.), Wiley.

Liu, C.-M., L. Guo, R.-M. Wang, Y. Deng, H.-B. Xu and S. Yang. (2004), 'Magnetic Nanochains of Metal Formed by Assembly of Small Nanoparticles', *Chemical Communications*, No. 23, pp. 2726-2727.

Lohße, A., I. Kolinko, O. Raschdorf, R. Uebe, S. Borg, A. Brachmann, J. M. Plitzko, R. Müller, Y. Zhang and D. Schüler. (2016), 'Overproduction of Magnetosomes by Genomic Amplification of Biosynthesis-Related Gene Clusters in a Magnetotactic Bacterium', *Applied and Environmental Microbiology* Vol. 82, No. 10, pp. 3032-3041.

Mann, S., R. B. Frankel and R. P. Blakemore. (1984), 'Structure, Morphology and Crystal Growth of Bacterial Magnetite', *Nature* Vol. 310, No. 5976, pp. 405-407.

Martel, S., M. Mohammadi, O. Felfoul, L. Zhao and P. Pouponneau. (2009), 'Flagellated Magnetotactic Bacteria as Controlled Mri-Trackable Propulsion and Steering Systems for Medical Nanorobots Operating in the Human Microvasculature', *The International Journal of Robotics Research* Vol. 28, No. 4, pp. 571-582.

Mastrogiacomo, G., H. Fischer, I. Garcia-Rubio and A. U. Gehring. (2010), 'Ferromagnetic Resonance Spectroscopic Response of Magnetite Chains in a Biological Matrix', *Journal of Magnetism and Magnetic Materials* Vol. 322, No. 6, pp. 661-663.

Matsunaga, T., T. Sakaguchi and F. Tadakoro. (1991), 'Magnetite Formation by a Magnetic Bacterium Capable of Growing Aerobically', *Applied microbiology and biotechnology* Vol. 35, No. 5, pp. 651-655.

Meldrum, F. C. (1993), 'Electron Microscopy Study of Magnetosomes in a Cultured Coccoid Magnetotactic Bacterium', *Proceedings of the Royal Society of London. Series B* Vol. Biological Sciences, No. 251, pp. 31–236.

Mihai, M., V. Socoliuc, F. Doroftei, E.-L. Ursu, M. Aflori, L. Vekas and B. C. Simionescu. (2013), 'Calcium Carbonate–Magnetite–Chondroitin Sulfate Composite Microparticles with Enhanced Ph Stability and Superparamagnetic Properties', *Crystal Growth & Design* Vol. 13, No. 8, pp. 3535-3545.

Moskowitz, B. M., R. B. Frankel, P. J. Flanders, R. P. Blakemore and B. B. Schwartz. (1988), 'Magnetic Properties of Magnetotactic Bacteria', *Journal of Magnetism and Magnetic Materials* Vol. 73, No. 3, pp. 273-288.

Narkowicz, R., D. Suter and I. Niemeyer. (2008), 'Scaling of Sensitivity and Efficiency in Planar Microresonators for Electron Spin Resonance', *Review of Scientific Instruments* Vol. 79, No. 8, pp. 084702.

Narkowicz, R., D. Suter and R. Stonies. (2005), 'Planar Microresonators for Epr Experiments', *Journal of Magnetic resonance* Vol. 175, No. 2, pp. 275-284.

Osborn, J. A. (1945), 'Demagnetizing Factors of the General Ellipsoid', *Physical Review* Vol. 67, No. 11-12, pp. 351-357.

Özdemir, Ö., D. J. Dunlop and B. M. Moskowitz. (1993), 'The Effect of Oxidation on the Verwey Transition in Magnetite', *Geophysical Research Letters* Vol. 20, No. 16, pp. 1671-1674.

Pan, Y., N. Petersen, M. Winklhofer, A. F. Davila, Q. Liu, T. Frederichs, M. Hanzlik and R. Zhu. (2005), 'Rock Magnetic Properties of Uncultured Magnetotactic Bacteria', *Earth and Planetary Science Letters* Vol. 237, No. 3-4, pp. 311-325.

Pankhurst, Q. A., J. Connolly, S. K. Jones and J. Dobson. (2003), 'Applications of Magnetic Nanoparticles in Biomedicine', *Journal of Physics D: Applied Physics* Vol. 36, No. 13, pp. R167.

Penninga, I., H. de Waard, B. M. Moskowitz, D. A. Bazylinski and R. B. Frankel. (1995), 'Remanence Measurements on Individual Magnetotactic Bacteria Using a Pulsed Magnetic Field', *Journal of Magnetism and Magnetic Materials* Vol. 149, No. 3, pp. 279-286.

Prozorov, R., T. Prozorov, S. K. Mallapragada, B. Narasimhan, T. J. Williams and D. A. Bazylinski. (2007), 'Magnetic Irreversibility and the Verwey Transition in Nanocrystalline Bacterial Magnetite', *Physical Review B - Condensed Matter and Materials Physics* Vol. 76, No. 5, pp. 1-10.

Prozorov, T., D. A. Bazylinski, S. K. Mallapragada and R. Prozorov. (2013), 'Novel Magnetic Nanomaterials Inspired by Magnetotactic Bacteria: Topical Review', *Materials Science and Engineering: R: Reports* Vol. 74, No. 5, pp. 133-172.

Rozenberg, G. K., M. P. Pasternak, W. M. Xu, Y. Amiel, M. Hanfland, M. Amboage, R. D. Taylor and R. Jeanloz. (2006), 'Origin of the Verwey Transition in Magnetite', *Physical Review Letters* Vol. 96, No. 4, pp. 045705.

Rudolf, H., D. Silvio and R. Michael. (2008), 'Effects of Size Distribution on Hysteresis Losses of Magnetic Nanoparticles for Hyperthermia', *Journal of Physics: Condensed Matter* Vol. 20, No. 38, pp. 385214.

Sakaguchi, T., N. Tsujimura and T. Matsunaga. (1996), 'A Novel Method for Isolation of Magnetic Bacteria without Magnetic Collection Using Magnetotaxis', *Journal of Microbiological Methods* Vol. 26, No. 1, pp. 139-145.

Sandig, O., J. Herrero-Albillos, F. M. Römer, N. Friedenberger, J. Kurde, T. Noll, M. Farle and F. Kronast. (2012), 'Imaging Magnetic Responses of Nanomagnets by Xpeem', *Journal of Electron Spectroscopy and Related Phenomena* Vol. 185, No. 10, pp. 365-370.

Scheffel, A., M. Gruska, D. Faivre, A. Linaroudis, J. M. Plitzko and D. Schüler. (2006), 'An Acidic Protein Aligns Magnetosomes Along a Filamentous Structure in Magnetotactic Bacteria', *Nature* Vol. 440, No. 7080, pp. 110-4.

Scheffel, A. and D. Schüler. (2007), 'The Acidic Repetitive Domain of the Magnetospirillum Gryphiswaldense Mamj Protein Displays Hypervariability but Is Not Required for Magnetosome Chain Assembly', *Journal of Bacteriology* Vol. 189, No. 17, pp. 6437-6446.

Schleifer, K. H., D. Schüler, S. Spring, M. Weizenegger, R. Amann, W. Ludwig and M. Köhler. (1991), 'The Genus Magnetospirillum Gen. Nov. Description of Magnetospirillum Gryphiswaldense Sp. Nov. And Transfer of Aquaspirillum Magnetotacticum to Magnetospirillum Magnetotacticum Comb. Nov', *Systematic and Applied Microbiology* Vol. 14, No. 4, pp. 379-385.

Schmidt, T. H., U. Groh, R. Fink, E. Umbach, O. Schaff, W. Engel, B. Richter, H. Kuhlenbeck, R. SchlÖGl, H. J. Freund, A. M. Bradshaw, D. Preikszas, P. Hartel, R. Spehr, H. Rose, G.

Lilienkamp, E. Bauer and G. Benner. (2002), 'Xpeem with Energy-Filtering: Advantages and First Results from the Smart Project', *Surface Review and Letters* Vol. 09, No. 01, pp. 223-232.

Scholl, A., J. Stöhr, J. Lüning, J. W. Seo, J. Fompeyrine, H. Siegwart, J. P. Locquet, F. Nolting, S. Anders, E. E. Fullerton, M. R. Scheinfein and H. A. Padmore. (2000), 'Observation of Antiferromagnetic Domains in Epitaxial Thin Films', *Science* Vol. 287, No. 5455, pp. 1014.

Schütz, G., W. Wagner, W. Wilhelm, P. Kienle, R. Zeller, R. Frahm and G. Materlik. (1987), 'Absorption of Circularly Polarized X Rays in Iron', *Physical Review Letters* Vol. 58, No. 7, pp. 737-740.

Sekerka, R. F. (1969), 'Ferromagnetic Resonance Frequency in Anisotropic Crystals for Arbitrarily Oriented Field', *Physics Letters A* Vol. 29, No. 9, pp. 560-561.

Simpson, E. T., T. Kasama, M. Pósfai, P. R. Buseck, R. J. Harrison and R. E. Dunin-Borkowski. (2005), 'Magnetic Induction Mapping of Magnetite Chains in Magnetotactic Bacteria at Room Temperature and Close to the Verwey Transition Using Electron Holography', *Journal of Physics: Conference Series* Vol. 17, No. 1, pp. 108.

Stöhr, J. and H. Siegmann. (2006), *Magnetism: From Fundamentals to Nanoscale Dynamics.*, Springer

Stöhr, J. and H. C. Siegmann. (2006), *Magnetism: From Fundamentals to Nanoscale Dynamics*.

Stohr, J., Y. Wu, B. D. Hermsmeier, M. G. Samant, G. R. Harp, S. Koranda, D. Dunham and B. P. Tonner. (1993), 'Element-Specific Magnetic Microscopy with Circularly Polarized X-Rays', *Science* Vol. 259, No. 5095, pp. 658-661.

Stoner, E. C. and E. P. Wohlfarth. (1948), 'A Mechanism of Magnetic Hysteresis in Heterogeneous Alloys', *Philosophical Transactions of the Royal Society of London. Series A, Mathematical and Physical Sciences* Vol. 240, No. 826, pp. 599.

Subías, G., J. García, J. Blasco, M. Grazia Proietti, H. Renevier and M. Concepción Sánchez. (2004), 'Magnetite, a Model System for Mixed-Valence Oxides, Does Not Show Charge Ordering', *Physical Review Letters* Vol. 93, No. 15, pp. 156408.

Tang, L., X. Yang, Q. Yin, K. Cai, H. Wang, I. Chaudhury, C. Yao, Q. Zhou, M. Kwon, J. A. Hartman, I. T. Dobrucki, L. W. Dobrucki, L. B. Borst, S. Lezmi, W. G. Helferich, A. L. Ferguson, T. M. Fan and J. Cheng. (2014), 'Investigating the Optimal Size of Anticancer Nanomedicine', *Proceedings of the National Academy of Sciences* Vol. 111, No. 43, pp. 15344-15349.

Taukulis, R., M. Widdrat, M. Kumari, D. Heinke, M. Rumpler, É. Tompa, R. Uebe, A. Kraupner, A. Cebers, D. Schüler, M. Pósfai, A. M. Hirt and D. Faivre. (2015), 'Magnetic Iron Oxide Nanoparticles as Mri Contrast Agents - a Comprehensive Physical and Theoretical Study', *Magnetohydrodynamics* Vol. 51, No. 4, pp. 721-747.

Terris, B. D. and T. Thomson. (2005), 'Nanofabricated and Self-Assembled Magnetic Structures as Data Storage Media', *Journal of Physics D: Applied Physics* Vol. 38, No. 12, pp. R199.

Toulemon, D., M. V. Rastei, D. Schmool, J. S. Garitaonandia, L. Lezama, X. Cattoën, S. Bégin-Colin and B. P. Pichon. (2016), 'Enhanced Collective Magnetic Properties Induced by the Controlled Assembly of Iron Oxide Nanoparticles in Chains', *Advanced Functional Materials*, pp. n/a-n/a.

Uebe, R. and D. Schuler. (2016), 'Magnetosome Biogenesis in Magnetotactic Bacteria', *Nat Rev Micro* Vol. 14, No. 10, pp. 621-637.

Verwey, E. J. W. and P. W. Haayman. (1941), 'Electronic Conductivity and Transition Point of Magnetite ("Fe3o4")', *Physica* Vol. 8, No. 9, pp. 979-987.

Wang, H., Q.-W. Chen, L.-X. Sun, H.-p. Qi, X. Yang, S. Zhou and J. Xiong. (2009), 'Magnetic-Field-Induced Formation of One-Dimensional Magnetite Nanochains', *Langmuir* Vol. 25, No. 12, pp. 7135-7139.

Weiss, B. P., S. Sam Kim, J. L. Kirschvink, R. E. Kopp, M. Sankaran, A. Kobayashi and A. Komeili. (2004), 'Ferromagnetic Resonance and Low-Temperature Magnetic Tests for Biogenic Magnetite', *Earth and Planetary Science Letters* Vol. 224, No. 1-2, pp. 73-89.

Widdrat, M., M. Kumari, É. Tompa, M. Pósfai, A. M. Hirt and D. Faivre. (2014), 'Keeping Nanoparticles Fully Functional: Long-Term Storage and Alteration of Magnetite', *Chempluschem* Vol. 79, No. 8, pp. 1225-1233.

Wolfgang, K. (2004), 'X-Ray Magnetic Circular Dichroism for Quantitative Element-Resolved Magnetic Microscopy', *Physica Scripta* Vol. 2004, No. T109, pp. 89.

Xu, P., G. M. Zeng, D. L. Huang, C. L. Feng, S. Hu, M. H. Zhao, C. Lai, Z. Wei, C. Huang, G. X. Xie and Z. F. Liu. (2012), 'Use of Iron Oxide Nanomaterials in Wastewater Treatment: A Review', *Science of The Total Environment* Vol. 424, pp. 1-10.

Yan, L., S. Zhang, P. Chen, H. Liu, H. Yin and H. Li. (2012), 'Magnetotactic Bacteria, Magnetosomes and Their Application', *Microbiological Research* Vol. 167, No. 9, pp. 507-519.

Zhang, Y., L. Sun, Y. Fu, Z. C. Huang, X. J. Bai, Y. Zhai, J. Du and H. R. Zhai. (2009), 'The Shape Anisotropy in the Magnetic Field-Assisted Self-Assembly Chain-Like Structure of Magnetite', *The Journal of Physical Chemistry C* Vol. 113, No. 19, pp. 8152-8157.

Zhang, Z. and S. Satpathy. (1991), 'Electron States, Magnetism, and the Verwey Transition in Magnetite', *Physical Review B* Vol. 44, No. 24, pp. 13319-13331.

Zhou, W., K. Zheng, L. He, R. Wang, L. Guo, C. Chen, X. Han and Z. Zhang. (2008), 'Ni/Ni3c Core–Shell Nanochains and Its Magnetic Properties: One-Step Synthesis at Low Temperature', *Nano Letters* Vol. 8, No. 4, pp. 1147-1152.

Zhu, X., S. S. Kalirai, A. P. Hitchcock and D. A. Bazylinski. (2015), 'What Is the Correct Fe L23 X-Ray Absorption Spectrum of Magnetite?', *Journal of Electron Spectroscopy and Related Phenomena* Vol. 199, pp. 19-26.

Abbreviations

FMR	Ferromagnetic Resonance
XPEEM	X-ray photoemission electron microscopy
XMCD	X-ray Circular Magnetic Dichroism
MTB	Magnetotactic Bacteria
Δ*mamJ*	MAMJ protein deleted mutant
Δ*F3*	F proteins deleted mutant
WT	Wild type

Appendix

Appendix A

Single Cell FMR in Microresonator

The single cell FMR experiments were performed in the lab of the Prof. Farle at the University of Duisburg-Essen. This lab has recently established a setup for utilizing a microresonator for angular dependent FMR spectroscopy (microFMR). With the microFMR technique, it is possible to measure single nanoparticles with high microwave efficiency and sensitivity. The microresonators are operable within X-band frequencies (Narkowicz, et al., 2008, Narkowicz, et al., 2005).

Figure 0.1a, schematically depicts the microresonator layout. This is a 20 nm gold layer, which is placed on a high resistive silicon substrate, using electron beam lithography. The microcoil with a ~20 μm diameter is designed to concentrate the high frequency magnetic field on the sample, and is where the samples are placed. The microresonator is placed between the modulation coils and a 180 ° rotatable electromagnet.

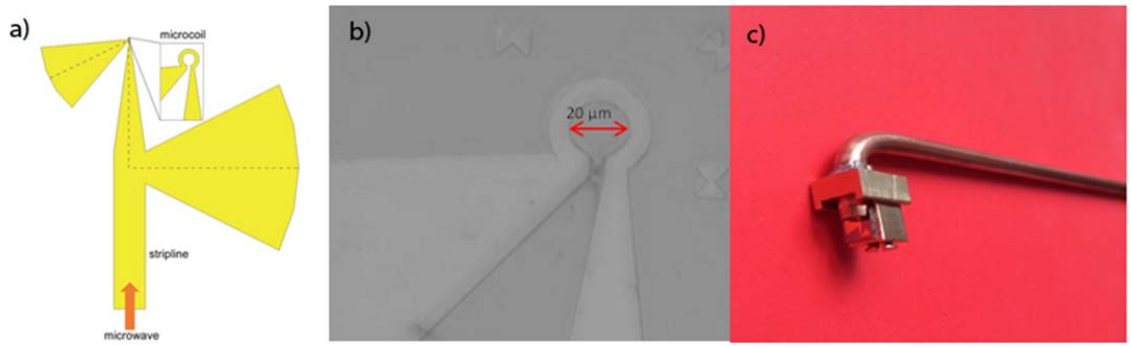

Figure 0.1 Microresonator structure. a) Schematic image of the microresonator. The inset shows a magnification of the resonator loop, in which the samples are placed and has a 20 µm diameter [Image from Master Thesis of A. Terwey with author's permission]. b) SEM image of the microcoil. c) The sample holder and connection to the microwave antenna.

The measurement is done on a microresonator, which contains two linear magnetosome chains (Figure 0.2). The microwave frequency is 9.06317 GHz and the modulation frequency is 123.45 Hz. The magnetic field scan is in a range of 0 to 600 mT with 1 mT field steps, and with an angular scan from 80 to 270 ° with 0.5 ° steps.

The single cell FMR is a convenient method investigating the resonance modes of each individual magnetosomes in a chain. This can be advantageous in two aspects. First is to have a direct measure on the magnetic anisotropies of individual magnetosomes in different configurations. Second, the basic resonance modes that are measured in the single cell experiment, can be used as the basis functions in simulations of bulk FMR spectra. This can improve the simulations to have more accurate characterization of bulk samples as well.

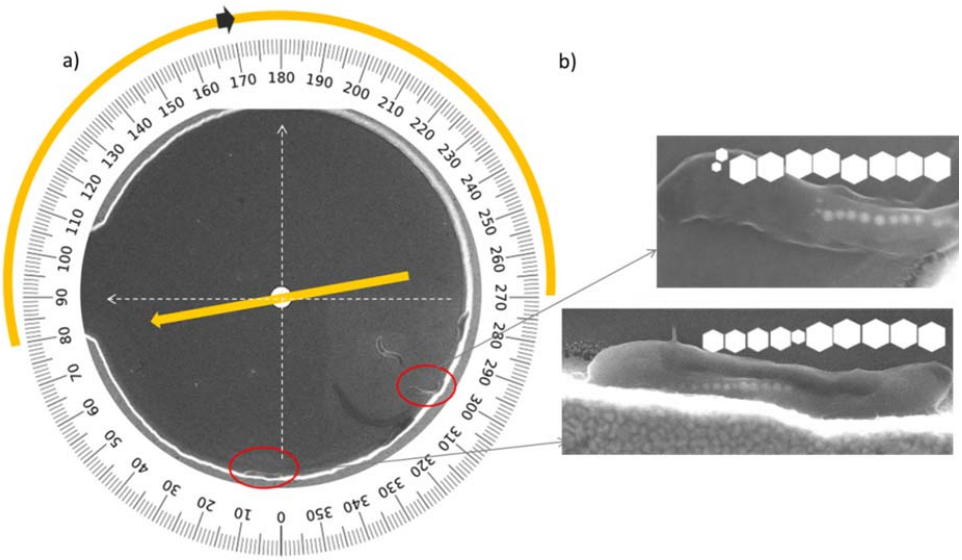

Figure 0.2 SEM image of a microresonator with two linear chains with schematic illustrations of field angles. a) The microcoil and its position in the magnetic field. The microFMR measurement starts with the magnetic field in the direction of 80°, as shown by the middle arrow. The angular dependent experiment continues in 0.5° steps until 270° to have a full period measurement. There are 5 cells in the microcoil but only two of them contain magnetosomes. b) SEM image of the two cells with magnetosomes. The orientation of the cells and the linear chains in the microcoil, are such that they are almost parallel together. The field at 90° is parallel and at 180° is perpendicular to both of the chains.

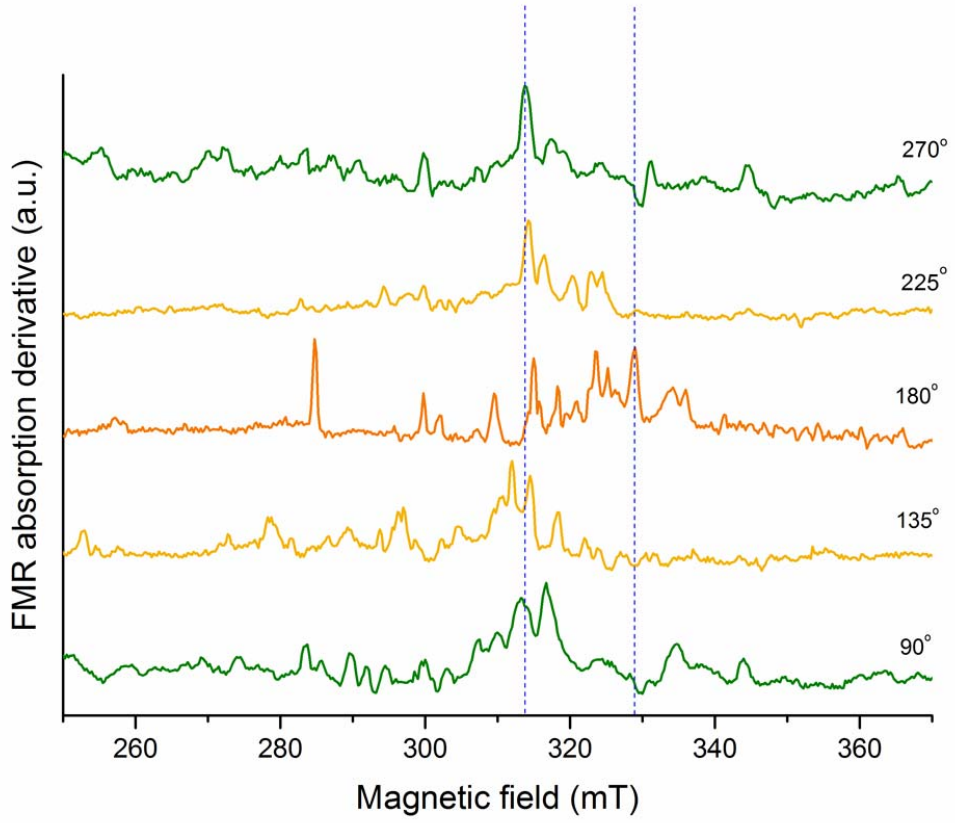

Figure 0.3 FMR absorption derivative spectrum in different in-plane angles. The magnetic field at 90° is parallel to the two chains and at 180° is perpendicular to both of them. f=9.06317 GHz.

Figure 0.3 shows the FMR spectra on the two chains in different planar angles. From the oriented bulk samples, it was shown that the absorption lines shift by changing the angle of the applied field. Some features of the two 90° with 270° spectra are reproduced, and these features are shifting in the other angles. But still due to the low intensity of the FMR spectra, the features are not as pronounced as the bulk FMR. To gain more information on the intrinsic anisotropies, a full angular dependent measurement of the two chains is performed, starting from 80° to 270° in 0.5° steps. Figure 0.4 is an amplitude map plot of the full angle spectra (min to max) of the FMR absorption derivative as a function of the applied external magnetic field over the in-plane angle.

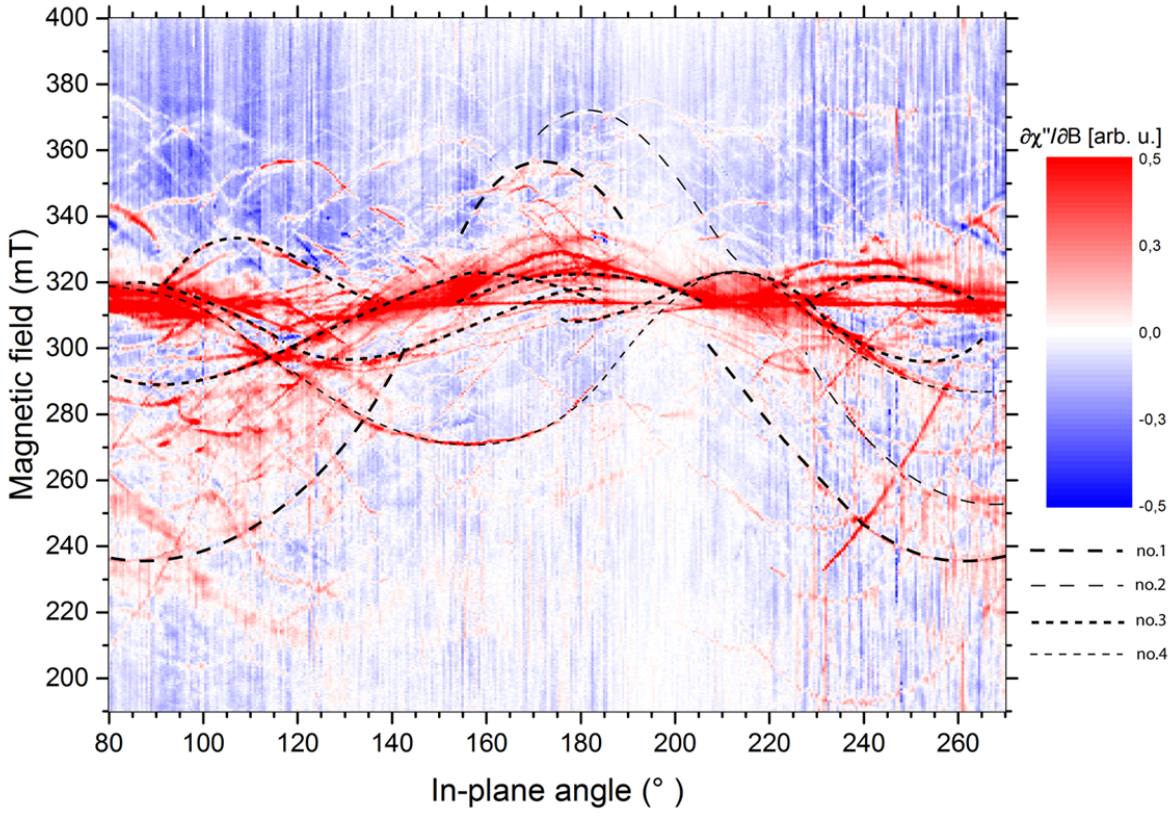

Figure 0.4 FMR amplitude map plot of two single chains in the microresonator. The intensities of the absorption derivative are plotted against the magnetic field amplitude and angle changes.

At a field position of ~310 mT a constant line can be seen. This is an angular independent EPR signal, which may be attributed to the substrate or sample holder. The amplitude map shows many distinct modes with angular dependent symmetries. Each of these modes resulted from different couplings of the magnetosomes. Some of the modes have higher intensity, which can be an indication of higher reproducibility of them. Although there are many modes attributed to various resonance bases in the sample, the aim is to figure out the main modes, which are assigned to the chain and magnetosomes anisotropy.

One main mode that can be detected is the two-fold symmetric line (dashed line no.1 in Figure 0.4) in the range of the 235 – 358 mT with its minimum at 80°, maximum point at 170°, and the next minimum at 260°. The two-fold symmetry in the spectrum angular shift is a characteristic of the samples with uniaxial anisotropy. Such a behavior has been observed in bulk samples of oriented MSR-1 wild type cells and Figure 3.18 shows its angular dependency. Considering the chains alignment in the microresonator, one can conclude that in the 80° measument they are almost parallel to the field and 260° is a perpendicular direction. This matches well with the results of bulk measurement. Also the field range, with width of ~ 123 mT, is comparable with the range of resonance field of the bulk spectra. With these evidences, it can be concluded that this mode is attributed to the whole chain's anisotropy. The same discussion is applied on the dashed line no.2 in Figure 0.4. This line is similar to the previous one with both angular and field shifts and can be assumed to be attributed to the other chain. These mods are suggesting a strong coupling of the particles in a chain and that the resonance field of the chains is strongly affected by their dipole coupling.

The next lines that attract the attention are the low field range, four-fold symmetric lines (dashed lines no.3). The high intensity of these lines as discussed before can indicate the reoccurrence of this resonance mode in the sample. The best explanation for these properties is that this mode is associated with each single magnetosome in the resonator. The four-fold symmetry is a direct result of the magnetocrystalline anisotropy. One can see how the resonance field of a system with only magnetocrystalline anisotropy has such symmetry. The high intensity is caused by the number of similar resonance modes, caused by particles in similar orientation relative to the field, and particles with different orientation have various angular dependency of the mode. The low

field range of the mode (300-320 mT) matches well with the experimental results of the scattered particles in the Δ*F3* mutant cells (Table 3.3).

Appendix B

Magnetosomes XPEEM Absorption

Figure 0.5 shows the magnetosome's absorption spectrum for non-polarized X-ray at the Fe $L_{3,2}$ edges. The spectrum agrees thoroughly with the reported stoichiometric magnetite (Goering, 2011), with the first peak position at 708.1 ev and second at 721.1 ev.

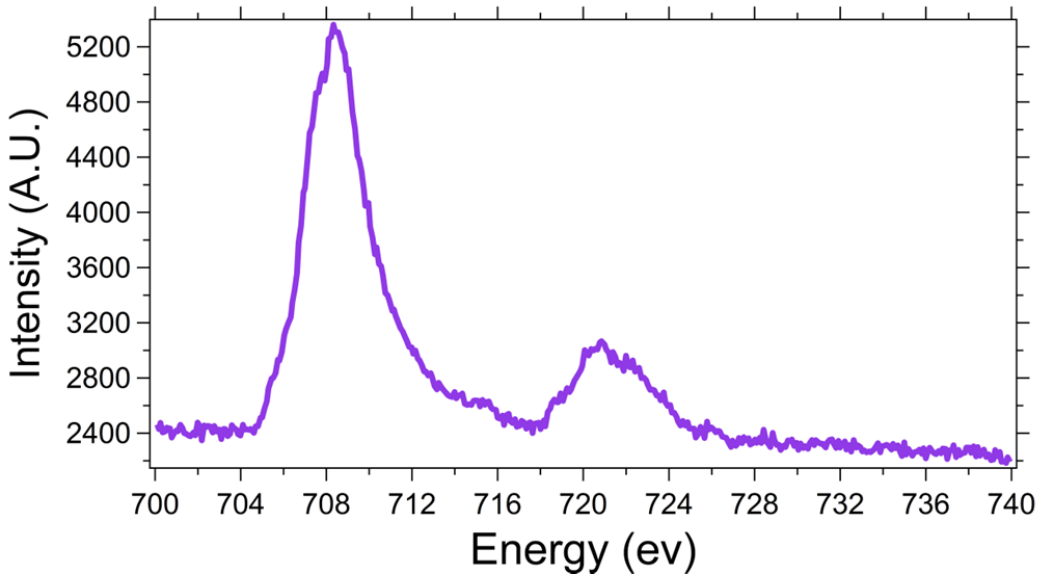

Figure 0.5 Magnetosome's absorption spectrum for non-polarized X-ray at Fe L_{32} edge. The absorption curve matches thoroughly with the reported stoichiometric magnetite (Fe_3O_4). The small shoulder at the L_3 edge (~708 ev) is the result of Iron electron spins interaction with the orbital momentum of the crystal structure.

The small shoulder at ~708 ev, which is below the main peak ($2p_{3/2} \rightarrow 3d$), indicates the oxidation (Goering, 2011, Zhu, et al., 2015).

Since the oxidation state of iron oxides affects the lattice structure, the spin-orbit interactions are influenced by the Oxygen atoms. Thus, this small peak is directly changing with the oxidation state. Zhu et.al. (Zhu, et al., 2015) show that this peak is less pronounced in stoichiometric magnetite particles and bacteria magnetosomes in comparison with more oxidized magnetite particles. In their experiment, the peak starts to get more definite, after air oxidation of the magnetite particle sample, showing the presence of γ-Fe_2O_3.

Beside the oxidation state, the small peak also changes depending on the surface sensitivity of the measuring technique. In transmission detection methods such as scanning transmission electron microscopy (STXM), the absorption is less surface sensitive than total electron yield (TEY) or PEEM techniques. Thus, the air oxidation of the samples is more evident with the later absorption measurements.

From these arguments, it can be concluded that the small peak in the measurement is similar to the stoichiometric magnetite spectrum, and that the lipid bilayer surrounding the magnetite crystals is preserving them from oxidation. This is in agreement with the reported measurement of Zhu et.al. (Zhu, et al., 2015) exposing isolated magnetosome to air for 1 week, 2 months, and 8 months and getting the same result. Longer X-ray exposures can help to reduce the noise of the spectrum. However, one drawback of this can be the damage of the magnetosome membrane by the photons and loss of its protection. Besides this, Widdrat et al. have shown that the magnetic properties of the oxidized particles do not decrease dramatically (Widdrat, et al., 2014).

Acknowledgements

I would like to express my appreciation to my supervisor Dr. Damien Faivre, for giving me the opportunity to join the research at Max Planck Institute of Colloids and interfaces, and opening many possibilities for me to learn and practice in interesting new areas. I am thankful for all his advices, trust and patience.
I am very grateful to Prof. Stefan Klumpp, for supervising me, especially through the theoretical and simulations of my work, and for all the helpful discussions and supports.
I express my thanks to Prof. Reinhard Lipowsky and the other IMPRS administration.
I would also like to write in honor and memory of Prof. Peter Strauch, for his precious help in the FMR experiments for two years at University of Potsdam. We are sorry for not having him among us anymore. His impact on EPR studies will last forever.
I want to thank Prof. Michael Winklhofer for his collaboration on this work, all the fruitful discussions, and also providing me the chance of conducting measurements at University of Duisburg.
I am thankful to Dr. Florian Kronast for his support at the SPEEM setup at BESSY. Also, many thanks to Anna Pohl and Lucas Kuhrts for their helpful and friendly presence during the beam time.
Many thanks to Agata for guiding me through the biology lab, Bahareh for all the interesting discussions and collaborations, Victoria for her great help at TEM, all the other former and current group members, and all my supportive friends at MPIKG.

My warmest thanks to my parents and little sister, for their endless love.

And my dear Hamidreza who always stands beside me…Thank you for making this possible.

“a life is measured by moments like these”